

Star Formation Conditions in Nearby Galaxies

INAUGURAL-DISSERTATION

zur

Erlangung des Doktorgrades
der Mathematisch-Naturwissenschaftlichen Fakultät
der Universität zu Köln



vorgelegt von

Marc Hitschfeld
aus Windeck-Lindenpütz

Köln 2008

Berichterstatter: Prof. Dr. Jürgen Stutzki
Prof. Dr. Frank Bertoldi

Tag der mündlichen Prüfung: 27.11.2008

Für

Janka.

The important thing is not to stop questioning.
- Albert Einstein -

Abstract

The understanding of gravitational stability of galactic disks against star formation, the interplay of atomic and molecular components of the interstellar medium in a galaxy and its physical conditions, namely temperature and density, are important to gain a deeper insight into star formation. Nearby galaxies like the spiral galaxy M51 or the southern starburst galaxies NGC4945 and Circinus offer excellent opportunities to investigate these topics over a complete galactic disk or parts of the galaxy.

A suitable tracer to study the molecular part of the gaseous component of galaxies is the CO molecule. It is the second most abundant molecule after H₂ in the interstellar medium, its lower lying transition are excited at typical conditions of molecular clouds and the rotational transitions lie in the radio window. Thus, CO emission can penetrate throughout galactic disks and is observable from the ground. Apart from complementary data from the literature, we use observations of ¹²CO 2–1, ¹²CO 4–3, and ¹³CO 2–1 in this thesis. Additionally, the [C I] ³P₁ – ³P₀ fine structure line was observed to study the physical conditions in the central regions of galaxies.

In the first part of this thesis, the nearby spiral galaxy M51 is used as a sample source to investigate the onset of star formation. CO, H I, radio-continuum, dust, and stellar maps of M51 are combined to study star formation rate, the H₂/H I transition, the gas-to-dust ratios, the stability of the disk against gravitational collapse, and properties of the giant molecular clouds. Parts of the results have been published in *Astronomy & Astrophysics* (461,143) in 2007 and are submitted to *Astronomy & Astrophysics*, 2008 for publication.

We use the first complete ¹²CO 2–1 map of M51 including the companion galaxy NGC5195 observed with HERA at the IRAM-30m telescope to trace the molecular gas. Complementary H I VLA data is used to study the atomic gas distribution and the combined total gas surface density. The total gas density is compared to the dust density from 850 μm SCUBA data. Using radio continuum VLA data, we compute the Schmidt law in M51, an empirical relation of total gas density and star formation rate. The velocity dispersions of the molecular and atomic gas, indicating the local resistance

against gravitational collapse, are computed. For the Toomre Q parameter of the disk, a measure of the gravitational stability (see also chapter 2.3), we combine the stellar surface density derived from the 2MASS K -band survey with total gas surface density and velocity dispersions of stellar, atomic, and molecular components of the disk. The *Gaussclumps*-algorithm is applied to decompose the ^{12}CO 2–1 emission into molecular cloud complexes with masses down to the resolution limit. Subsequently, we study the clump mass spectrum of the identified molecular clouds.

The ratio of molecular to atomic gas surface density shows a close-to *powerlaw* dependence on the hydrostatic pressure P_{hydro} . The distribution of the gas surface density, Σ_{gas} , in M51 shows an underlying exponential distribution with a scale-length of $h_{\text{gas}} = 7.6$ kpc representing 55% of the total gas mass, comparable to the properties of the exponential dust disk. The total gas surface density and the star formation rate per unit area and time $\dot{\Sigma}_{\text{SFR}}$ [$\text{M}_{\odot}\text{pc}^{-2}\text{Gyr}^{-1}$] are correlated. This empirical relation is also found in other galaxies and is the so called local *Schmidt law* (chapter 2.4). We fitted a local Schmidt law with a power-law index of $n = 1.4 \pm 0.6$ to our data in M51. In contrast to the velocity widths observed in HI, the CO velocity dispersion shows enhanced line widths in the spiral arms compared to the interarm regions. The threshold of gravitational stability according to the total Toomre parameter, $Q_{\text{tot}} = 1$ (chapter 2.3), is close to the results in the radial averages: Q_{tot} varies from 1.5-3. A map of Q_{tot} shows values around 1 on the spiral arms indicating self-regulation. The clump mass spectrum extends over a mass range of $4.9 \cdot 10^5 \text{ M}_{\odot}$ to $1.2 \cdot 10^8 \text{ M}_{\odot}$ and shows a *powerlaw* index $\alpha = 1.71 \pm 0.24$. The positions of the 16 most massive identified clumps in the inner part follow the shape of a logarithmic spiral.

The second part of this thesis deals with the estimation of the physical conditions in the central regions of the star burst galaxies NGC 4945 and Circinus from molecular line observations. The temperature, molecular density, and column densities of CO and atomic carbon are predicted. We published parts of this analysis in *Astronomy & Astrophysics* (479,75) in 2008.

The new NANTEN2 4m sub-millimeter telescope in Pampa La Bola, Chile, enabled us to observe for the first time CO 4–3 and [C I] $^3P_1 - ^3P_0$ in the

centers of both galaxies at linear scales of 682 pc and 732 pc, respectively. We compute the cooling curves of ^{12}CO and ^{13}CO using radiative transfer modeling and estimate the temperature, density, and column density of CO and [CI].

The centers of NGC 4945 and Circinus exhibit [CI] $^3P_1 - ^3P_0$ luminosities of 91 and 67 $\text{K km s}^{-1} \text{kpc}^2$, respectively. The [CI] $^3P_1 - ^3P_0/\text{CO } 4-3$ ratio of integrated intensities are large at 1.2 in NGC 4945 and 2.8 in Circinus. Combining previous CO $J= 1-0$, $2-1$ and $3-2$ and $^{13}\text{CO } J= 1-0$, $2-1$ studies with our new observations, the radiative transfer calculations give a range of densities, $n(\text{H}_2) = 10^3 - 3 \times 10^4 \text{ cm}^{-3}$, and a wide range of kinetic temperatures, $T_{\text{kin}} = 20 - 100 \text{ K}$, depending on the density. The estimated total [CI] cooling intensity is stronger by factors of $\sim 1 - 3$ compared to the total CO cooling intensity. The CO/C abundance ratios are 0.2-2, similar to values found in Galactic translucent clouds. Future high- J CO and [CI] $2-1$ observations will be able to better constrain the ambiguities of density and temperature.

Zusammenfassung

Das Verständnis des Zusammenhangs von Gravitationsstabilität galaktischer Scheiben und Sternentstehung, das Wechselwirken der atomaren und molekulare Komponenten des interstellaren Mediums in einer Galaxie und die physikalischen Bedingungen, im Besonderen Temperatur und Dichte, sind für ein tieferes Verstehen des Sternentstehungsprozesses wichtig. Nahegelegene Galaxien wie die Spiralgalaxie M51 oder die südlichen Galaxien NGC4945 und Circinus bieten ideale Bedingungen, um die genannten Themen zu untersuchen.

Das CO-Molekül ist gut geeignet, den molekularen Anteil der Gaskomponente von Galaxien zu studieren. Es ist das zweithäufigste Molekül (nach dem molekularem Wasserstoff H₂) im interstellaren Medium, seine niedrigeren Übergänge sind bei typischen Bedingungen in Molekülwolken angeregt und die Rotationsübergänge liegen im Radiobereich. Dadurch kann die CO-Strahlung komplette Scheiben von Galaxien durchdringen und ist vom Boden gut beobachtbar. Neben Komplementärdaten aus der Literatur benutzen wir in dieser Arbeit Beobachtungen von ¹²CO 2–1, ¹²CO 4–3 und ¹³CO 2–1. Zusätzlich wurde der [C I] ³P₁ – ³P₀ Feinstrukturübergang beobachtet, um die physikalischen Bedingungen in den zentralen Regionen von Galaxien zu studieren.

Im ersten Teil dieser Arbeit werden am Beispiel der nahegelegenen Spiralgalaxie M51 die Bedingungen für Sternentstehung untersucht. CO, H I, Radio-Kontinuum, Staub und stellare Karten von M51, werden für die Untersuchung der Sternentstehungsrate, des H₂/H I Übergangs, des Gas-Staub Verhältnisses, der Gravitationsstabilität der Scheibe der Galaxie und für die Bestimmung der Eigenschaften von Riesenmolekülwolken kombiniert. Teilergebnisse dieses Kapitels wurden in *Astronomy & Astrophysics* (461,143) in 2007 veröffentlicht und sind für Publikation in *Astronomy & Astrophysics* in 2008 eingereicht.

Um das molekulare Gas zu beobachten, benutzen wir die erste komplette ¹²CO 2–1 Karte von M51 inklusive des Begleiters NGC5195, die mit dem HERA-Empfänger am IRAM-30m Teleskop beobachtet wurde.

Die Verteilung der atomaren Gaskomponente wurde mit HI-VLA Komplementärdaten beobachtet und mit der molekularen Komponente zur totalen Gasverteilung kombiniert. Mit Hilfe von Radio-Kontinuum Daten berechnen wir das sog. *Schmidt law* in M51, eine empirische Relation zwischen Oberflächengasdichte und Sternentstehungsrate. Die Geschwindigkeitsdispersionen des molekularen und atomaren Gases werden bestimmt. Diese können lokal den Kollaps durch Gravitation verhindern. Um den Toomre Parameter Q zu berechnen, der ein Maß für die Stabilität gegen Kollaps ist, benutzen wir eine Sternmassendichtekarte abgeleitet von 2Mass K -Band Beobachtungen und Karten der Gasmassendichte sowie der Geschwindigkeitsdispersionen der stellaren, atomaren und molekularen Komponente der Scheibe. Wir verwenden den *Gaussclumps*-Algorithmus, um die ^{12}CO 2–1 Emission in Agglomerationen von Riesenmolekülwolken zu zerlegen, deren Massen bis an die Auflösungsbegrenzung heranreichen. Damit untersuchen wir das Klumpen-Massen Spektrum der identifizierten Riesenmolekülwolken.

Das Verhältnis von molekularer zu atomarer Gasflächenmassendichte zeigt eine *Powerlaw*-ähnliche Abhängigkeit vom hydrostatischem Druck P_{hydro} . Die Verteilung der Gasflächenmassendichte, Σ_{gas} , in M51 zeigt eine unterliegende exponentielle Verteilung mit einer Skalenlänge von $h_{\text{gas}} = 7.6$ kpc und einem Massenanteil von 55% an der totalen Gasmasse, ähnlich der Staubmassenverteilung. Die Gasflächendichte und die Sternentstehungsrate pro Einheits-Fläche und Zeit, $\dot{\Sigma}_{\text{SFR}}$ [$M_{\odot}\text{pc}^{-2}\text{Gyr}^{-1}$], sind korreliert. Diese empirische Beziehung wurde auch in anderen Galaxien festgestellt und wird als *Schmidt law* (chapter 2.4) bezeichnet. Wir fitten ein lokales Schmidt law mit einem *Powerlaw*-Index von $n = 1.4 \pm 0.6$ in M51. Im Gegensatz zu den HI -Momenten zeigen die CO-Dispersionen erhöhte Linienbreiten auf den Spiralarmen im Vergleich zu den Zwischenarm-Regionen. Die radialen Mittelungen zeigen Werte in der Nähe des Grenzwertes zur Gravitationsinstabilität: nach dem Toomre-Kriterium $Q_{\text{tot}} = 1$ (chapter 2.3). In den radialen Mittelungen variiert Q_{tot} zwischen 1.5 und 3. Eine Karte von Q_{tot} zeigt Werte um 1 in den Spiralarmregionen, was auf Selbstregulierung in der Scheibe der Galaxie hindeutet. Das Klumpenmassenspektrum deckt einen Massenbereich von $4.9 \cdot 10^5 M_{\odot}$ bis $1.2 \cdot 10^8 M_{\odot}$ ab und zeigt einen *Powerlaw*-Index $\alpha = 1.71 \pm 0.24$. Die Positionen der 16 massivsten identifizierten Klumpen im Inneren von M51 zeigen die Form einer logarithmis-

chen Spirale.

Im zweiten Teil der Arbeit werden die physikalischen Bedingungen in den zentralen Regionen der Galaxien NGC4945 und Circinus aus molekularen Linienbeobachtungen abgeschätzt. Die Temperatur, molekulare Dichte und Säulendichte von CO und [C I] werden modelliert. Teilergebnisse dieses Kapitels sind in *Astronomy & Astrophysics* (479,75) in 2008 publiziert.

Mit Hilfe des neuen NANTEN2 4m Submillimeter-Teleskops in der Pampa la Bola, Chile, haben wir zum ersten Mal CO 4-3 und [C I] $^3P_1 - ^3P_0$ in den Zentralregionen der beiden Galaxien mit einer räumlichen Auflösung von 682 pc beziehungsweise 732 pc beobachtet. Wir berechnen mit Hilfe von Strahlungstransport die Kühlkurven von ^{12}CO und ^{13}CO und schätzen Temperatur, Dichte und Säulendichte von CO und [C I] ab.

Die Zentren von NGC 4945 und Circinus zeigen [C I] $^3P_1 - ^3P_0$ Luminosität mit 91 beziehungsweise $67 \text{ K km s}^{-1} \text{ kpc}^2$. Das Verhältnis der integrierten [C I] $^3P_1 - ^3P_0$ /CO 4-3 Intensitäten ist hoch mit 1.2 in NGC 4945 und 2.8 in Circinus. Wir benutzen zusätzlich CO $J= 1-0$, $2-1$ und $3-2$ sowie $^{13}\text{CO } J= 1-0$, $2-1$ mit den neuen Beobachtungen. Damit ergeben Strahlungstransportrechnungen eine Spanne möglicher Dichten, $n(\text{H}_2) = 10^3 - 3 \times 10^4 \text{ cm}^{-3}$, und eine Spanne von kinetischen Temperaturen, $T_{\text{kin}} = 20 - 100 \text{ K}$, abhängig von den Dichten. Die abgeschätzte totale [C I]-Kühlleistung ist stärker als die CO-Kühlleistung um einen Faktor von $\sim 1 - 3$. Das CO/C Häufigkeitsverhältnis ist 0.2-2. Zukünftige Beobachtungen von hohen CO Übergängen und [C I] $2-1$ werden es ermöglichen, die auftretenden Unsicherheiten in Dichte und Temperatur besser einzuschränken.

Contents

1	Introduction	15
2	Background and concepts	21
2.1	Morphology of galaxies	21
2.2	Formation and evolution of spiral galaxies	24
2.2.1	Density wave theory	26
2.3	Disk stability	30
2.4	Kennicutt-Schmidt law	31
2.5	Radiative transfer	34
2.5.1	Collisional excitation	35
2.5.2	Radiation mechanisms	36
2.5.3	Rate equation	38
2.5.4	Critical density	40

3	The nearby galaxy M51 - a laboratory to study the onset of star formation	43
3.1	Introduction to M51	44
3.2	IRAM-30m HERA-Observations	46
3.2.1	^{12}CO 2-1	46
3.2.2	^{13}CO 2-1	48
3.2.3	Complementary data	49
3.3	Observational results	50
3.3.1	Integrated intensity map using the masked moment method	50
3.3.2	Molecular gas distribution	51
3.3.3	^{13}CO 2-1	53
3.3.4	HI and radio continuum	54
3.3.5	Dust emission	56
3.4	Molecular and atomic gas	57
3.4.1	The total gas surface density	57
3.4.2	Total gas densities in other galaxies	61
3.5	Stellar surface density from the <i>K</i> -Band emission	63
3.6	Radial averages and Schmidt law	64
3.6.1	Radial distribution of the gas	65
3.6.2	The molecular gas fraction	67

3.6.3	The hydrostatic pressure	69
3.6.4	Star formation rate and local Schmidt law	71
3.6.5	The local Schmidt law and star formation efficiency in simulations	77
3.7	The structure of the total gas density	79
3.8	Gravitational stability	84
3.8.1	Kinematics of the ^{12}CO 2–1 data	84
3.8.2	Radial Toomre analysis for the gaseous disk	94
3.8.3	Discussion of the radial Q_{gas} analysis	96
3.8.4	The combined Toomre parameter Q_{total}	98
3.8.5	The local distribution of Q_{tot}	102
3.9	Correlation of Toomre Q and H_2/HI	106
3.10	Giant Molecular Associations in M51	107
3.10.1	Formation and destruction of GMCs	107
3.11	Molecular cloud properties	110
3.11.1	<i>Gaussclumps</i>	110
3.11.2	Mass and mass spectrum of clumps	112
3.12	Summary	116

4	The physical conditions in the central regions of galaxies	119
4.1	Introduction	119
4.1.1	NGC 4945	120
4.1.2	Circinus	122
4.1.3	The importance of submm lines in NGC4945 and Circinus	123
4.2	Observations with the NANTEN2 telescope	124
4.2.1	Spectra of CO 4–3 and [C I] 1–0	126
4.3	Physical conditions	128
4.3.1	Escape probability calculations using CO and ^{13}CO	129
4.4	Summary and discussion	135
5	Outlook	143
A	^{12}CO 4–3 in NGC 253	159
	List of Publications	171
	Danksagung	173
	Erklärung	177
	Lebenslauf	179

Chapter 1

Introduction

The identification of the observed nebular stellar aggregations as external galaxies was not resolved until the early 20th century. In the *Great debate* Shapley and Curtis discussed whether the spiral nebulae were stellar clouds and part of the Milky Way or objects similar to the Milky Way at greater distance. Hubble was able to resolve this debate (Hubble 1938) and showed that the Andromeda galaxy was clearly outside of the Milky Way using the 2.5m Mt. Wilson telescope for observations of Cepheid variables in Andromeda. Cepheids show a strong correlation of luminosity and the period of their variability which allowed Hubble to use them as standard candles and to determine the distances to Andromeda more precisely. Hubble was able to take advantage of the technological progress in optical astronomy in the 19th century. The introduction and advance in spectroscopy and photometry enabled the astronomers to obtain velocity information and accurate luminosities of the observed objects.

Modern CCD-detectors and space based telescopes like the Hubble Space Telescope launched in 1990, enable astrophysicists to survey large areas of the sky at high angular resolution, overcoming the disturbances by the atmosphere in ground-based observations (the recent introduction of active and adaptive optics helps to reduce atmospheric disturbances in the near-infrared and optical regime). Current knowledge is that the visible

Universe contains about 100 billion galaxies, with each of them containing, similar to the Milky Way, about 100 billion stars.

The birth of radio astronomy was in 1933 when Jansky discovered extraterrestrial cm radio emission from the Milky Way and linked it to the stars and the interstellar matter in the Galactic disk (Jansky 1933). Reber (1940) performed the first extragalactic radio observations in the Andromeda Galaxy M31 using a parabolic radio antenna.

After the first detections of molecules in space in the optical (CH, CH⁺, CN) from 1937 (Swings & Rosenfeld 1937), extragalactic observations of molecular gas in the radio domain were first done in 1974. Whiteoak & Gardner (1974) detected the OH molecule in absorption in the southern galaxy NGC4945 (this galaxy is also studied in this thesis). The first extragalactic detection of the CO molecule by Rickard et al. (1975) followed.

The atmospheric radio window, enabling ground based observations, extends from about 1MHz at the lower frequency range to around 1THz. The low end cutoff is caused by ionospheric absorption and scattering. At the high end, the absorption of atmospheric water and oxygen are the main obstacles for observations. This is one reason for the remote dry and high-altitude locations of modern mm and submm-radio telescopes: e.g. the KOSMA¹-telescope on the Gornergat, Switzerland at 3.100m, the IRAM²-30m telescope at Pico Veleta, Spain at 3000m and the APEX³ and NANTEN2-telescopes at Pampa la Bola, Chile at 4900m altitude and the future ALMA⁴ interferometer at the same location. Another excellent site for submm-telescopes is Mauna Kea, Hawaii with the JCMT⁵ and the CSO⁶ on site.

¹Kölner Observatorium für Submillimeter Astronomie

²Institut de Radio Astronomie Millimetrique

³Atacama Pathfinder Experiment

⁴Atacama Large Millimeter Array

⁵James Clerk Maxwell Telescope

⁶Caltech Submillimeter Observatory

Observations of external galaxies with these sensitive facilities enable us to study the distribution of the interstellar medium over the whole disk of a galaxy, in contrast to galactic studies which are in the optical limited due to the strong extinction in the disk of the Milky Way and the location of the observer within the disk. The disk of a galaxy is composed of stars and gas. The relative mass fraction of the interstellar medium varies depending on the location in a galaxy and among other things, this fraction will be investigated in the spiral galaxy M51. The gas consists of an atomic and molecular component with locally varying mass fractions. The dynamics and structure of the atomic gas are well traced by the 21 cm hyperfine structure line of the neutral H I atom. We will later combine H I-data from our collaborators and observed line transitions in CO and [C I] as tracers of the molecular gas.

To date approximately 130 molecules have been detected in measurements beyond our solar system. As a tracer for the molecular gas we use CO. It is the second most abundant molecule after H₂ in the interstellar medium as it is very stable due to its high binding-energy. CO is used as a standard tracer for molecular mass with rotational transitions in the radio window. H₂ is not suitable because it needs high excitation temperatures of several hundred Kelvin which exceed the typical temperatures of the cold molecular phase of interstellar medium of several 10 K significantly. The CO molecule has a photo-dissociation potential of 11.1 eV, which is near the upper end of the interstellar photon field of 13.6 eV caused by absorption at the Lyman edge due to atomic hydrogen. The excitation energy of the lowest lying rotational transition is at 5.6 K, ideal for studying the interstellar medium with typical temperatures of several 10 K. CO is a linear diatomic molecule with a low permanent dipole moment of 0.1 Debye. The low- J CO transitions thus have critical densities of $\sim 10^4$ cm⁻³ for collisions with H₂ at typical temperatures in the interstellar medium. A critical density describes a state of balance between the radiative (spontaneous emission depending on the Einstein A-coefficient) and collisional de-excitation (proportional to the density), for a given line transition (see also chapter 2.5).

Another important tracer is the neutral carbon [C I] atom. The fine structure transition [C I] $^3P_1 - ^3P_0$ (henceforth 1-0) is excited at 24 K and with

a relatively low critical density of 10^3 cm^{-3} , matching typical conditions in the interstellar medium. The [C I] atom has been found in good correlation with low- J CO lines (e.g. Mookerjea et al. 2006) and appears to be a good tracer of surface regions of clumps illuminated by the FUV field of newborn, massive stars (e.g. Kramer et al. 2005). The photo-ionization potential of [C I] to [C II] is at 11.3 eV. The [C I] 1–0 line has been detected in about 30 galactic nuclei (Gerin & Phillips 2000; Israel & Baas 2002; Israel 2005).

The [C II] 158 μm fine-structure line is another important tracer associated with warm, dense photo dissociated surface regions of molecular clouds illuminated by nearby OB stars. It is excited at 92 K and the critical density is $5 \cdot 10^3 \text{ cm}^{-3}$. Emission of CO, [C I] and [C II] traces the bulk of carbon bearing species in molecular clouds and is important in their chemical network. The HCN molecule is a tracer found in dense molecular gas regions with typical densities of $n(\text{H}_2) = 10^4 - 10^5 \text{ cm}^{-3}$.

Outline

In this thesis, newly observed ^{12}CO 2–1, ^{12}CO 4–3, ^{13}CO 2–1, and [C I] 1–0 -data are combined with complementary molecular line, radio continuum, and HI -data from the literature or recently observed by collaborators. This data are used to study the physical conditions and mechanisms of star formation in the interstellar medium of external galaxies.

In chapter 2, we summarize important background and theoretical concepts as far as they are relevant for the analysis parts of this thesis. This includes the Hubble scheme for the classification of galaxies, mechanisms for the formation of spiral galaxies, the gravitational stability of disks in galaxies and empirical star formation relations.

We also discuss how to determine physical conditions like temperature, density, and column density from observed integrated intensities using radiative transfer calculations. This is later applied to the central regions

of the two southern galaxies Circinus and NGC4945.

In chapter 3, we study the nearby spiral galaxy M51 as a template source for global and local distribution of the atomic and molecular gas, star formation laws and gravitational stability of the disk. We identify molecular clouds from the ^{12}CO 2–1 data and study their mass and stability. The dynamics of M51 and the deviations of purely rotational motions are discussed and compared to model predictions.

For this analysis the first complete ^{12}CO 2–1 map of M51 including the south-western spiral arm and the companion galaxy NGC5195 is presented. This map was obtained with the IRAM-30m telescope using the receiver array HERA⁷. We combine these newly observed data set with additional H I, radio continuum, and infrared (K -band $2.2\mu\text{m}$)-data. The M51 project was a collaborative effort together with C. Kramer, J. Stutzki, B. Mookerjea (KOSMA), K. Schuster (IRAM, France) and S. Garcia-Burillo (Observatorio de Madrid, Spain).

Chapter 4 assesses the physical conditions, namely temperature, density and column density, in the central regions of the southern starburst galaxies NCG4945 and Circinus. First detections in the ^{12}CO 4–3 and [C I] 1–0 transitions in these sources combined with lower rotational CO transitions and radiative transfer calculations are used to determine these quantities. The abundance ratio of CO and [C I] is discussed and compared to abundance ratios in molecular clouds and central regions of other galaxies. The observations have been carried out by me, C. Kramer, R. Simon and the NANTEN2-team using the NANTEN2-telescope in Pampa la Bola, Chile. This telescope is operated jointly by the Nagoya University radioastronomy group (Prof. Fukui), the KOSMA group from Universität zu Köln (Prof. Stutzki), the University of Bonn (Prof. Bertoldi) and other contributing partners from Chile, Australia and Korea. The observations and analysis in southern extragalactic sources were a joint project of the KOSMA-group (C. Kramer, J. Stutzki) and colleagues of the Argelander Institute, University of Bonn (M. Aravena, F. Bertoldi).

In the last chapter, we address the perspectives of future extragalactic stud-

⁷Heterodyne Receiver Array

ies using the new generation of radio-astronomical facilities on ground-, air- and space-based platforms.

Chapter 2

Background and concepts

2.1 Morphology of galaxies

The following sections follow closely parts of the books *J. Binney and S. Tremaine: Galaxy Dynamics* and the lecture *Entwicklung von Galaxien* by *S. Hüttemeister* and summarize relevant concepts in the context of this thesis.

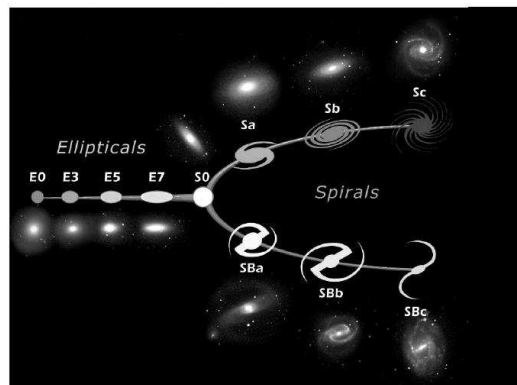


Figure 2.1: Hubble sequence of galaxy morphology.



Figure 2.2: An HST composite edge on view of the Sa-type spiral galaxy M101. M101 nicely shows the structure of disk galaxies including the bulge in the center, the disk and the halo (www.spacetelescope.org).

Galaxies are classified into different categories based on their appearance in the optical. As an example the classification scheme of the Hubble sequence is shown in Fig. 2.1 (Sandage 1961). This classification scheme was introduced by Hubble in 1936 in his book *The realm of nebulae*. Hubble interpreted the diagram as a time series of evolution of a galaxy with increasing age from left to right (Fig. 2.1) thus, referring to ellipticals as early-type and to spirals as late-type galaxies. The Hubble interpretation of the diagram is discarded today but the nomenclature of early-types, late-types still is in use although in conflict with the temporal evolution. The spiral galaxy's in fact turned out to be the earlier stage of galaxy evolution compared to ellipticals.

Elliptical galaxies are labeled E_n where the axial ratio b/a of major axis b and minor axis a determines the number via $n = 10(1 - b/a)$. For galaxies later than elliptical type, the Hubble diagram shows two branches of galaxies distinguishing between barred galaxies and the so called normal galaxies. The barred galaxies occur with a similar frequency as the normal galaxies. The S0 or SB0 type galaxies are called lenticular galaxies and show a central brightness distribution similar to an elliptical galaxy. In the outermost parts they become rather flat, which is best seen in edge-on systems. The second branch in the Hubble sequence contains the normal spirals. The morphology of these types of systems shows a more or less extended central bulge resembling the brightness profile of an elliptical galaxy and no visible bar. The bulge is the central part of a rather thin disk which shows a more or less pronounced spiral pattern. The early-type spirals are

located on the left side of the Hubble diagram and show a more extended bulge and a rather smooth spiral structure. The late-type spirals show a less extended bulge and sharply defined spiral arms. Galaxies obeying no symmetry were classified as irregulars in the Hubble classification.

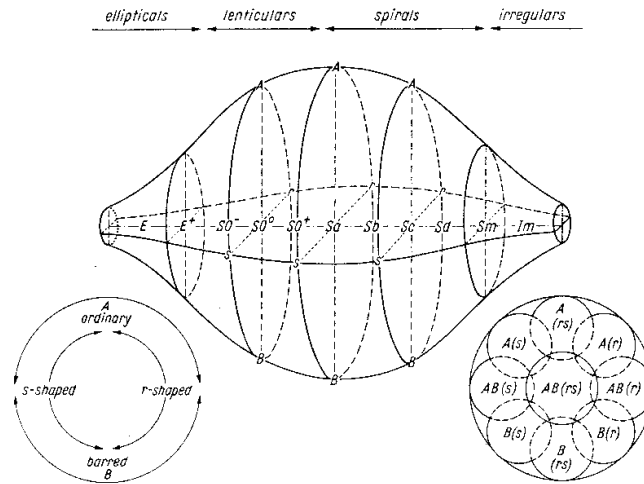


Figure 2.3: Classification of galaxy morphology by de Vaucouleurs. The sketch is taken from Buta & Combes (1996).

Other classification schemes were later introduced e.g. by de Vaucouleurs (1959) and Elmegreen & Elmegreen (1982). The de Vaucouleurs scheme is used in this work and is an extension of the Hubble scheme (see Fig. 2.3). The Hubble classification from ellipticals to spirals and irregulars is kept. The classification of the spirals is more sophisticated. Three criteria determine the galaxy type according to de Vaucouleurs (1959): the absence or presence of a bar (SA, SB or intermediate SAB), the absence or presence of ring-like structures (symbols s, r or rs) and the appearance of the spiral arms. Additional to the Hubble specifications of the spiral arms, Sd for diffuse, broken arms with a faint bulge is introduced and Sm for irregular appearance without a bulge. The combination of these three criteria determines the galaxy type according to the Vaucouleurs scheme.

In the next sections, we will give a summary of theoretical concepts for the formation of spiral galaxies and set the stage for terms later used in the

detailed analysis of the spiral galaxy M51.

2.2 Formation and evolution of spiral galaxies

Spiral patterns are a well known morphology observed in galaxies. They seem to be long-lived in the sense that they are stable over several orbital timescales, implied by the large number of galaxies with prominent spiral patterns.

The simplest concept producing spiral structure is differential rotation. Gas and stars in galaxies rotate with different angular velocities at different radii $\Omega = \Omega(r)$, the so called *differential rotation*. A spiral pattern caused by this effect would windup in a few orbital timescales around the center in contrast to the observed structures in galaxies, as we will discuss next.

Rotation curves of spiral galaxies, i.e. the dependence of rotation velocity on galactocentric radius $v(r)$ around the center, have been mostly determined from optical- and HI-line spectroscopy and subsequently created position-velocity diagram's. E.g. Sofue et al. (1999) studied rotation curves from a sample of around 50 spiral and irregular galaxies. They used a fixed intensity criterion (depending on the maximum and lowest-contour intensity) to determine the rotation velocity at a given position in the position-velocity diagram. Typically rotation curves of all types of spiral galaxies show a similar structure. After a steep rise of the rotation velocity in the central part, the rotation curve flattens at galactocentric radii of up to 5 kpc from the center and stays constant in the outer part. The flat outer parts are not expected from the observed mass profiles assuming Keplerian motions and Newtonian gravity and were one of the first indications for the existence of dark matter and dark matter halos in galaxies.

For a constant rotation velocity, the angular velocity $\Omega = v(r)/r$ thus shows differential rotation with the dependence $\Omega \sim r^{-1}$. If the spiral arms would be rotating with this differential rotation, the spiral arms would wind-up in few rotations around the center. Thus, a much tighter spiral



Figure 2.4: Composite Hubble Space Telescope image of the grand-design spiral galaxy M51 showing the prominent spiral structure (www.spacetelescope.org).

structure than found in observations of spiral galaxies would be expected (e.g. Kalnajs 1973). Typical values are a constant circular velocity $v_c=200$ kms^{-1} at a radius $R=8$ kpc. After a (relatively short) time of 1 Gyr the pitch angle of the spiral arms winds up to 2° - the tightest pitch angles observed range from 5° to 30° , depending on the galaxy type. This shows the shortcoming of the differential rotation approach.

Lin & Shu (1964) were the first to solve the *wind-up dilemma* by present-

ing a density wave theory to explain the observed spiral structure in disk galaxies. The theory assumes that a density wave moves through the disk of the galaxy at a constant angular velocity (pattern speed Ω_p). Possible triggering mechanisms will be mentioned later. We will discuss the density wave mechanism in more detail in the next section.

2.2.1 Density wave theory

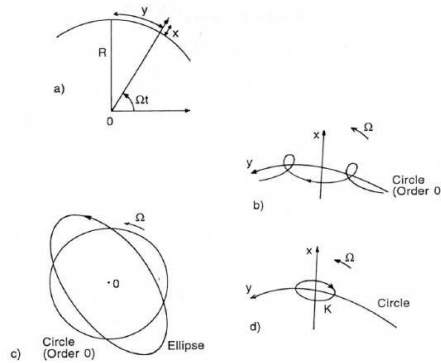


Figure 2.5: Illustration of different trajectories: a) Definition of the coordinate system. b) General case of a rosette. c) $\kappa = 2\Omega$. d) $\Omega = \Omega_p$.

In disk galaxies gas and stars move on nearly circular orbits as dissipation forces (caused by tidal or collisional interaction), force them to enter the lowest energy trajectory. The special case of a Keplerian potential yields ellipses as orbits with circles as the lowest energy limit case. Orbits of non-Keplerian potentials can be approximated by precessing ellipses forming rosettes.

For disk galaxies a commonly used approximation for the orbits (also later used in the analysis of the M51 observations) is the *epicyclic approximation*.

The epicyclic frequency is defined as $\kappa^2 \equiv \partial^2 \Phi_{\text{eff}} / \partial r^2$, neglecting all higher order terms in the Taylor expansion of the effective potential (different cases of κ are illustrated in Fig. 2.5). Φ_{eff} is the axisymmetric effective potential in the rotating frame including the *centrifugal* potential. Motions in the

plane of the galaxy are considered. In terms of the angular frequency κ can be expressed as: $\kappa^2 = r \frac{d\Omega^2}{dr} + 4\Omega^2$, with the angular frequency $\Omega = v/r$.

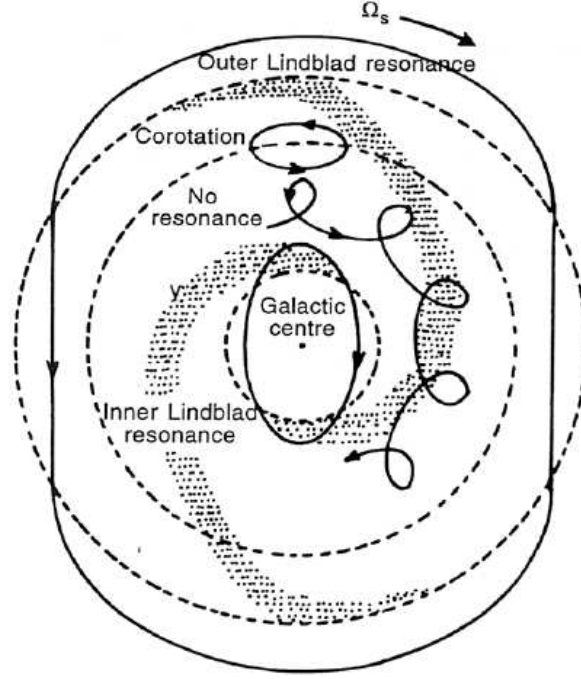


Figure 2.6: Corotation radius and Lindblad resonances in density wave theory.

Assuming a fixed pattern speed of the density wave and differential rotation of stars and gas, there are certain locations in a disk galaxy where resonances occur. In a corotating frame with $\Omega' = \Omega - \Omega_p$, the epicyclic orbits are closed if $\Omega' = \kappa/m$ with m the number of spiral arms. In this case, stars and gas are moving in resonance with the pattern speed. For $m = 2$ this resonances are called *Lindblad resonances* and defined as:

$$\Omega_p = \Omega - \kappa/2 : \text{ the inner Lindblad resonance (ILR),} \quad (2.1)$$

$$\Omega_p = \Omega + \kappa/2 : \text{ the outer Lindblad resonance (OLR).} \quad (2.2)$$

The corotation radius is located where density wave and gas and stars move at the same angular velocity $\Omega_p = \Omega$.

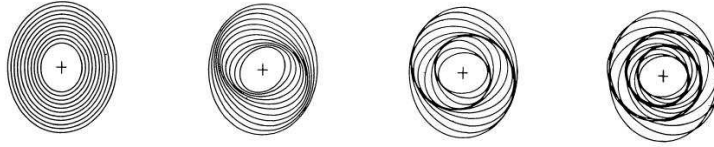


Figure 2.7: *Spiral patterns created by small differences in the pattern speed Ω_p in the different orbits.*

One way to explain the existence of spiral patterns is the following simple approach. Assuming every orbit (rotating with Ω_p) produces closed ellipses in the corotating frame, the equation $\Omega_p = \Omega - \kappa/2$ holds. If Ω_p is nearly constant or slightly different for all orbits, the spiral pattern performs a rigid rotation without winding up of the spiral arms as illustrated in Fig. 2.7. The assumption of a nearly constant Ω_p holds in the Milky Way over a large range from galactocentric radii of 3 to 20 kpc. The frequent occurrences of two-armed spiral patterns, as very prominently seen in the grand-design galaxy M51 (detailed analysis of this source later), have been explained by Kalnajs (1973) using this approach.

Especially near the ILR, density waves are strongly damped through interaction with the accumulated matter and often do not reach the corotation radius. A reflection at the ILR creates a leading wave with respect to the spiral pattern but the trailing wave is strongly amplified by up to a factor of 10. This phenomenon is called *swing amplification* (see Fig. 2.9) and presents one plausible scenario for the fact that most observed spiral arms are trailing with respect to the direction of rotation (e.g. Mark 1976; Goldreich & Tremaine 1978).

Note that the density wave theory by Lin & Shu (1964) does not take into account the self-gravity of the density wave and is in that sense not self-consistent. Toomre (1977) reviews the theories of spiral structure based on the Lin and Shu approach in great detail. The density wave theory provides a number of mechanisms to explain the observed variety in spiral galaxies but none of them is able to account for all observed galaxy types.

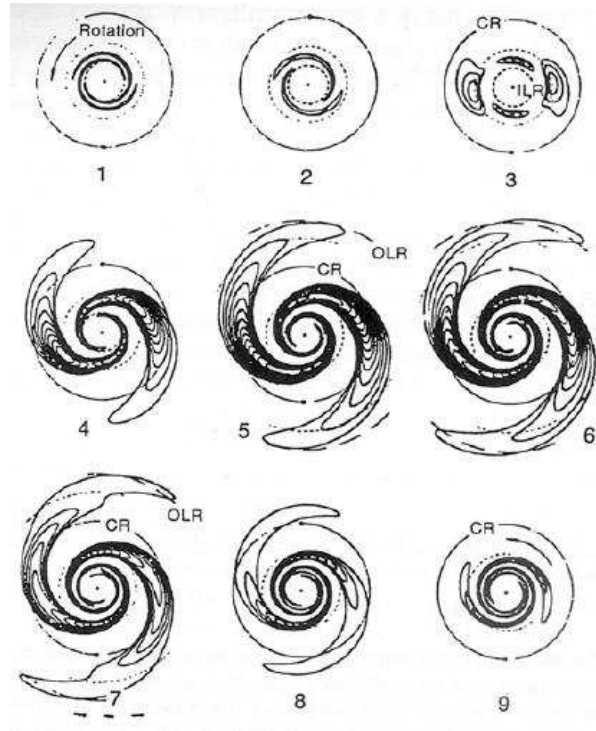


Figure 2.8: Sketch of the mechanism of swing amplification of a density wave mode as presented in Toomre (1981).

Triggering The triggering mechanism of the density wave is at the moment not fully understood. One plausible scenario is a density wave from a bar (Huntley et al. 1978) or the interaction with a neighbor galaxy which induces a transitory density wave. In the case of the M51 system, Toomre & Toomre (1972) numerically modeled the passage of the companion NGC5195. The model reproduces the overall observed structure of the system but differs significantly in the central part. A possible reason for this is that self-gravity has been neglected in this model. Garcia-Burillo et al. (1993a) performed 3D Monte Carlo simulations of the interacting M51 system, neglecting self-gravity. The modeled velocity field matches very well with an observed CO-velocity field. However, this mechanism can only explain spiral arms in galaxies with a nearby companion.

There exist alternative models to the density wave approach which can

explain spiral structure. Models based on stochastic star formation have been successful in producing the fragmented and flocculent structure observed in some spiral galaxies (Goldreich & Lynden-Bell 1965; Sellwood & Carlberg 1984). Magnetohydrodynamic theories discussed in the 1950s failed to explain modern observational results.

After the sections summarizing the morphology of galaxies and possible mechanisms creating the observed spiral arm structure, we will next introduce mechanisms governing the locations of star formation in a particular galactic disk.

2.3 Disk stability

An important parameter for the understanding of star formation in disk galaxies is the local stability against gravitational collapse. Gaseous and stellar disks are stable against non-axisymmetric disturbances (Goldreich & Lynden-Bell 1965; Julian & Toomre 1966). For axisymmetric perturbations ($m = 0$) in a gaseous disk rotating at a fixed angular frequency Ω , the dispersion relation is analogous to the dispersion relation leading to the *Jeans criterium*, describing the stability of a gas cloud against collapse:

$$\omega^2 = 4\Omega^2 - 4\pi G\rho_0 + k^2 v_s^2, \quad (2.3)$$

where ρ_0 is the volume density and v_s the speed of sound. In the case of the *Jeans criterium* this leads to a critical wavelength λ_{crit} , which is the minimum wavelength leading to instability and collapse of the gas into stellar condensation: $\lambda_{crit} = (\frac{\pi}{G\rho_0})^{1/2} v_s$.

Disk galaxies are close to the special case of a very thin differentially rotating disk and we can replace the density term $4\pi\rho_0$ by $2\pi G\Sigma_{gas}$. Here we first consider the pure gaseous disk following the Toomre approach. Σ_{gas} is a surface mass density (measured in units of $M_\odot \text{pc}^{-2}$). Inserting the previously defined epicyclic frequency κ , the dispersion relation for axisymmetric

disturbances in the plane of the disk is:

$$\omega^2 = \kappa^2 - 2\pi G \Sigma_{\text{gas}} |k| + k^2 v_s^2. \quad (2.4)$$

k is the wave number and v_s the speed of sound of the gas. This relation also uses the tight-winding assumption: to first order the long-range coupling of the gravitational force can be neglected (e.g. Kalnajs 1973). Solving this quadratic equation, we see that a gaseous disk is stable against axially symmetric disturbances for

$$Q_{\text{gas}} = v_s \kappa / (\pi G \Sigma_{\text{gas}}) > 1. \quad (2.5)$$

Q_{gas} is the *Toomre stability parameter* (Toomre 1964). For a pure stellar disk the stability parameter is similar. From equation 2.5 we see that gravity drives the disk towards collapse while velocity dispersion and the epicyclic motion hinder this collapse. For $Q_{\text{gas}} > 1$ the disk is stable against gravitational perturbations, while for $Q_{\text{gas}} < 1$ the disk is unstable.

In a *real-life* galaxy we will have interaction of the stellar and gaseous components. The interaction complicates the treatment of the gravitational stability of the disk. Stars and gas are treated as two different isothermal fluids (Wang & Silk 1994). The dispersion relation for two isothermal fluids is presented e.g. in Jog & Solomon (1984). Wang & Silk (1994) derive a linear approximation in the stellar and gaseous wavenumber $k_{s,g}$ for the total Toomre Q parameter:

$$Q_{\text{total}}^{-1} = Q_{\text{gas}}^{-1} + Q_{\text{stellar}}^{-1}. \quad (2.6)$$

The impact of the stellar contribution on the total disk stability can be significant and we come back to this in the special case of M51 in a later chapter.

2.4 Kennicutt-Schmidt law

Next, we will discuss an empirically determined relationship of gas density and star formation rate. A summary of the most recent results in this field

is contained in the annual review by McKee & Ostriker (2007). The star formation rate $\dot{\Sigma}_{\text{SFR}}$, i.e. the stellar mass density created in a certain time interval, and the total gas density have been studied in large samples of galaxies. A star formation rate is typically given in units of $M_{\odot} \text{pc}^{-2} \text{Gyr}^{-1}$. A fundamental physical quantity associated with a star formation rate is the star formation efficiency $\epsilon_{\text{sfr}} = \dot{\Sigma}_{\text{SFR}}/\Sigma_{\text{gas}}$, the ratio of star formation rate and available gas density. ϵ_{sfr} describes how quickly gas is converted into stars typically in units of Gyr^{-1} . The inverse quantity is the so called *gas depletion time* and quantifies the time-scale on which the whole gas reservoir is converted into stars, assuming a constant star formation efficiency over time.

The star formation rate can be deduced from the far-infrared (FIR) dust continuum emission. Parts of the FIR emission is related to current star formation as it traces young stars forming embedded in molecular clouds (Yun et al. 2001). A non-star formation contribution to the FIR stems from cold cirrus emission which contributes to the total FIR emission with varying fraction in different galaxies (Helou 1986). Helou (1986) uses IRAS¹-data to conclude that in most galaxies the FIR traces massive young stars but there are galaxies where the cirrus component dominates.

Another tracer for the star formation rate is 20 cm radio continuum emission, which consist mainly of non-thermal synchrotron emission radiated by cosmic rays interacting with magnetic fields. The sources of the cosmic rays are supernovae remnants and thus trace high-mass star formation. We use empirical relations between non-thermal synchrotron emission and supernovae rate following Condon (1992). Note, that a tight correlation of FIR and radio continuum emission has been found in many sources (Condon 1992). We discuss the radio continuum as a tracer for star formation in the case of M51 in more detail later.

The most widely studied empirical law linking star formation rate and gas density is the *Kennicutt-Schmidt law* (Schmidt 1959; Kennicutt 1998). It assumes a powerlaw dependence of the star formation rate on the gas density:

$$\dot{\Sigma}_{\text{SFR}} = A \Sigma_{\text{gas}}^n. \quad (2.7)$$

¹Infrared Astronomical Satellite

In this description, star formation rate and gas density are usually averaged over the whole galaxy or azimuthally averaged over an annulus of a certain width. This may introduce averaging over areas with very different star formation rates and gas densities and thus results must be taken with caution.

The empirically determined Kennicutt-Schmidt law is also found in models, as e.g. set up by Elmegreen (1994) where self-gravity as well as magnetic fields are considered. The average star formation rate will depend on the volume efficiency for star formation ϵ , the instability due to gravity (with varying degree depending on the strength of the magnetic field) and the available volume gas density ρ_{gas} . For reasonable assumptions, Elmegreen (1994) derive a volume Kennicutt-Schmidt law of $\rho_{\text{SFR}} \propto \rho_{\text{gas}}^{1.5}$.

The Schmidt law was globally studied by Kennicutt (1998) in a sample of 88 galaxies. In this paper, the star formation rate and the gas densities were averaged over the complete galaxy.

Improving on the global averaging, radially averaged Schmidt law studies followed. E.g. Wong & Blitz (2002); Boissier et al. (2003); Heyer et al. (2004) studied the radially averaged Schmidt law in individual galaxies. The powerlaw indices of the observed Schmidt laws show a range of 1.2-2.5.

Alternative descriptions for the Schmidt law are proposed in recent publications. E.g. Wong & Blitz (2002) found a good correlation of the star formation rate with an H_2 Schmidt law, namely a correlation of the star formation rate density with molecular gas density in the disk of their galaxies, neglecting the atomic component of the gas density.

High resolution sub-kpc studies in different regions of a sample of 15 galaxies done by Bigiel et al. (2007) also indicate a tight correlation of the H_2 gas with the star formation rate.

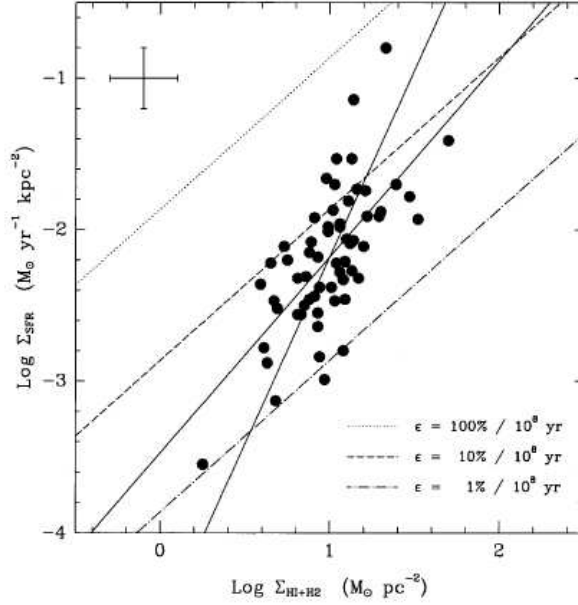


Figure 2.9: Relation of the global star formation rate Σ_{SFR} and the gas density Σ_{gas} in 61 normal spirals from the sample studied in Kennicutt (1998). Dashed and dotted lines indicate relations for constant global star formation efficiency.

2.5 Radiative transfer

In this section, the determination of physical properties from line intensities using radiative transfer model's is explained. In particular the escape probability formalism is summarized which we use in the following to study the central regions in the southern galaxies Circinus and NGC4945 in chapter 4. For a more comprehensive discussion on radio-astronomical quantities and their derivation see Stutzki (2001).

The comparison of intensities of different line transitions of a molecule enables to determine the excitation conditions in the observed region. In the case of *local thermodynamic equilibrium* (LTE) the level population follows a Boltzmann distribution and only depends on the temperature. In general, the interstellar medium is not in LTE and more complex mechanism are needed to obtain e.g. density and temperature in an observed region.

In the case of line emission of molecules, two fundamental mechanisms govern the level populations: the excitation through collisions and radiative excitation.

2.5.1 Collisional excitation

Due to the overwhelmingly dominant abundance of H_2 in molecular clouds, only collisions with H_2 as a partner must be considered. We consider the transition of a molecule from a state i to j . The collision rate C_{ij} is proportional to the density of H_2 molecules $n(\text{H}_2)$ and the collision coefficient γ_{ij} :

$$C_{ij} = n(\text{H}_2)\gamma_{ij}. \quad (2.8)$$

γ_{ij} itself is the thermal average of the product of scattering cross section σ_{ij} of the molecule and the thermal velocity v of its scattering partners: $\gamma_{ij} = \langle \sigma_{ij}v \rangle$.

For a two-level system with upper state u and lower state l , the change of the upper level population n_u is

$$\frac{dn_u}{dt} = -n_u C_{ul} + n_l C_{lu}, \quad (2.9)$$

the equivalent holds for the lower level. The particle number is conserved:

$$\frac{dn_u}{dt} = -\frac{dn_l}{dt}. \quad (2.10)$$

Thus, in equilibrium we get:

$$\begin{aligned} n_u C_{ul} &= n_l C_{lu}, \\ \frac{n_u}{n_l} &= \frac{C_{lu}}{C_{ul}} := \frac{g_u}{g_l} \exp\left(-\frac{E_u - E_l}{kT_{\text{ex}}}\right). \end{aligned} \quad (2.11)$$

The coefficients g_u, g_l are the statistical weights of the corresponding levels. Equation 2.11 defines the excitation temperature T_{ex} .

This definition is motivated by the fact that if the level population is thermalized, the excitation temperature is the kinetic temperature $T_{\text{ex}} = T_{\text{kin}}$.

In the more general case of a multi-level system, all pairwise excitation temperatures of the different transitions equal the kinetic temperature.

The above relation thus links the up-, and downward collisional rates with the kinetic temperature of the collision partners. Although derived for the case of the thermal equilibrium with the collisional partners, the left side, i.e. the ratio of rate constants, is a microscopic property and the relation also holds off thermal equilibrium. This, at first hand, surprising connection is also called *detailed balance relation*.

The fundamental reason for this is *micro-reversibility*, i.e. the probability of a transition is identical for forward and backward collisions of the scattering partners in the case of identical quantum numbers. For more details see also Stutzki (2001).

Next, we will discuss radiative excitation before combining both processes in the rate equation.

2.5.2 Radiation mechanisms

For simplicity we again introduce all processes for a two level system with levels l and u. The population of the levels will depend on the emission probability from the upper level to the lower level (*Einstein coefficient* A_{ul}) and stimulated emission. Stimulated emission from the upper to the lower level is characterized by the Einstein coefficient B_{ul} and the mean intensity J_ν . Additionally, absorption of photons will populate the upper level depending on B_{lu} and J_ν . The frequency at absorption and emission will not exactly correspond to the energy difference of the levels. Due to pressure broadening, the intrinsic line width caused by the Heisenberg uncertainty principle (resulting in a Lorentzian line profile) and thermal and turbulence broadening (resulting in a Gaussian line profile), the line profile $\phi(\nu - \nu_0)$ is a Voigt profile.

Volume emissivity η_ν and absorptivity χ_ν for this system are then given via:

$$\eta_\nu(\mathbf{r}) = h\nu/4\pi A_{ul}n_u\phi(\nu - \nu_0), \quad (2.12)$$

$$\chi_\nu(\mathbf{r}) = h\nu/4\pi (B_{lu}n_l - B_{ul}n_u)\phi(\nu - \nu_0). \quad (2.13)$$

depending on the density in the upper and lower levels. The source function $S_\nu = \eta_\nu/\chi_\nu = A_{ul}/(B_{lu}n_l/n_u - B_{ul})$ thus only depends on the ratio of population in the levels. The source function is a Planck-function depending on the excitation temperature T_{ex} :

$$S_\nu = \frac{2h\nu^3}{c^2} \frac{1}{\exp(h\nu/kT_{\text{ex}}) - 1} = B_\nu(T_{\text{ex}}). \quad (2.14)$$

T_{ex} is defined via the population of two levels, which follows a Boltzmann distribution: $\frac{n_u}{n_l} = \frac{g_u}{g_l} \exp(h\nu/kT_{\text{ex}})$ (see above).

A line intensity at a position \mathbf{r} in the direction \mathbf{n} is given via the formal solution of the radiative transfer equation:

$$I_\nu(\mathbf{r}, \mathbf{n}) = I_{\nu,bg,S} \exp(-\tau_{\nu 0}(\mathbf{r}, \mathbf{n})) + \int_0^{\tau_{\nu 0}} S_\nu(\tau'_\nu) \exp(\tau'_\nu) d\tau'_\nu \quad (2.15)$$

$I_{\nu,bg,S}$ is the background intensity along the line of sight for the line frequency ν , τ_ν is the optical depth and $\tau_{\nu 0}$ the optical depth in the line center. S_ν is the source function, discussed above. As S_ν will depend on I_ν , solving the formal radiative transfer equation needs some simplifying assumptions:

Excitation temperatures T_{ex} of different line transitions are assumed to be spatially constant in the whole source. The optical depth along the line of sight is taken to be $\tau_{\nu,S} = \tau_{\nu,0} \Delta\nu \phi(\nu - \nu_0)$ with the line profile normalized to $\int \phi(\nu) d\nu = 1$. For frequencies beyond the line profile $\nu_t - \nu \gg \delta\nu$: $\tau_{\nu,S} = 0$ and $I_\nu = I_{t,bg}$. $I_{t,bg}$ is the background continuum radiation which contains at least the contribution of the cosmic microwave background at 2.7 K. The observed line intensity as the difference of line and continuum emission in direction \mathbf{r}, \mathbf{n} is given in the so called *detection equation*:

$$I_{\nu,l} = (S_\nu - I_{t,bg})(1 - \exp(\tau_{\nu,S})). \quad (2.16)$$

The source function and optical depth are determined from the excitation temperature T_{ex} and one level population, e.g. of the upper level. Before the *escape probability approximation* is discussed, we first introduce the *rate equation* for a multi-level system which describes the local level population.

2.5.3 Rate equation

Next, we discuss the rate equation for the general case of a multilevel system. The level population will be determined from radiative and collisional excitation and deexcitation. The rate equation describes the change in local level population for the level i :

$$0 = \frac{dn_i}{dt} = \sum_t (\delta_{u_t, i} [n_{u_t} A_t + n_{u_t} J_t B_{u_t, l_t} - n_{l_t} J_t B_{l_t, u_t}] + \delta_{l_t, i} [n_{u_t} A_t + n_{u_t} J_t B_{u_t, l_t} - n_{l_t} J_t B_{l_t, u_t}]) - \sum_{j>i} [n_i C_{ij} - n_j C_{ji}] + \sum_{j<i} [n_i C_{ij} - n_j C_{ji}]. \quad (2.17)$$

The index t symbolizes the sum over all radiative transitions connecting to level i . Thus, the local level population depends on the local radiation field J_t , and the collision rates. The collision rates itself depend on the density ($n(\text{H}_2)$) and the kinetic temperature T_{kin} which itself determines the thermal (Maxwell) velocity distribution.

Solving this coupled system of equations and the formal solution of radiative transport in equation 2.15 is only possible iteratively and numerically as it contains non-local dependencies. We use the escape probability model e.g. as introduced by Stutzki & Winnewisser (1985) and will briefly explain the assumptions of the escape probability approach.

As assumed for the derivation of the detection equation, the excitation temperatures T_{ex} are taken to be spatially constant. Thus, effectively the mean excitation temperatures in the source are considered. The escape probability $\beta_\nu(\mathbf{r}, \mathbf{n}) = \exp(-\tau_{\nu,0}(\mathbf{r}, \mathbf{n}))$ describes the fraction of photons escaping the

cloud from \mathbf{r} in direction \mathbf{n} . The assumption of isotropic background radiation and a constant background intensity and source function within the line width makes the calculation of the steradian averaged escape probability easier. The mean intensity is then given as

$$J_\nu(\mathbf{r}) = (1 - \beta_\nu(\mathbf{r}))S_{\nu 0} + \beta_\nu(\mathbf{r})J_{\nu 0, bg}. \quad (2.18)$$

As S_ν , J_ν are considered constant with frequency, they were replaced with $S_{\nu 0}$, $J_{\nu 0}$. The frequency dependence of the optical depth is determined from the normalized profile function $\phi(\nu_0) = \phi(\nu - \nu_0)$ as above yielding $\phi(\nu_0)(\nu = \nu_0) = 1/\Delta\nu$. Frequency averaging weighted with the profile function yields:

$$J_t(\mathbf{r}) = (1 - \beta_t(\mathbf{r}))S_{\nu 0} + \beta_t(\mathbf{r})J_{\nu 0, bg}, \quad (2.19)$$

with the line-averaged escape probability:

$$\begin{aligned} \beta_t(\mathbf{r}) &= \int \beta_\nu(\mathbf{r})\phi(\nu - \nu_0)d\nu \\ &= \int d\nu \int d\mathbf{n}^2 \phi(\nu - \nu_0)\exp(-\tau_{\nu, 0}(\mathbf{r}, \mathbf{n})\Delta\nu\phi(\nu - \nu_0)). \end{aligned} \quad (2.20)$$

Using the escape probability approximation, the rate equation system gets less complicated as the non-local dependency of the mean intensity on the level population (via source-function and optical depth) is simplified to a dependence on local level populations.

However, the escape probability approach is not self-consistent. The line-averaged escape probability is varying with the location, which results in a spatial variation of the mean intensity and thus (via the rate equation) in level populations varying with location. This is not consistent with the assumption of a constant source function.

Redefining the source function (or excitation temperatures respectively) by an effective mean source function and similarly the escape probability, this inconsistency can be overcome. Using analogous a typical mean optical depth, the escape probability is given as:

$$\beta_t(\tau_{\nu 0}) = \int (-\tau_{\nu 0}\Delta\nu\phi(\nu_t - \nu))\phi(\nu_t - \nu)d\nu. \quad (2.21)$$

The escape probability formalism with its assumption of a mean source function thus gives a local dependence of source function and mean intensity.

2.5.4 Critical density

As collisional and radiative processes enter into the rate equation, one can estimate for a given line transition t , which process dominates at a certain density n_{H_2} . The following considerations are made for the case of a two-level system: we use the escape probability approximation and the mean background intensity is expressed via a blackbody temperature T_{rad} . The rate-equation in this case yields the following relationship:

$$\exp(-h\nu/kT_{\text{ex}}) = \frac{\exp(-h\nu/kT_{\text{kin}}) + \exp(-h\nu/kT_{\text{rad}}) \times n_{\text{eff}}^*/n_{\text{H}_2}}{1 + n_{\text{eff}}^*/n_{\text{H}_2}} \quad (2.22)$$

The critical density n^* of a molecular transitions and the effective critical density n_{eff}^* are defined as:

$$n^* = \frac{A_t}{\gamma_{\text{ul}}}, \quad n_{\text{eff}}^* = \frac{\beta_t}{1 - \exp(-h\nu/kT_{\text{rad}})} n^*. \quad (2.23)$$

The critical density defines the density at which the spontaneous emission described by the Einstein-A coefficient is equal to the collisional deexcitation.

For a given molecular transition with a critical density n^* , at densities $n_{\text{H}_2} \gg n^*$, collisional processes dominate $T_{\text{ex}} \approx T_{\text{kin}}$. The system is in an LTE state and the level population follows a Boltzmann distribution at temperature T_{kin} . Even if the system is not in LTE, trapping of photons due to high optical thickness can reduce the effective critical density by the escape probability factor β_t . Analogous, a high background radiation temperature T_{rad} increases the effective critical density.

In the case of $n_{\text{H}_2} \ll n^*$, the radiation temperature T_{rad} of the background will determine the level population, as radiative processes dominate. Only in the case of a two-level system the transition from T_{rad} to T_{kin} with increasing density occurs monotonously.

The critical density e.g. for the CO 2-1 molecular transition at $T_{\text{kin}} = 40$ K is $1.5 \cdot 10^4 \text{cm}^{-3}$ decreasing to $8.2 \cdot 10^3 \text{cm}^{-3}$ at $T_{\text{kin}} = 100$ K (Flower & Launay 1985). The analysis of CO and [C I] intensities in the southern galaxies Circinus and NGC4945 using radiative transfer calculations in the escape probability formalism (Stutzki & Winnewisser 1985), will be presented in chapter 4.

Chapter 3

The nearby galaxy M51 - a laboratory to study the onset of star formation

Parts of this chapter have been published in

- Schuster, K., Kramer, C., Hitschfeld, M., Garcia-Burillo, S. and Mookerjea, B., *Astronomy & Astrophysics*, 2007, in press,
- Hitschfeld, M., Kramer, C., Schuster, K., Garcia-Burillo, S. and Stutzki, J., *Astronomy & Astrophysics*, 2008, submitted.

In this chapter, the spiral galaxy M51 is used as a sample source to investigate the distribution of atomic and molecular gas, empirical star formation relations also found in other galaxies and the gravitational stability of the disk according to the Toomre criterion. Due to its proximity and inclination, M51 is an ideal target to study the conditions and efficiency at which it forms stars from the gas. First, the widely studied astronomical source M51 is introduced, including previous results in the context of this thesis.

3.1 Introduction to M51

M51 is an interacting, grand-design spiral galaxy at a distance of only 8.4 Mpc seen nearly face-on (Table 3.1). It is rich in molecular gas, most of which is found in the two very prominent spiral arms which are presumably caused by the tidal interaction (Tully 1974a; Howard & Byrd 1990; Toomre & Toomre 1972).

Table 3.1: *Basic properties of M51. References: ^a RC3 catalogue de Vaucouleurs et al. (1991), ^b Feldmeier et al. (1997), note that Takáts & Vinkó (2006) recently reported a distance of only 7.1 ± 1.2 Mpc, ^c Tully (1974b).*

	M51
RA(2000)	13:29:52.7
DEC(2000)	47:11:43
Type	SA(s)bc pec ^a
Distance [Mpc]	8.4 ^b
11'' correspond to	448 pc
Heliocentric velocity [kms ⁻¹]	463 ^a
Position Angle [°]	170 ^c
Inclination [°]	20 ^c

Kinematic studies reveal unusually large streaming motions implying a strong density wave and the presence of galactic shocks (Aalto et al. 1999). The [C II] map of Nikola et al. (2001) shows two secondary lobes of emission to the northeast and southwest near the corotation radius of the density wave pattern, presumably due to cloud-cloud collisions, stimulating star formation. Calzetti et al. (2005) combine Spitzer infrared data of IRAC¹ and the MIPS² with UV data from the GALEX³. These data are used to discuss the various tracers of star formation in M51. Enhanced star formation activity at the two lobes seen in [C II] is probably triggered by the interaction (Nikola et al. 2001). This is also indicated

¹Infrared Array Camera

²Multi Imaging Photometer for Spitzer

³Galaxy Evolution Explorer

by disk simulations of Toomre & Toomre (1972) which show tidal tails emerging from the disk at the positions of enhanced star formation. VLA⁴ observations of the HI line show a prominent tail outside the main disk extending to the south and east, and covering more than 25', i.e. 100 kpc, in projected distance (Rots et al. 1990) (cf. Tilanus & Allen 1991). Meijerink et al. (2005) find that a major fraction of cold dust emission at 850 μm stems from an extended exponential disk with a scale length of 5.45 kpc, possibly also tracing total gas column densities. The kinematics of H α emission of M51 were recently studied by the SINGS⁵ team (Daigle 2006), improving on the work of Tilanus & Allen (1991).

The relative importance of the different components of the interstellar medium was addressed by Nikola et al. (2001) when trying to explain the mapped [C II] emission using modeling of *photon dominated regions* (PDRs). In a recent study comprising all major cooling lines of the molecular gas, i.e. those of [C II], [O I], CO, and [C I], at selected spiral arm positions and the center of M51, Kramer et al. (2005) conclude that the bulk of the emission stems from clumpy PDRs. Only about 15–30% of the [C II] emission stems from dense H II regions. The [C I] and CO emission of the center region have also been studied by Israel et al. (2006); Israel & Baas (2002); Gerin & Phillips (2000). Schinnerer et al. (2004) mapped two distinct regions in the spiral arms of M51 in HCN, HCO⁺ and other tracers of the chemistry. Rydbeck et al. (2004) presented a large CO 1–0 map of M51 obtained at the Onsala-20m telescope. The inner region of M51 were previously mapped in CO 1–0 with the FCRAO-14m⁶, IRAM-30m, and NRO⁷-45m telescopes by Scoville & Young (1983); Lord & Young (1990); Garcia-Burillo et al. (1993b); Nakai et al. (1994); Kuno et al. (1995a); Kuno & Nakai (1997). These single-dish observations reveal the large-scale emission for which interferometric observations are not sensitive. OVRO⁸ was used to create CO 1–0 maps by Rand & Kulkarni (1990) and Aalto et al. (1999). Helfer et al. (2003) used BIMA⁹ in combination with NRAO¹⁰-12m single-dish data to

⁴Very Large Array

⁵Spitzer Infrared Nearby Galaxies Survey

⁶Five College Radio Astronomy Observatory

⁷Nobeyama Radio Observatory

⁸Owens Valley Radio Observatory

⁹Berkeley Illinois Maryland Association

map the inner part of M51 in CO 1–0.

Shetty et al. (2007) recently presented a detailed 2D study of the velocity field of M51 using interferometric CO 1–0 data at $6''$ resolution and Fabry-Perot $H\alpha$ data. Henry et al. (2003) studied the strong density wave in M51 and speculate that it is a superposition of different modes.

3.2 IRAM-30m HERA-Observations

3.2.1 ^{12}CO 2–1

In the context of this thesis, the raw data of ^{12}CO 2–1 observations of M51 with the IRAM-30m were reduced and analyzed. The M51 observations were a collaborative effort of C. Kramer, B. Mookerjea and J. Stutzki (KOSMA) and K. Schuster (IRAM, France). The data reduction was done using the CLASS and GREG programs, which are part of the GILDAS¹¹ software package.

The observations of the ^{12}CO 2–1 emission from M51 were conducted with the IRAM-30m telescope in February 2005 using the 18 element focal plane heterodyne receiver array HERA (Schuster et al. 2004) together with the WILMA¹² auto correlator backend. WILMA has a channel spacing of 2.6 kms^{-1} (2 MHz) and a bandwidth of 1200 kms^{-1} (930 MHz). Pixel 2 of the second HERA polarization showed excess noise and was ignored from further analysis.

Observations were conducted in position switched *on-the-fly* (OTF) mode scanning M51 in right ascension. Sampling was $6''$ in RA. HERA was rotated by 18.5° to obtain a spacing of $7.6''$ in declination between adjacent scan lines (Schuster et al. 2004). This corresponds to near Nyquist sampling for a half power beamwidth (HPBW) of $11''$. The resulting map in ^{12}CO 2–1 has a size of $11' \times 11'$. Fig. 3.1 shows the $7' \times 10'$ sub-region where CO was

¹⁰ National Radio Astronomy Observatory

¹¹ <http://www.iram.fr/IRAMFR/GILDAS>

¹² Wideband Line Multiple Autocorrelator

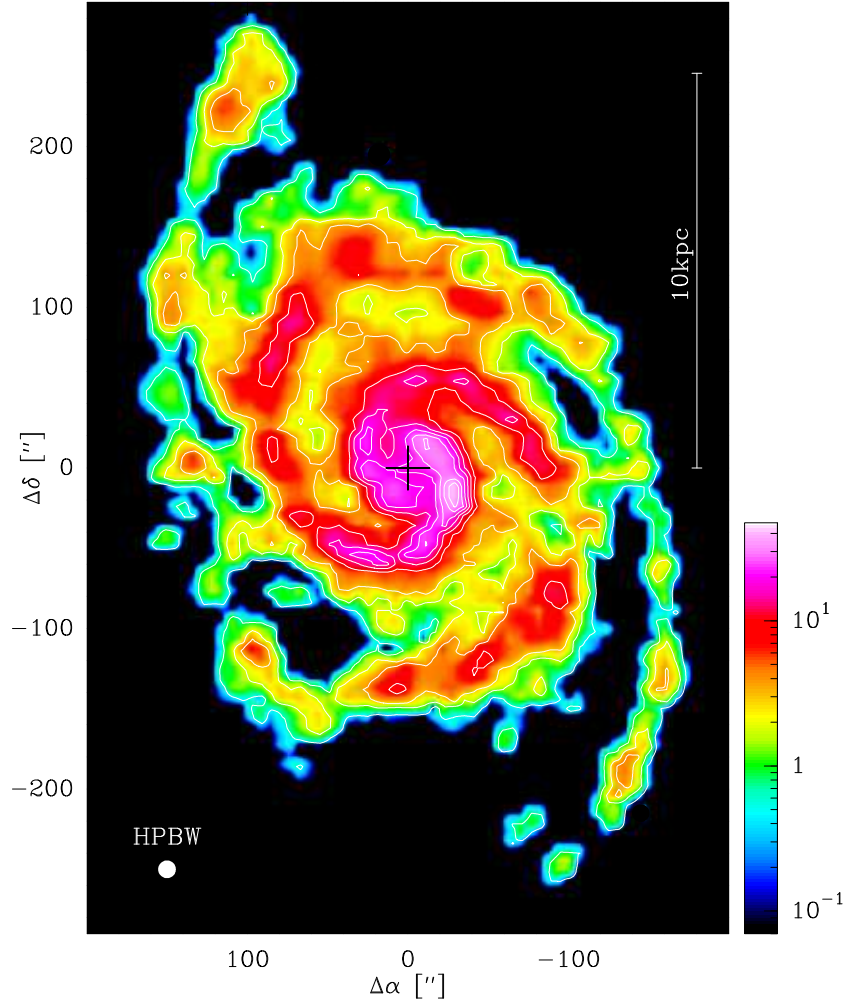


Figure 3.1: Map of ^{12}CO 2-1 integrated intensities [Kkm s^{-1}] showing M51 and its companion galaxy NGC 5195 in the north-east. The image has a resolution of $11''$ and is constructed from a masked moment calculation integrating over the full kinematic extent of M51, $350 \text{ km s}^{-1} < v_{\text{lsr}} < 600 \text{ km s}^{-1}$ (see section 3.3.1). Color coded intensities are on a logarithmic scale. The cross marks the 0/0 center position at (eq.2000) The noise level is $1\sigma = 0.65 \text{ Kkm s}^{-1}$. Contours range in units of 1σ from 1, 3, 6, 16 to 56 in steps of 10. The peak intensity is 47.3 Kkm s^{-1} . All intensities are on the T_{A}^* scale.



Figure 3.2: ^{12}CO 2–1 and ^{13}CO 2–1 observations were conducted with the IRAM-30m telescope on Pico Veleta, Sierra Nevada.

detected. An emission-free reference position was selected at offsets $(10', 0')$. The ^{12}CO 2–1 mean baseline rms is 18 mK at 5 km s^{-1} velocity resolution on the T_{A}^* scale. To correct to first order for the telescope efficiencies, i.e. to go from the T_{A}^* scale to the T_{mb} scale, we simply multiplied the antenna temperature data with the ratio of forward efficiency $F_{\text{eff}} = 0.91$ over main beam efficiency $B_{\text{eff}} = 0.52$. These numbers show that the mapped spatial structure of M51 is to some extent smeared out by the error beams of the IRAM-30m telescope (Greve et al. 1998) - this will be later discussed in more detail.

3.2.2 ^{13}CO 2–1

The observations of the ^{13}CO 2–1 emission in the north-western inner spiral arm of M51 were conducted with the IRAM-30m telescope in January 2007. The ^{13}CO 2–1 M51 observations were carried out and reduced by me and C. Kramer.

We used the HERA receiver array together with the WILMA auto correlator backend. Observations were conducted in position switched OTF mode scanning along the north eastern spiral arm in M51. An emission-free reference position at offsets $(10', 0')$ was chosen. A $68'' \times 138''$ -map with

a sampling of $6''$ was observed. σ corresponds to 0.36 Kkms^{-1} at 5 kms^{-1} velocity resolution on the T_{A}^* scale.

Fig. 3.4 shows the integrated intensity of ^{13}CO 2–1 in the entire north-eastern spiral arm region where we detected ^{13}CO 2–1 emission in M51. The observed spectra are shown in Fig. 3.3.

3.2.3 Complementary data

We briefly present the complementary data used in the determination of the Schmidt law and the gravitational stability analysis of the disk of M51. The HI-data trace the atomic component, *K*-Band emission is a possible tracer for the stellar component of the galaxy. Radio continuum emission was used for the derivation of the star formation rate. We compare the distribution of the total gas density in M51 to the structure of the dust emission using $850\mu\text{m}$ -data. The observations of the different tracers are presented next.

HI We use data of the HI Nearby Galaxy Survey (THINGS) (Walter et al. 2005, 2008). M51 was observed in the VLA D, C, and B array configurations and presented in Kennicutt et al. (2007). In D-configuration the interferometer is sensitive to scales of $15'$ and thus we expect to detect almost the total flux for M51. The angular resolution in the integrated intensity image is $5.86'' \times 5.56''$. The sensitivity of the THINGS data is 0.44 mJy/beam for 5.2 km/s channel width (Walter et al. 2008). Rots et al. (1990) obtained 1.4 mJy/beam for a similar beam size but 10.3 km/s channel width. This a factor of 4 higher compared to THINGS at the same velocity resolution.

Radio continuum For the derivation of the star formation rate in a later section, we use a map of radio continuum intensities at 20 cm (Patrikeev et al. 2006). The observations were carried out with the VLA in C+D configuration. The angular resolution of the M51 map is $15''$ resolution.

***K*-Band** To derive stellar densities, we used the *K*-Band images of the *Two Micron All Sky Survey* (2MASS) Large Galaxy Atlas (Jarrett et al. 2003). The 2MASS M51 image has an angular resolution of $3''$.

850 μ m dust emission Meijerink et al. (2005) present 850 μ m dust emission observations of M51 with SCUBA¹³ at the JCMT. In the final background subtracted and calibrated image, the FWHM is $15''$ and the rms is 9 mJy/beam. For details on calibration and observation techniques see Meijerink et al. (2005).

3.3 Observational results

In this section, the local distribution of the different observed emission lines in the disk of M51 is presented and described. These data are of fundamental importance in the later analysis parts and are thus presented in great detail.

3.3.1 Integrated intensity map using the masked moment method

To create the integrated intensity map of the ^{12}CO 2–1 data (Fig. 3.1) and ^{13}CO 2–1 data (Fig. 3.4), we used the masked moment integration method presented in Adler et al. (1992). This technique minimizes the noise contribution from emission-free channels within the chosen velocity range. In M51 the full velocity range of emission is $350 \text{ km s}^{-1} < v_{\text{lsr}} < 600 \text{ km s}^{-1}$. The integrated intensity or zeroth moment M_0 is defined as

$$M_0 = \sum_v T_v, \quad (3.1)$$

where T_v is the v -th channel intensity map and the sum is carried out over a specific velocity interval.

¹³Submillimetre Common-User Bolometer Array

The masking method requires additionally for each pixel i a mean value $\langle T_v^i(x, y) \rangle$ above a threshold in a specified volume surrounding the pixel. Only if the average value $\langle T_v^i(x, y) \rangle$ for the actual volume is above the specified threshold, the center value of the volume $T_v^i(x, y)$ is added in the sum of the zeroth moment M_0 . The threshold value is typically between $1-2\sigma$ of the map (Adler et al. 1992). We used a 2σ threshold for the ^{12}CO 2–1 data of M51. The volume for a given pixel are the neighbor pixels (in 3D).

3.3.2 Molecular gas distribution

The HERA map of ^{12}CO 2–1 (Fig. 3.1) is the first CO map of M51 encompassing the companion galaxy as well as the south-western arm out to a radius of ~ 12 kpc in a homogeneously sampled data set at linear scales of down to 450 pc.

The emission detected with the 30m telescope traces the well known two-armed spiral pattern out to the companion galaxy NGC 5195, which shows up brightly in the north-east at ~ 10.5 kpc radial distance, and out to the south-western tip of the second arm at the opposite side of M51. The outer parts of the two arms in the west and in the east appear more fragmented than the inner parts. The western arm especially is almost unresolved. Inter-arm emission is detected above the 3σ level out to radii of about 6 kpc. Several spoke-like structures connect the spiral arms radially.

CO-to- H_2 conversion in M51 To estimate e.g. the total H_2 column densities from the integrated CO 2–1 intensities later used for the map of the total gas density, a 2–1/1–0 intensity ratio of 0.8 as found by Garcia-Burillo et al. (1993b) is assumed. For the CO-to- H_2 conversion factor X , we assume a quarter of the the Milky Way value X_{MW} (Strong et al. 1988; Strong & Mattox 1996) and constant with radius (Garcia-Burillo et al. 1993b; Guélin et al. 1995). The total H_2 column density per beam in M51 is thus: $N(\text{H}_2) = 0.25 X_{\text{MW}} (1/0.8) \int T_{\text{mb}}(\text{CO}(2-1)) dv$ with

$$X_{\text{MW}} = 2.3 \cdot 10^{20} \text{ cm}^{-2} (\text{K km s}^{-1})^{-1}.$$

Garcia-Burillo et al. (1993b) used ^{12}CO 1–0 to ^{12}CO 3–2 data and Monte Carlo radiative transfer simulations as well as $^{12}\text{CO}/^{13}\text{CO}$ ratios and a comparison with the extinction in 39 HII regions to estimate the X-factor and found it constant with galactocentric radius. Guélin et al. (1995) independently derived the CO-to- H_2 conversion factor, using dust continuum data. Similar X-factors for M51 were found by Kuno et al. (1995b), using CO data and visual extinctions towards HII regions, and by Adler et al. (1992) using BIMA CO 1–0 data assuming that the *giant molecular clouds* (GMCs) are in virial equilibrium.

The X-factor may be a function of the metallicity in spiral galaxies as has been suggested by several authors (e.g. Arimoto et al. 1996). However, other factors like the radiation field or the cosmic-ray rate also have a strong impact on the CO-to- H_2 conversion factor (Bell et al. 2006). The metallicities of M51 have been found to be slightly super solar showing only a shallow drop with radius by only $-0.02 \text{ dex kpc}^{-1}$ (Bresolin et al. 2004): $12 + \log(\text{O}/\text{H}) = 8.72(\pm 0.09) - 0.28(\pm 0.14)R/R_0$ with $R_0 = 5.4'$. The almost constant metallicity appears to be consistent with a constant X-factor.

The 3σ limit ^{12}CO 2–1 data with resolutions of $11''$ and 5 km s^{-1} corresponds to a mass of $1.7 \cdot 10^5 M_\odot$. The spatial resolution of 450 pc does not allow to detect individual GMCs if their typical size is $\sim 50 \text{ pc}$. The individual *clumps* delineating the spiral arms like beads on a string (Fig. 3.1) have been labeled *giant molecular associations* (GMAs). These may be bound clusters of GMCs as suggested by Rand & Kulkarni (1990) or random superpositions of molecular clouds and GMCs (Garcia-Burillo et al. 1993a).

The total mass of the molecular gas of M51 derived from the CO 2–1 data set is $1.94 \cdot 10^9 M_\odot$. This value agrees well with the total mass of $1.6 \cdot 10^9 M_\odot$ derived by Helfer et al. (2003) from NRAO 12m CO 1–0 data when using the same CO-to- H_2 conversion factor and distance.

3.3.3 ^{13}CO 2–1

In Fig. 3.3 the observed spectra of ^{13}CO 2–1 in the north-eastern spiral arm region are shown. Emission is detected in the velocity range of 350-500 kms^{-1} . The temperature is on the T_A^* -scale ranging from -0.01 to 0.05 K. The noise increases at both edges along the scan direction due to undersampling in these regions. The integrated intensity is presented in Fig. 3.4. The ^{13}CO 2–1 integrated intensity distribution was created using the masked moment technique as described above using a threshold of 2σ with a noise level of $\sigma = 0.36 \text{ Kkms}^{-1}$.

Both regions of strong ^{12}CO 2–1 emission also show emission in ^{13}CO 2–1. The maximum intensity in both regions is shifted outwards from the center of the galaxy by approximately $20''$. The southern region shows two peaks of ^{13}CO emission on the inner spiral segment at $90''/60''$ and $80''/100''$. At the northern clump the ^{13}CO emission is shifted but also slightly more extended compared to the ^{12}CO emission. The ratio of the maximum intensity in ^{13}CO and ^{12}CO is at around 13. The average ratio found was 15 in a sample of 8 galaxies studied by the UMass/INAOE Galaxy Survey.

The northern spiral arm region was chosen for observations due to its very prominent ^{12}CO 2–1 emission (Fig. 3.1) and strong ^{13}CO 2–1 intensity at one position (Garcia-Burillo et al. 1993b). In this region Kramer et al. (2005) detected [C I] at one position and Nikola et al. (2001) observed strong [C II] emission.

This thesis presents the spatial distribution of the ^{13}CO 2–1 emission in the northern spiral arm region in M51. In future investigations, it will be interesting to use the optically thin ^{13}CO 2–1 as a tracer for the column density and subsequently the molecular mass. This will enable to locally check the CO-to- H_2 conversion factor X in this region. Possibly future high-resolution interferometer observations with the PdB-IRAM interferometer at $2''$ - $3''$ angular resolution in ^{13}CO 2–1 will allow to study the masses of single giant molecular clouds.

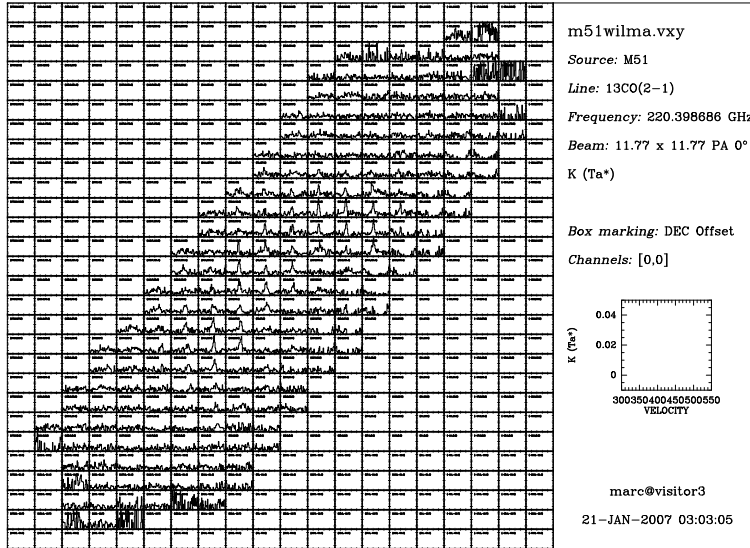


Figure 3.3: Map of ^{13}CO 2–1 spectra in the northern spiral arm region of M51. The spectra are on T_A^* -scale from -0.01 to 0.05 K and the velocity range covers 300 - 550 km s^{-1} .

3.3.4 H I and radio continuum

The H I emission at $6''$ resolution (Fig. 3.5) is weaker in the inner region while the outer CO arms are clearly delineated in H I and show up prominently. There is also prominent patchy H I emission in the south where CO is not detected.

In the inner arms of M51, inside the corotation radius of ~ 7.4 kpc (Garcia-Burillo et al. 1993a), H I and $\text{H}\alpha$ emission (Rand & Kulkarni 1990; Tilanus & Allen 1991; Scoville et al. 2001) as well as young star cluster complexes (Bastian et al. 2005) are seen slightly towards the convex side, i.e. downstream relative to the CO emission, suggesting that they arise when GMCs are destroyed by short-lived OB stars. In a later section, physical mechanisms governing the fraction of atomic to molecular gas are discussed.

Fig. 3.5 shows that the H I clouds tracing the south-western spiral arm, peak on the concave side of the CO arm. This is outside the corotation radius and thus again downstream, consistent with the above interpretation.

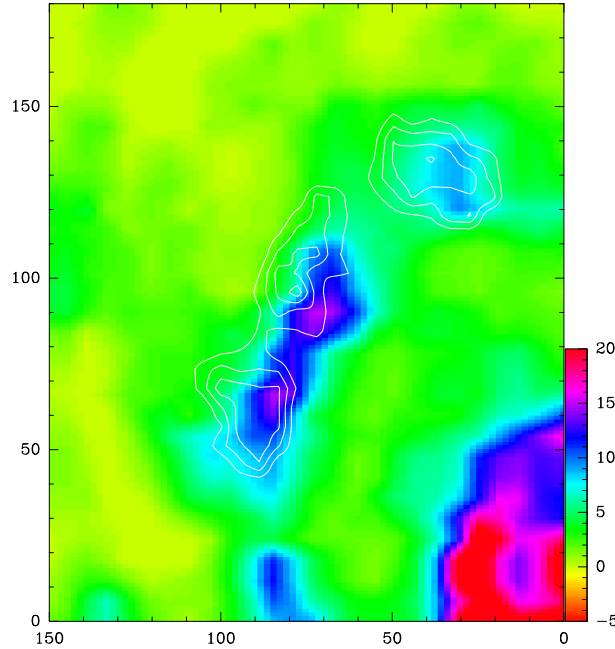


Figure 3.4: Map of ^{12}CO 2–1 integrated intensities and ^{13}CO 2–1 in contours on top. The map shows the entire north-eastern spiral arm region where we detected ^{13}CO 2–1 in M51. Contours range in units of 0.5σ from 0.18 to 1.20 Kkms^{-1} . The underlying ^{12}CO 2–1 integrated intensity is given in units of Kkms^{-1} .

Fig. 3.6 shows a map of the radio continuum (RC) at 20 cm (1.4 GHz) taken with the VLA at $15''$ resolution (Patrikeev et al. 2006). Further below, we will use this map to derive the star formation rate per unit area. The radio continuum map shows strong emission in the inner arms, which slowly drops off towards the outer arms. There is patchy 20 cm emission in the south where there is HI but only very little CO. Again similar to HI, the 20 cm emission tracing the south-western spiral arm peaks on the concave, downstream side of the CO arm. The spiral arm near $(-40'', 125'')$ shows an interesting discontinuity and local lack of radio continuum, HI, and CO emission. Patrikeev et al. (2006) discuss systematic offsets between the spiral arms traced by 6 cm radio continuum emission, ISOCAM data at $15\ \mu\text{m}$, and BIMA CO 1–0 emission over scales of several kpc.

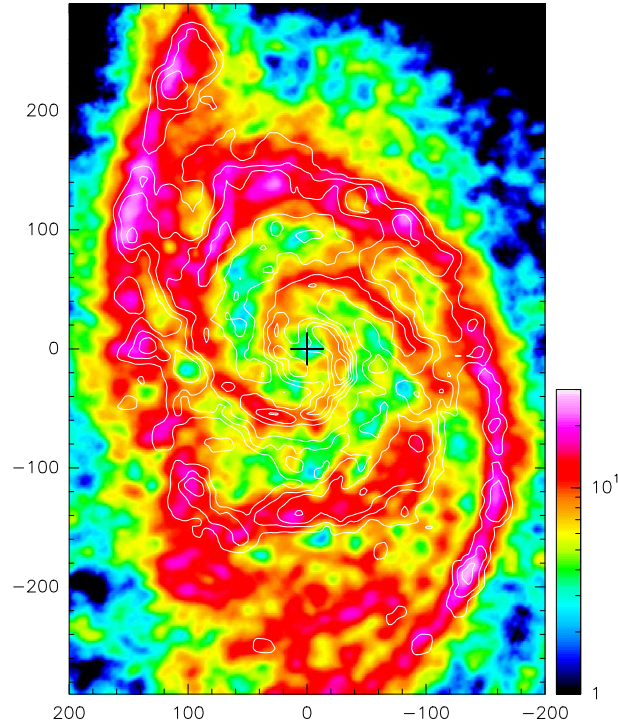


Figure 3.5: VLA map of the H I column density [$1\text{E}20 \text{ cm}^{-2}$] at $6''$ resolution in colors. Contours show integrated ^{12}CO 2–1 intensities (cf. Fig. 3.1).

3.3.5 Dust emission

The $850\mu\text{m}$ emission in M51 shown in Fig. 3.7 is broader and smeared out compared to the ^{12}CO 2–1 emission, which delineates spiral arms more prominently. The spiral arm regions in the central part are visible. In the outer parts, the spiral arms prominently visible in CO are not detected in dust emission. Meijerink et al. (2005) decomposed the dust emission in an extended underlying exponential disk and spiral structure superimposed. In the analysis parts, we will compare this composition with the structure of the total gas surface density in M51. Note that especially in the spiral arms the dust emission may be significantly contaminated by ^{12}CO 3–2 emission up to 30–40 % (Meijerink et al. 2005).

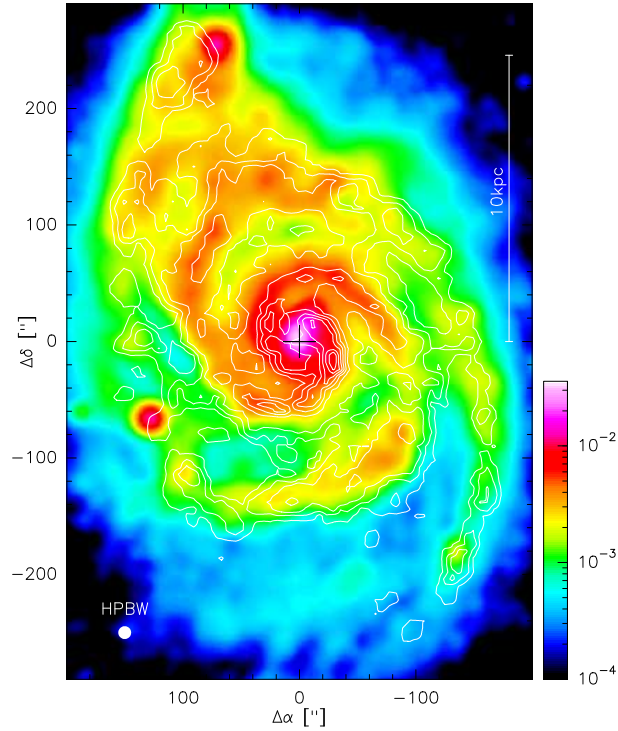


Figure 3.6: Map of radio continuum intensities at 20 cm (VLA C+D, 15'' resolution) in units of Jy/beam (Patrikeev et al. 2006). Contours show integrated ^{12}CO 2–1 intensities (cf. Fig. 3.1).

3.4 Molecular and atomic gas

3.4.1 The total gas surface density

In Fig. 3.8 we present a map of the total gas surface density Σ_{gas} . This map is a major ingredient of the gravitational stability analysis which is discussed later. It combines the the local distribution of the molecular and atomic components in the disk of M51.

To convert from the observed integrated intensities to the total gas surface density, we use the relation $\Sigma_{\text{gas}} = 1.36 \times (\Sigma_{\text{H}_2} + \Sigma_{\text{H}_I})$ taking into account the mass contribution from He. The atomic surface density was calculated

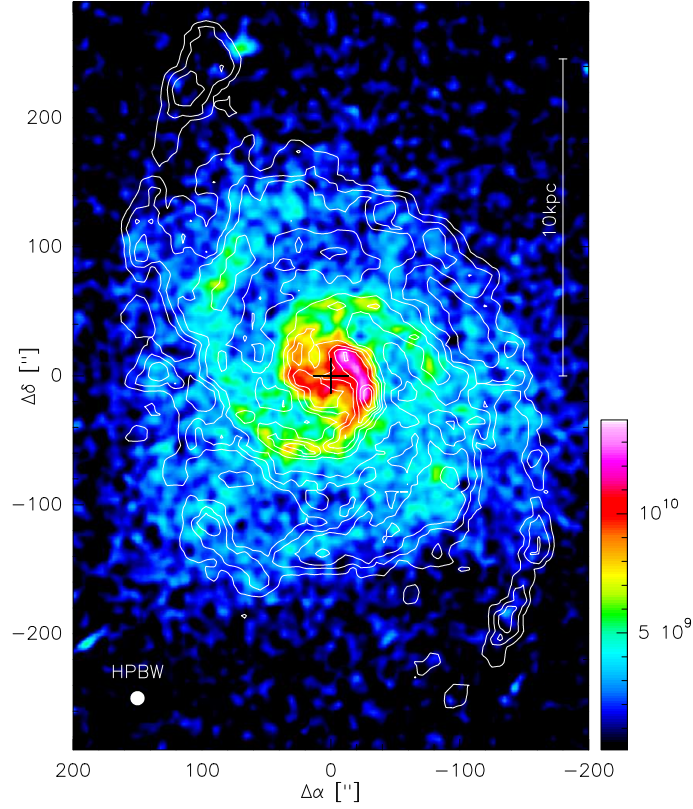


Figure 3.7: Map of $850\mu\text{m}$ dust emission observed with SCUBA (in raw instrumental units) at the JCMT (Meijerink et al. 2005). ^{12}CO 2–1 in contours and HPBW indicated.

from the THINGS H I column density image of M51 smoothed to $11''$ resolution. Two logarithmic spirals (shown in black) serve as a guide to delineate the inner spiral arms. They are adopted from Shetty et al. (2007) who determined them based on $^{12}\text{CO}1-0$ data. As this is the first total gas density map of M51, we briefly summarize some prominent morphology of the map next. There are several spur-like structures bridging the gap between the inner spiral structure and the outer spiral arms e.g. in the north-western area at $(-40'', 80'')$ at a surface density of $20\text{--}30 M_{\odot} \text{pc}^{-2}$. Also, in the north-east at $(100'', 100'')$ there is a strong bridge between inner and outer spiral arms with a total gas surface density of $20\text{--}40 M_{\odot} \text{pc}^{-2}$. The gaps or minima in total gas density seen in the spiral arms e.g. at $(-80'', -40'')$ and at $(-120'', 60'')$ are interpreted as the signature of 4:1

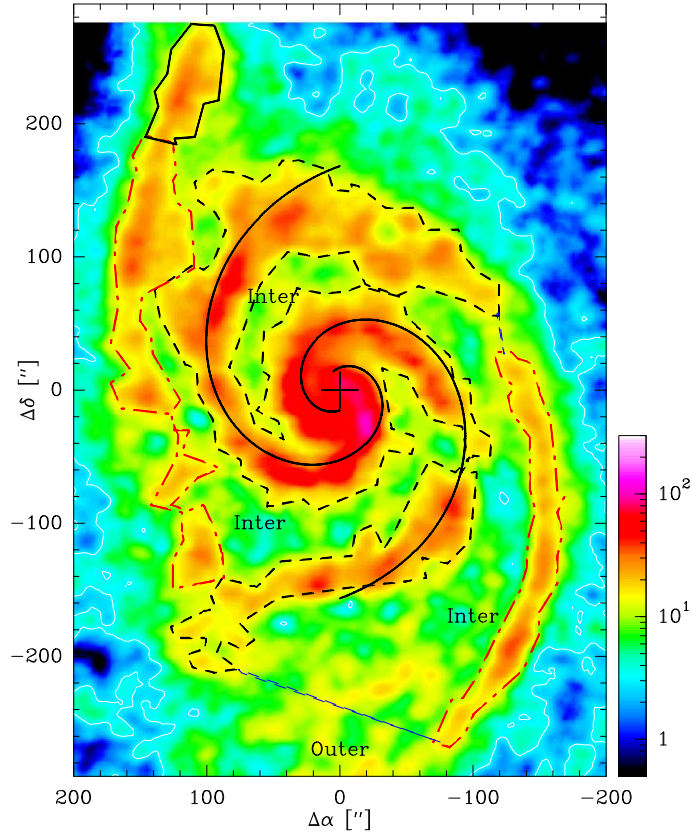


Figure 3.8: Map of the total gas mass surface density Σ_{gas} in M51 in $M_{\odot} \text{pc}^{-2}$ derived from the $^{12}\text{CO}2-1$ and H I-emission. The $1-\sigma$ value of the total gas density map is $0.8 M_{\odot} \text{pc}^{-2}$. A logarithmic spiral is shown in all Figures of M51 to guide the eye. Contours mark regions discussed in §3.4.1 and Table 3.2.

ultra harmonic resonances by Elmegreen et al. (1989), applying density wave theory.

Next, we mask different regions in M51 to characterize their average properties in Table 3.2. We identify spiral arm regions in the total gas density map using a threshold surface density of $20 M_{\odot} \text{pc}^{-2}$. This discerns spiral arm and interarm regions in the central part similar to visual inspection of the total gas density map. This threshold also roughly reproduces the

shape of the spiral arms in H α -emission (Scoville et al. 2001), 20cm radio-continuum emission (Patrikeev et al. 2006) and CO 1–0 interferometer data (Shetty et al. 2007). The inner spiral arms and the companion are marked in black short-dashed contours. The outer spiral arm regions are indicated in red contours. The closed non-spiral arm regions labeled *Inter* in Fig. 3.8 are averaged for the interarm regions properties. The disk outside the previous regions and above the 3σ level of $2.4 M_{\odot} \text{pc}^{-2}$ ($\sigma(\Sigma_{\text{H}_2}) = 0.36 \text{Kkms}^{-1}$, $\sigma(\Sigma_{\text{H I}}) = 0.44 \text{Kkms}^{-1}$), indicated by the white contour, we label as the outer disk.

Σ_{gas} in the spiral arm regions The total gas surface density in Fig. 3.8 peaks at $127 M_{\odot} \text{pc}^{-2}$. The inner spirals with the most dense region just south-west of the center show peak total gas surface densities of 80-100 $M_{\odot} \text{pc}^{-2}$. Averaging over the indicated inner spiral arm region covering the eastern and western arms, we obtain $\Sigma_{\text{gas}} \sim 26.8 M_{\odot} \text{pc}^{-2}$ (Table 3.2). The western inner arm shows a significant gap near $(-80'', -80'')$ leading to the lower average density.

The outer spiral arms show less gas surface density compared to the inner spiral arms with an averaged total gas density of $18.8 M_{\odot} \text{pc}^{-2}$ including the south western spiral arm and the north eastern spiral arm. This is approximately a factor of 1.5 weaker than the spiral arms in the central region. Few high density regions on the outer spiral arms reach Σ_{gas} of 40-50 $M_{\odot} \text{pc}^{-2}$ e.g. to the south-west at $(-120'', -200'')$ and the north-east at $(140'', 100'')$. This is significantly weaker compared to the peaks in the center.

Σ_{gas} in the interarm regions The interarm regions show surface densities of 5-15 $M_{\odot} \text{pc}^{-2}$. The average value is $9.4 M_{\odot} \text{pc}^{-2}$. The averaged inner arm/interarm contrast in the total gas surface density is 2.9 confirming the results of Garcia-Burillo et al. (1993b) in the integrated CO 2–1 intensities. Table 3.2 summarizes these results.

Table 3.2: Properties of Σ_{gas} and $\Sigma_{\text{H}_2}/\Sigma_{\text{HI}}$ in M51 averaged over the areas shown in Fig. 3.8.

	Σ_{gas} [$M_{\odot} \text{ pc}^{-2}$]	$\Sigma_{\text{H}_2}/\Sigma_{\text{HI}}$
inner spiral arms	26.8	2.3
outer spiral arms	18.8	0.21
interarm region	9.4	0.71
outer disk	6.4	-
NGC5195 - companion	20.2	0.4
ratio inner/outer spiral	1.4	11.0
inner arm/interarm	2.9	3.2
outer arm/interarm	2.0	0.3

Error-beam pick up Note that the arm/interarm contrast in the ^{12}CO 2–1 map is a lower limit as error beam contribution affects the integrated intensities. In interarm regions the pick-up of arm regions will tend to increase the intensity while in arm regions the situation is reversed. The IRAM-30m telescope has 3 error beam contributions with beam widths of $125''$, $180''$ and $950''$ at 230 GHz with relative power contributions of 10-20%, 12% and 26% for a beam efficiency of $B_{\text{eff}} = 0.42$ (Greve et al. 1998). As the B_{eff} increased to $B_{\text{eff}} = 0.52$ the relative power contributions of the error beams will be lower to date.

3.4.2 Total gas densities in other galaxies

We will compare the total gas density map of M51 to the nearby galaxies M83 and LMC, as they belong to the few galaxies where high resolution total gas density maps are published. In the future the combined analysis of complete HI and CO maps of a large sample of galaxies will allow to infer possible correlations of gas density and distribution with galaxy type or the global environment of a galaxy, e.g. the interaction with a neighbor galaxy.

M83: First, we compare the Σ_{gas} distribution of M83 (Lundgren et al. 2004) with our results in M51. M83 is a nearly face-on galaxy with a similar inclination of 24° compared to M51, showing a pronounced spiral structure. M83 is at a distance of 4.5 Mpc and the total gas density map in Lundgren et al. (2004) has an angular resolution of $22''$ (i.e. 480 pc) similar to the physical resolution of the M51 data. The map is created using ^{12}CO 1–0 observations assuming a constant X-factor and additionally HI-data for the atomic component. M83 has in general a significantly higher mass density compared to M51 reaching $\Sigma_{\text{gas}} = 500 \text{ M}_\odot \text{ pc}^{-2}$ in the center and $100\text{--}200 \text{ M}_\odot \text{ pc}^{-2}$ in the inner spiral arms. The interarm regions show total gas surface densities of $10\text{--}20 \text{ M}_\odot \text{ pc}^{-2}$. This is still roughly a factor of 5 higher than the value derived in M51. The arm/interarm contrast is stronger than in M51.

Sakamoto et al. (1999) studied the influences of bar driven molecular gas transport into the inner part of galaxies. As M83 inhibits a strong central bar, the higher gas densities compared to M51 might be the result of enhanced gas accretion by the bar. Spurs and bridges connecting spiral arm regions are also found in M83, especially in the inner $100''$.

LMC: Yang et al. (2007) present a total gas surface density map of the LMC, an irregular SB dwarf of the Milky Way with an inclination angle of 35° at only 50 kpc distance. Yang et al. (2007) used ^{12}CO 1–0 (Fukui et al. 2001) and HI -data (Kim et al. 2003) to construct a map of the total gas density at a spatial resolution of 40 pc. The Σ_{gas} map of the LMC shows several dense regions with densities up to $100 \text{ M}_\odot \text{ pc}^{-2}$. The linear dimension of these regions varies from around 50 pc to 4 kpc. Their orientation is not organized in spiral arms.

The lowest density areas in the LMC have densities of $\Sigma_{\text{gas}} = 4 \text{ M}_\odot \text{ pc}^{-2}$ (Yang et al. 2007), very similar to the detection limit achieved in M51.

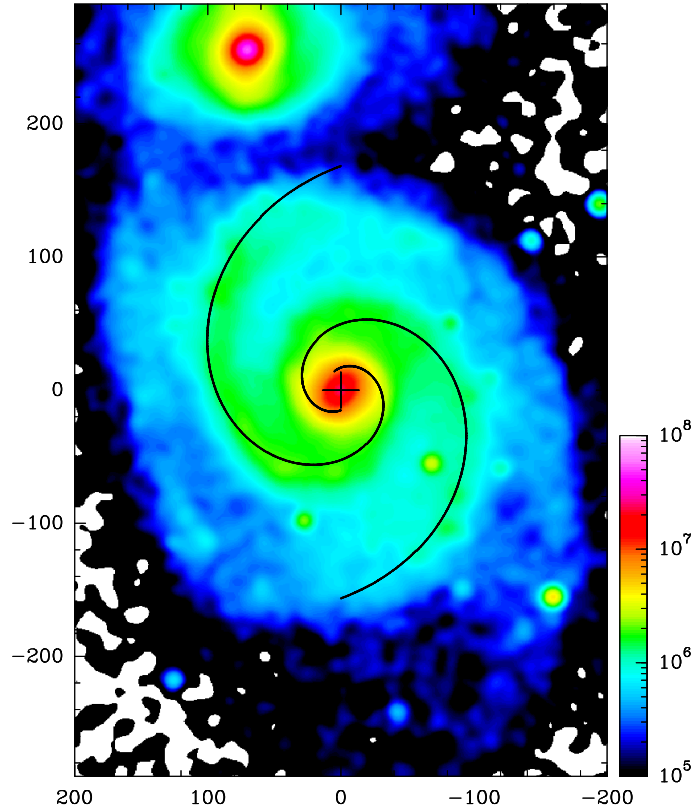


Figure 3.9: Map of the K -band luminosity L_K from the Two Micron All Sky Survey (2MASS) Large Galaxy Atlas (Jarrett et al. 2003) smoothed to $11''$ resolution. The units are L_\odot .

3.5 Stellar surface density from the K -Band emission

The stellar surface density is an important parameter in determining the stability of the disk. We use the K -Band images of the 2MASS Large Galaxy Atlas (Jarrett et al. 2003) to determine the stellar surface mass density Σ_* . The K -Band is a reasonable tracer of the stellar mass density as it is much less affected by extinction within M51 than e.g. the B -Band in the optical. The Galactic foreground extinction in the K -Band is 0.013 mag compared to 0.152 mag in the B -Band (Schlegel et al. 1998).

Bell & de Jong (2001) discuss mass-to-light ratios in the optical and near-IR passbands. Assuming an universal spiral galaxy initial mass function (IMF), they find variations of the mass-to-light ratio of up to 7 in the optical, 3 in the B -Band and 2 in the K -Band. To convert from luminosities to solar masses, we use a K -Band mass-to-light ratio $M_K/L_K = 0.5 M_\odot/L_\odot$ (Bell & de Jong 2001). The stellar surface density is then determined from the K -Band luminosities via $\Sigma_* = 4.27 \cdot 10^{-5} \times L_K M_\odot \text{pc}^{-2}$ for a distance of 8.4 Mpc to M51 and an angular resolution of $3''$.

3.6 Radial averages and Schmidt law

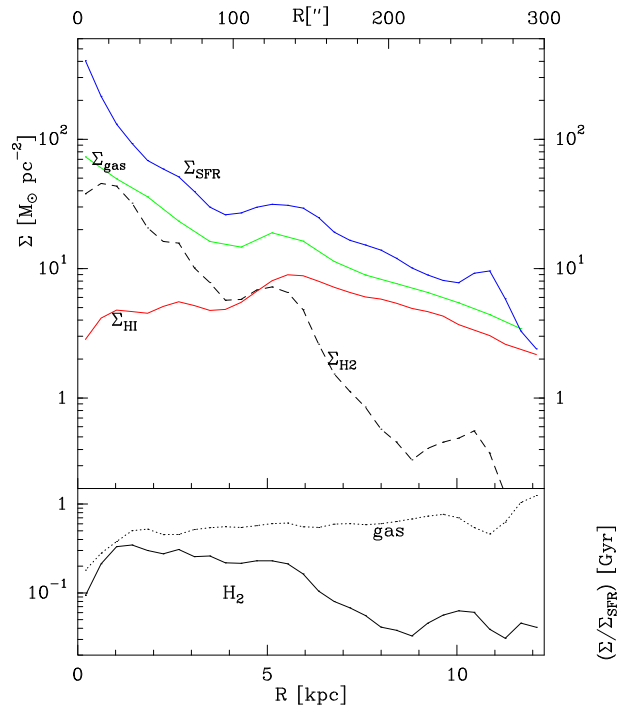


Figure 3.10: Radial distributions of surface densities of H_2 , HI, the total gas, and the star formation rate per unit area in M51. The lower box shows the ratios $\Sigma_{\text{gas}}/\dot{\Sigma}_{\text{SFR}}$ and $\Sigma_{H_2}/\dot{\Sigma}_{\text{SFR}}$.

Next, the correlation of H_2 and HI surface densities in radial averages and the local distribution is studied. We also investigate the local Schmidt law

for M51 using estimations of the star forming activity along radial averages, including the outskirts of the disk where H I dominates.

3.6.1 Radial distribution of the gas

Total H₂ column densities are derived from the integrated CO 2–1 intensities as described in Sec. 3.3.2. We derive the face-on surface density via $\Sigma_{\text{H}_2} = 2 m_{\text{H}} N(\text{H}_2) \cos i$ with the atomic hydrogen mass m_{H} and the inclination angle i of M51 (Table 3.1). The total H I column density is derived assuming optically thin emission: $N(\text{HI}) = 1.82 \cdot 10^{18} \int T_{\text{mb}} dv / (\text{K km s}^{-1}) \text{ cm}^{-2}$. The corresponding surface density is: $\Sigma_{\text{HI}} = m_{\text{H}} N(\text{HI}) \cos i$. The total molecular mass of M51 is $1.94 \cdot 10^9 M_{\odot}$ (Sec. 3.3.2) and the global ratio of H I over H₂ mass is 1.36. The molecular gas content of M51 is similar to the total molecular mass of the Milky Way, $1.3 \cdot 10^9 M_{\odot}$ (Misiriotis et al. 2006). However, the Milky Way has a larger fraction of H I mass. The ratio of H I over H₂ mass in the Milky Way is 6.3.

Fig. 3.10 shows the radial profiles of the surface densities.

Radial averages¹⁴ of surface densities in this thesis were created by averaging in azimuth in elliptical annuli spaced by 10'', including points of no detection, and centered at the (0,0) position. The annuli were assumed to be circular rings viewed at an inclination angle $i = 20^\circ$ and with a line of nodes rotated from north to east by the position angle PA=170 °(Table 3.1).

Total gas surface densities are given by $\Sigma_{\text{gas}} = 1.36(\Sigma_{\text{H}_2} + \Sigma_{\text{HI}})$ which includes helium. The radially averaged Σ_{gas} drops by a factor of ~ 20 from $70 M_{\odot} \text{ pc}^{-2}$ in the center to $3 M_{\odot} \text{ pc}^{-2}$ at radii of 12.2 kpc (300'') (Fig. 3.10).

Fig. 3.11 shows the variation of $\Sigma_{\text{HI}}/\Sigma_{\text{H}_2}$ with radius in M51. Standard deviations of the mean Σ_{HI} and Σ_{H_2} are calculated from the rms values along the annular averages: $\sigma = \text{rms}(N_{\text{pix}}/n_{\text{beam}})^{-0.5}$, following Wong & Blitz (2002) with the number of pixels per annulus N_{pix} and the number of pixels per beam n_{beam} . The fraction of atomic gas gradually increases with

¹⁴hereafter we use the term radial averages to define the radial profiles of quantities which are averaged over azimuth as a function of radius in the disk of the galaxy

radius. In the inner regions of M51, up to ~ 6 kpc, the ratio of HI to H₂ surface density scales roughly with $R^{1.5}$. As the radial HI profile in M51 is roughly constant, varying only by a factor of ~ 5 , the powerlaw dependence of the ratio of molecular and atomic gas is largely due to the decrease of the molecular gas surface density which drops by more than 2 orders of magnitude. The HI gas surface density starts to exceed the molecular surface density at radii greater than 4 kpc. The outer regions show deviate from any simple powerlaw. The peak $\Sigma_{\text{HI}}/\Sigma_{\text{H}_2}$ fraction reaches values of 20 in the outer areas of our map.

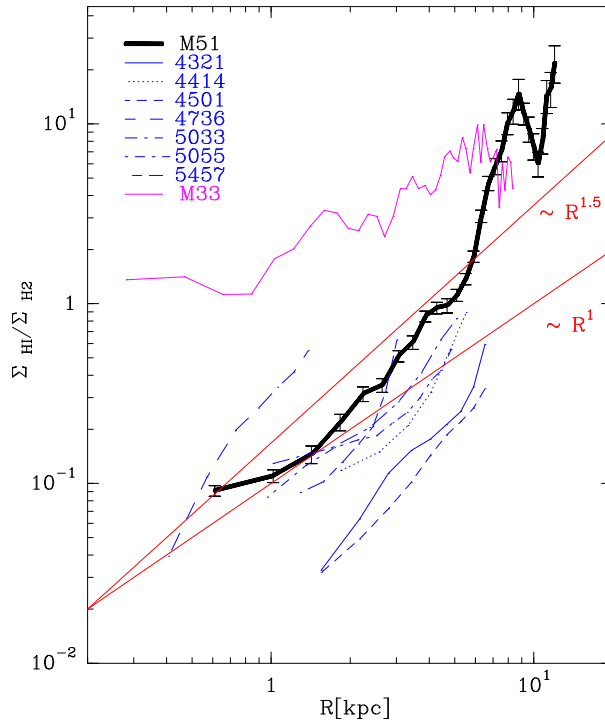


Figure 3.11: Radial distribution of the ratio of atomic Σ_{HI} to molecular surface densities Σ_{H_2} for M51 (thick line), the six spirals of the sample of Wong & Blitz (2002), and M33 (Heyer et al. 2004). For comparison, we show two powerlaws, one where the ratio scales with $R^{1.5}$ and one where it scales with R .

The ratio of atomic and molecular gas surface densities Fig. 3.11 also shows the fraction of atomic gas for the seven spirals studied by Wong

& Blitz (2002) and for M33 studied by Heyer et al. (2004). In the center regions, the $\Sigma_{\text{HI}}/\Sigma_{\text{H}_2}$ ratio of the nine galaxies varies strongly between 0.03 in NGC 4321 and slightly more than 1 in M33. With the exception of M33, the inner regions are clearly dominated by molecular material. For the galaxies of the Wong sample, the ratio scales roughly with $R^{1.5}$ for radii upto ~ 6 kpc. In M33, the atomic gas dominates the total gas surface density for the entire disk, in strong contrast to the other 8 spirals (Fig. 3.11). The slope is much more shallow: the fraction of atomic gas scales with $R^{0.6}$ only (Heyer et al. 2004). At ~ 7 kpc, the fraction equals the fraction found at that distance in M51.

3.6.2 The molecular gas fraction

Fig. 3.12 shows the ratio map of atomic gas surface density Σ_{HI} and molecular gas surface density Σ_{H_2} . Note that this is the inverse ratio compared to radial averages in the previous section. This is intentional as we will compare $\Sigma_{\text{H}_2}/\Sigma_{\text{HI}}$ to the hydrostatic pressure subsequently. In the map areas below $2\sigma=1.3$ Kkms $^{-1}$ of the masked-moment integrated intensity image of ^{12}CO 2–1 were blanked. As the HI is more extended, the Σ_{H_2} limits the extend of the map.

The map of $\Sigma_{\text{H}_2}/\Sigma_{\text{HI}}$ (Fig. 3.12) shows a steep decrease of the ratio from peak values of around 50 in the center to 0.1 in the outer regions (cf. radial averages). The spiral arms in the center are the regions with the highest fraction of molecular gas. The average ratio in the two inner spiral arms delineated in Fig. 3.8 is 2.1. Outwards, at radii of around $100''$, the ratio drops also in the spiral arms. The north-eastern and south-western continuation of the inner spiral arms shows $\Sigma_{\text{H}_2}/\Sigma_{\text{HI}}$ at around 1 and in few regions up to 2-3. There are few regions with a ratio of 1 or slightly above which are correlated with the regions of increased total gas density (Fig. 3.8). The average ratio on the outer spiral arms in the marked polygons is 0.21. This is a factor of 10 lower compared to the inner spirals. The interarm region shows an average ratio of 0.71.

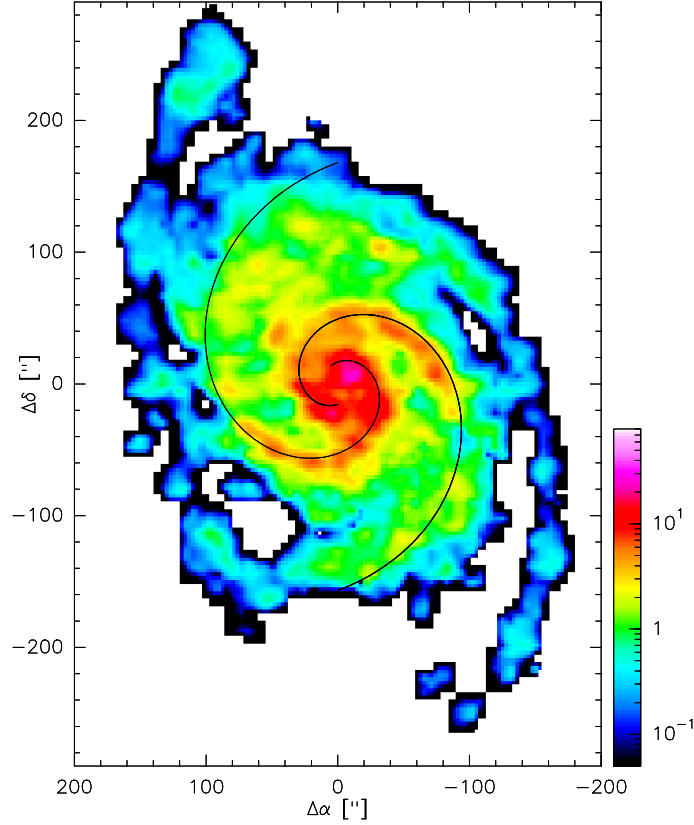


Figure 3.12: Map of the ratio of molecular- (Σ_{H_2}) and atomic gas surface density ($\Sigma_{\text{H I}}$) in M51 derived from the ^{12}CO 2-1 and H I-emission. Regions without detection of ^{12}CO 2-1 are blanked. The $1\text{-}\sigma$ limit in the ^{12}CO 2-1 data is 0.65Kkm s^{-1} corresponding to $\Sigma_{\text{H}_2} = 0.36 M_{\odot} \text{pc}^{-2}$.

The dominant trend in the $\Sigma_{\text{H}_2}/\Sigma_{\text{H I}}$ -ratio is the decrease with galactocentric radius by at least one order of magnitude. Additionally, the $\Sigma_{\text{H}_2}/\Sigma_{\text{H I}}$ -ratio varies between spiral arm and interarm regions. This weaker effect, possibly induced by the spiral density wave, locally influences the ratio. This enhances the molecular fraction in the inner parts further and weakens the decrease of the molecular fraction in the outer spiral arms.

The hydrostatic pressure in the disk of M51 has been recently identified as an important parameter governing the ratio of atomic and molecular gas e.g. by Blitz & Rosolowsky (2004a). The next subsection will address the

hydrostatic pressure in M51 and its correlation with the ratio of atomic and molecular surface density.

3.6.3 The hydrostatic pressure

Recent investigations, e.g. by Blitz & Rosolowsky (2004a,b, 2006), have shown a tight correlation of the ratio of molecular Σ_{H_2} and atomic gas densities $\Sigma_{\text{H I}}$ in external galaxies and the hydrostatic pressure P_{hydro} . Elmegreen (1993) theoretically studied the impact of hydrostatic pressure and radiation field on the ratio of atomic and molecular gas. He concludes that the pressure should be the dominant factor and predicts a powerlaw $\frac{\Sigma_{\text{H}_2}}{\Sigma_{\text{H I}}} \sim P_{\text{hydro}}^{2.2}$.

Following Blitz & Rosolowsky (2004b), the hydrostatic pressure can be estimated for an infinite disk with isothermal gas and stellar layers from the midplane pressure in equilibrium:

$$P_{\text{hydro}} = (2G)^{0.5} \Sigma_{\text{gas}} \sigma_{\text{gas}} (\rho_*^{0.5} + (\frac{\pi}{4} \rho_{\text{gas}})^{0.5}). \quad (3.2)$$

Assuming the volume density of the gas ρ_{gas} is small compared to the stellar density ρ_* and a self-gravitating stellar disk ($\Sigma_* = 2\rho_* h_*$):

$$P_{\text{hydro}} = 0.84(G\Sigma_*)^{0.5} \Sigma_{\text{gas}} \frac{\sigma_{\text{gas}}}{h_*^{0.5}}. \quad (3.3)$$

Σ_* is the stellar surface density which we will address in a later section, Σ_{gas} the total gas density and σ_{gas} the velocity dispersion of the gas. We estimated σ_{gas} from the ^{12}CO 2–1 velocity dispersion as we will discuss in the next section. For the stellar scale height we adopt $h_* = 1$ kpc consistent with studies by van der Kruit & Searle (1981); Kregel et al. (2002). They find in their surveys of edge-on spiral galaxies a variation of h_* from 0.4–1.7 kpc with no dependence on the galactocentric radius. For all input quantities in SI-units, P_{hydro} in equation 3.3 is given in N/m^2 . In more convenient units with surface densities in $\text{M}_{\odot} \text{pc}^{-2}$, the gas dispersion in kms^{-1} and the stellar scale height in pc, the equation takes the form:

$$P_{\text{hydro}}/k_{\text{B}} = 272 \text{ cm}^{-3} \text{K} (\Sigma_*)^{0.5} \Sigma_{\text{gas}} \frac{\sigma_{\text{gas}}}{(h_*)^{0.5}}. \quad (3.4)$$

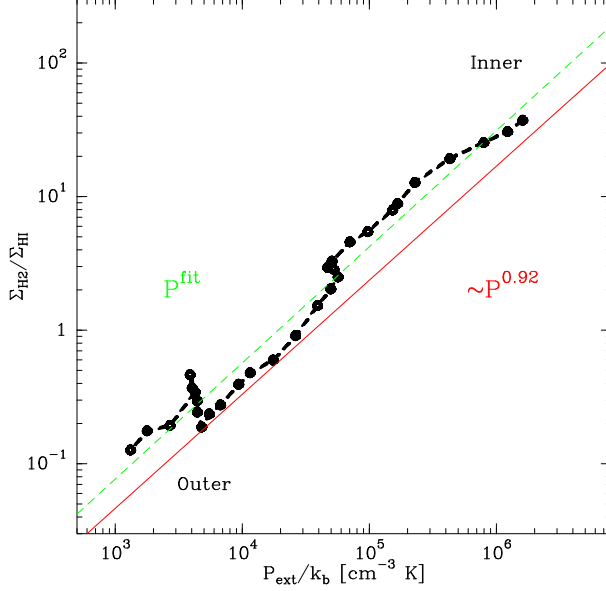


Figure 3.13: The fraction of molecular gas density Σ_{H_2} and atomic gas density Σ_{H_I} is plotted against the hydrostatic pressure P_{hydro} . The slope found in Blitz & Rosolowsky (2006) is indicated in red. In green the fit to our data P^{fit} is shown. Galactocentric radius in decreasing from left to right.

Fig. 3.13 shows the ratio of molecular gas density Σ_{H_2} and atomic gas density Σ_{H_I} plotted against the hydrodynamic pressure P_{hydro} . A linear regression fit yields a powerlaw:

$$\frac{\Sigma_{\text{H}_2}}{\Sigma_{\text{H}_I}} = (P_{\text{hydro}}/P_0)^\alpha, \quad (3.5)$$

with the powerlaw coefficient $\alpha = 0.87 \pm 0.03$ and $P_0 = (1.92 \pm 0.07) 10^4 \text{ cm}^{-3}\text{K}$. The slope of 0.87 is very similar to the slope of 0.92 determined by Blitz & Rosolowsky (2006) for a sample of 14 spiral and dwarf galaxies, including M51. We find a slightly lower P_0 compared to the mean result of Blitz & Rosolowsky (2006) in their sample with $(3.5 \pm 0.6) 10^4 \text{ cm}^{-3}\text{K}$.

The stellar surface density Σ_* at $\Sigma_{\text{H}_2}/\Sigma_{\text{H}_I}=1$ is at around $50 \text{ M}_\odot \text{ pc}^{-2}$. Blitz & Rosolowsky (2006) found in most of their galaxies a higher value of around $120 \text{ M}_\odot \text{ pc}^{-2}$ using an Galactic X-factor.

The importance of hydrostatic pressure This result underlines the importance of the hydrostatic pressure as the physical parameter determining the fraction of molecular to atomic material at a given radius on large scales. The nearly linear dependence found over the whole pressure regime is expected by theoretical predictions (Blitz & Rosolowsky 2006; Elmegreen 1993), if the gravitational potential imposed by the gaseous component is small compared to the stellar component. Note, that the pressure dependence of the molecular to atomic fraction is expected to break down when the spatial resolution of the observational data is of the order of the size of a single GMC. A single GMC is expected to have enhanced pressure due to self-gravity and the assumption of pressure equilibrium is no longer valid (Blitz & Rosolowsky 2006).

The next chapter deals with the Schmidt law, i.e. the correlation of the total gas surface densities with the star formation rate derived from the 20 cm radio continuum data, for M51. We introduced the Kennicutt-Schmidt law in section 2.4.

3.6.4 Star formation rate and local Schmidt law

Star formation rate from the radio continuum emission Various tracers of star formation such as $H\alpha$, UV, the far infrared continuum, and the radio continuum are frequently used. $H\alpha$ emission is directly linked to OB associations but subject to extinction. See Bastian et al. (2005) for a recent study of the local star formation rate in M51, derived from $H\alpha$ images. Optically thin far-infrared (FIR) emission is usually taken as the most direct indicator of star formation. In a recent study, Calzetti et al. (2005) used MIPS/Spitzer $24\mu\text{m}$ maps to study the star formation rate. Some questions remain however in regions of diffuse FIR emission from the atomic ISM. In such regions the dominant contribution to the FIR flux may be due to radiation heating of dust by the normal interstellar radiation field (Cox & Mezger 1989) and thus not trace star formation.

Radio continuum as a tracer of the star formation rate The radio continuum has widely been accepted as an alternative measure for star

formation activity, a fact which is underlined by the very strong FIR/RC correlation in many different galaxies (see the review by Condon 1992). The FIR/RC correlation holds also on local scales of a few hundred parsecs comparable to the resolution of our data set. See Murphy et al. (2005) who recently studied this relation in M51. The large scale 20 cm map of Patrikeev et al. (2006) at $15''$ resolution is shown in Fig. 3.6 and we assume that the 20 cm radiation can be used as a direct indicator for the star formation rate. The FIR/RC correlation and a subsequent SFR/FIR conversion is used to derive the star formation rate. We then compare the star formation rate with the H_2 and HI surface densities in order to check for star formation thresholds.

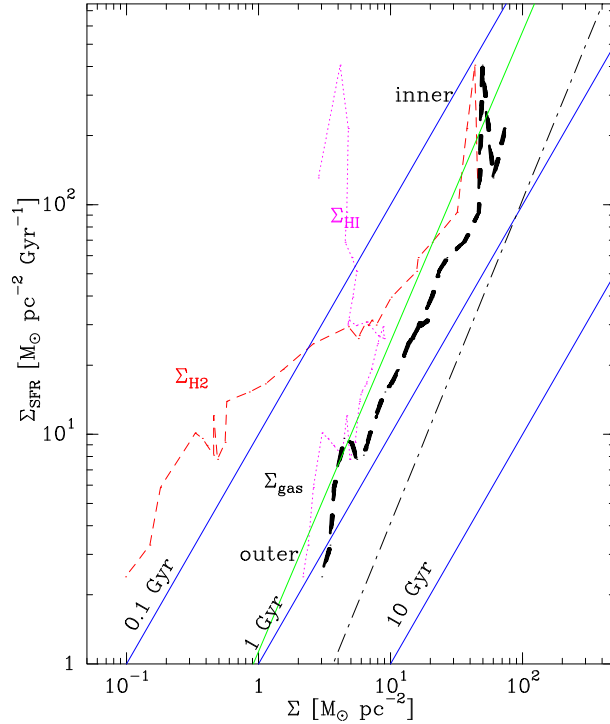


Figure 3.14: Radially averaged star formation rate per unit area, $\dot{\Sigma}_{\text{SFR}}$, versus surface density of H I, H_2 , and the total gas Σ_{gas} . The solid green line is the local Schmidt law found in M51. The dashed-dotted black line is the global Schmidt law found by Kennicutt (1998). Drawn blue lines represent lines of constant gas depletion time or star formation efficiency.

The radio continuum emission of the disk of M51 reflects the spatial distri-

bution of the current star formation rate. In normal galaxies, such as M51, most of the radio continuum at 20 cm is non-thermal synchrotron emission (Condon 1992), radiated by cosmic rays interacting with the magnetic fields of the interstellar medium. The cosmic rays in turn are emitted by supernova remnants. The remaining radio continuum emission is free-free bremsstrahlung emission from thermal electrons in H II-regions. The radio continuum thus traces the current star formation rate of massive stars.

The observed optically thin radio continuum emission is known to be well correlated with FIR dust continuum emission in a large variety of sources, including normal disk galaxies. The tight correlation was confirmed by Helou et al. (1985) using IRAS data and is described by the parameter

$$q = \log\left(\frac{\text{FIR}}{[3.75 \cdot 10^{12} \text{ Wm}^{-2}]}\right) - \log\left(\frac{S_{20\text{cm}}}{[\text{Jy}]}\right). \quad (3.6)$$

The parameter q was found to be 2.3 with a dispersion of ~ 0.2 dex in a wide variety of sources (Condon 1992). We used this relation to derive the FIR flux at $15''$ resolution at each position in M51. Murphy et al. (2005) have recently confirmed that this correlation holds for a map of M51 at $70 \mu\text{m}$ using MIPS/Spitzer at $19''$ resolution. In the disk, they find a median and scatter of $q_{70} = 1.94 \pm 0.19$. Note that the correlation is expected to break down at yet smaller scales of a few hundred parsecs around massive star-forming regions (Boulanger & Perault 1988).

The FIR intensity reflects the current star formation rate (see e.g. Yun et al. 2001), as young stars form deeply embedded in their parental molecular clouds, before dispersing their environment by forming H II regions and by supernovae explosions. Following the argument of Thronson & Telesco (1986), the FIR luminosity is proportional to the star formation rate:

$$L_{\text{FIR}} = \text{SFR } t_{\text{FIR}} L/M, \quad (3.7)$$

where L/M is the luminosity-to-mass ratio of the young stellar clusters. Assuming a typical disruption time-scale of $t_{\text{FIR}} = 2 \cdot 10^6$ yr and a

Salpeter initial mass function (IMF), the current star formation rate is $\text{SFR} = 6.5 \cdot 10^{-10} (L_{\text{FIR}}/L_{\odot}) M_{\odot} \text{yr}^{-1}$. In summary, the star formation rate per unit area is related to the flux density at 20 cm via

$$\frac{\dot{\Sigma}_{\text{SFR}}}{[M_{\odot} \text{pc}^{-2} \text{Gyr}^{-1}]} = 1.53 \cdot 10^5 \frac{S_{20\text{cm}}}{[\text{Jy beam}^{-1}]} \quad (3.8)$$

The gas depletion or consumption time is defined as $\tau_{\text{gas}} = \Sigma_{\text{gas}}/\dot{\Sigma}_{\text{SFR}}$. This is the time which would be needed to convert the total gas content into stars assuming that the SFR is constant with time and that there is no gas infall or recycling via stellar winds. Note, that the inverse of the gas depletion time is the star formation efficiency. Next, we compare the global star formation rate of M51 with previous extragalactic studies.

The global star formation rate The global star formation rate of M51 is $2.56 M_{\odot} \text{yr}^{-1}$ and the global gas depletion time 0.76 Gyr. The latter value corresponds to a global star formation efficiency (SFE) of 13% per 0.1 Gyr. Both values, the depletion time and the SFE, agree to within a factor of 2 with the values derived by Scoville et al. (2001) from Hubble Space Telescope (HST) $\text{H}\alpha$ images and CO data. Misiriotis et al. (2006) have recently studied the distribution of the ISM in the Milky Way. They find a similar SFR of $2.7 M_{\odot} \text{yr}^{-1}$ but factor ~ 5 larger gas depletion time of 3.57 Gyr in the Milky Way. Typical normal spiral galaxies need less time than found in the Milky Way, but more time than found in M51, to consume all the gas into stars. Kennicutt (1998) finds a median depletion time of 2.1 Gyr for his sample of 61 normal disk galaxies which shows variations between 0.2 Gyr in starburst galaxies like NGC 5169 and 12 Gyr in early-type spirals such as M31.

The radial averaged star formation rate The radial averaged SFR peaks above $100 M_{\odot} \text{pc}^{-2} \text{Gyr}^{-1}$ in the center (Fig. 3.10), indicating a nuclear starburst, and drops radially to values of $3 M_{\odot} \text{pc}^{-2} \text{Gyr}^{-1}$ at 12 kpc distance. Note that the C2 cluster complex studied by Bastian et al. (2005) shows a local SFR of $2600 M_{\odot} \text{pc}^{-2} \text{Gyr}^{-1}$, while the other complexes studied by these authors show moderate local rates of $\sim 60 - 70 M_{\odot} \text{pc}^{-2} \text{Gyr}^{-1}$.

Regions of more than $\sim 100 M_{\odot} \text{pc}^{-2} \text{Gyr}^{-1}$ (i.e. $0.1 M_{\odot} \text{kpc}^{-2} \text{yr}^{-1}$) are classified as starbursts (e.g. Kennicutt 1998). The center of M51 harbors a Seyfert 2 AGN surrounded by a $\sim 100 \text{pc}$ disk/torus (Kohno et al. 1996) of warm and dense gas (Matsushita et al. 1998, 2004).

Schmidt law Fig. 3.10 shows the variation of the radially averaged star formation rate in comparison with the H I, H₂ and the total gas surface density in M51. Ignoring the center, the radial drop of the star formation rate closely resembles the drop of the total gas surface density. Neither does the SFR show the rather flat distribution of the atomic gas nor the much steeper drop of the molecular gas. In contrast, we would have anticipated a good correlation of the star formation rate with the molecular gas since star formation is known to occur only in molecular clouds. Indeed, Heyer et al. (2004) find a strong correlation between the star formation rate and the molecular gas surface density in M33. Similarly, Wong & Blitz (2002) report a much better correlation of $\dot{\Sigma}_{\text{SFR}}$ with Σ_{H_2} than with $\Sigma_{\text{H I}}$ in their sample of 6 molecule-rich spirals. However, Kennicutt (1998) who studied 88 galaxies and found that the disk-averaged SFR is much better correlated with the disk-averaged H I surface densities than with the H₂ surface densities. In M51, H I is often found downstream of the CO arms indicating that the H I clouds are the remnants of GMCs photo-dissociated by young massive stars (Sec. 3.3.4). The star formation rate may thus regulate the surface density of the atomic gas and hence explain the observed correlation.

Fig. 3.14 shows the variation of SFR in M51 with gas surface densities together with lines of constant gas depletion time. The gas consumption time in M51 varies between 0.1 Gyr in the center where the gas surface density and the SFR surface density are high and 1 Gyr at large radii where the gas surface density and SFR density are low (Figs. 3.10, 3.14). In contrast, the Milky Way (Misiriotis et al. 2006) and the 6 CO-bright spiral galaxies studied by Wong & Blitz (2002) exhibit gas depletion times which are larger by a factor of about 10. They rise from $\sim 1 \text{Gyr}$ in the centers to $\sim 10 \text{Gyr}$ and slightly more in the outskirts.

Fig. 3.14 also shows that the star formation rate is proportional to a power of the total gas surface density in M51

	A	n	Reference
Local Schmidt laws:			
M51	1.12 ± 0.50	1.35 ± 0.61	this thesis
M33	3.5 ± 66	3.3 ± 0.07	Heyer et al. (2004)
Milky Way		2.18 ± 0.20	Misiriotis et al. (2006)
7 CO-bright spiral galaxies		1.7 ± 0.3	Wong & Blitz (2002)
16 spiral galaxies		~ 2	Boissier et al. (2003)
simulations	0.25 ± 0.16	1.31 ± 0.15	Li et al. (2006)
Global Schmidt laws:			
97 normal and starburst galaxies	0.25 ± 0.07	1.4 ± 0.15	Kennicutt (1998)
7 CO-bright spiral galaxies		1.7	Wong & Blitz (2002)
simulations	0.11 ± 0.04	1.56 ± 0.09	Li et al. (2006)

Table 3.3: Schmidt law $\dot{\Sigma}_{\text{SFR}} = A\Sigma_{\text{gas}}^n$ observed in M51 and other galaxies and samples of galaxies in comparison with the Schmidt law derived simulations. $\dot{\Sigma}_{\text{SFR}}$ and A are in units of $M_{\odot}\text{pc}^{-2}\text{Gyr}^{-1}$ and Σ_{gas} in units of $M_{\odot}\text{pc}^{-2}$. The values of the sample of Wong & Blitz (2002) hold for an extinction correction that depends on the gas column density.

$$\dot{\Sigma}_{\text{SFR}} = A\Sigma_{\text{gas}}^n \quad (3.9)$$

i.e. follows a Schmidt law (Schmidt 1959), with normalization $A = 1.1 \pm 0.5$ and the slope $n = 1.4 \pm 0.6$ where $\dot{\Sigma}_{\text{SFR}}$ is in units of $M_{\odot}\text{pc}^{-2}\text{Gyr}^{-1}$ and Σ_{gas} in units of $M_{\odot}\text{pc}^{-2}$.

The Schmidt law in other galaxies In Table 3.3, the result in M51 is compared with other galaxies and the results from simulations. The slope found in M51 agrees with the global Schmidt law, seen in a study of disk-averaged Σ_{gas} and $\dot{\Sigma}_{\text{SFR}}$ of 61 normal and 36 starburst galaxies (Kennicutt 1998). Note however, that the slope of the 61 normal galaxies is much less well-defined. Depending on the fitting method it varies between 1.3 and 2.5 (Kennicutt 1998).

In contrast, the observed slopes of *local* Schmidt laws, describing radial averages of Σ_{gas} and $\dot{\Sigma}_{\text{SFR}}$ in individual galaxies, do not in general agree with the global value, but vary strongly between 1.2 and 3.3. Wong & Blitz (2002) studied radial averages of Σ_{gas} and $\dot{\Sigma}_{\text{SFR}}$ in a sample of spiral galaxies and derive local Schmidt laws with slopes between 1.2 and 2.1, assuming that extinction depends on gas column density. Boissier et al. (2003) study 16 spiral galaxies to study the local star formation laws and find a slope of ~ 2 . In a similar study, Heyer et al. (2004) shows that M33 exhibits a significantly steeper slope of 3.3. Misiriotis et al. (2006) find a slope of 2.2 for the Milky Way.

3.6.5 The local Schmidt law and star formation efficiency in simulations

Recent smoothed particle hydrodynamics (SPH) simulations of gravitational instability of isolated disk galaxies comprising a dark matter halo, a disk of stars, and isothermal gas by Li et al. (2005, 2006) find a slope of 1.31 of the local Schmidt law (Table 3.3), close to the slope of the global Schmidt law, which is also reproduced, and close to the slope of 1.35 found in M51. On the other hand, the slope of 1.3 is at the low-end of the local Schmidt law slopes observed so far.

We find a normalization factor A of the local Schmidt law in M51 of $1.12 M_{\odot} \text{pc}^{-2} \text{Gyr}^{-1}$ (Table 3.3), similar to A of gas-rich models in Li et al. (2006). This is a factor 5 larger than the average value of the Li et al. (2006) models. It is also a factor 5 larger than the normalization found in the large sample of Kennicutt (1998).

Interestingly, the normal galaxies of the Kennicutt (1998) sample show on average a factor ~ 3 longer gas consumption times than found in M51. In section 3.6.4 we also noticed that the Milky Way (Misiriotis et al. 2006) and the 6 CO-bright galaxies studied by Wong & Blitz (2002) exhibit consumption times which are larger than the consumption time found in M51 by about one order of magnitude. Apparently, the star formation efficiency of M51 is higher than in many other normal galaxies.

The reason may be the interaction of M51 with its neighboring galaxy NGC 5195, as has been proposed before as mentioned in the Introduction (e.g. Nikola et al. 2001; Howard & Byrd 1990; Toomre & Toomre 1972). This is supported by the recent simulations of Li et al. (2004) which show that interaction and merging can lead to instable disks and strong starbursts.

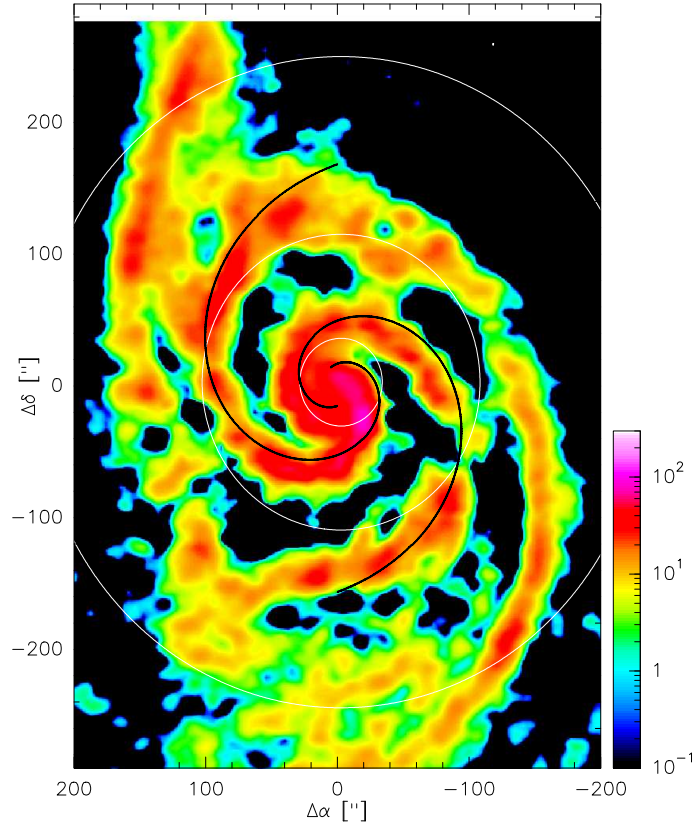


Figure 3.15: The residual map of the total gas surface density after removal of a fitted underlying exponential disk. The exponential disk is shown in contours with contour levels $1 M_{\odot} pc^{-2}$, $5 M_{\odot} pc^{-2}$ increasing to $20 M_{\odot} pc^{-2}$ in steps of $5 M_{\odot} pc^{-2}$.

3.7 The structure of the total gas density

An underlying exponential disk in M51

Before entering in the stability analysis of the disk, the structure of the total gas density in M51 is further investigated. Following the analysis of an underlying exponential dust disk by Meijerink et al. (2005) using $850\mu m$ dust emission observed with SCUBA at the JCMT, the properties of an exponential disk using the two-dimensional total gas density distribution

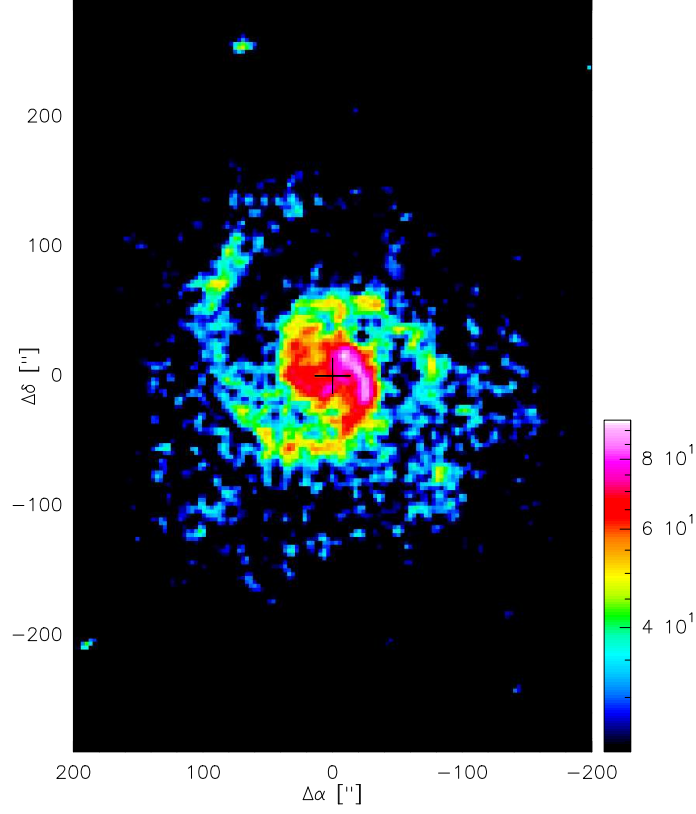


Figure 3.16: The residual map of the $850\mu\text{m}$ dust emission after removal of a fitted underlying exponential disk (Fig.2 in Meijerink et al. 2005). The 3σ -level is at 24 Jy/beam .

Table 3.4: Properties of the exponential gas disk in M51.

(a) Properties of the dust disk are from Meijerink et al. (2005)

Σ_{gas} scale length h_{gas}	$7.6 \pm 0.1 \text{ kpc}$
Amplitude: $\Sigma_{\text{gas}}^{\text{peak}}$	$17.8 \pm 0.2 \text{ M}_{\odot} \text{ pc}^{-2}$
disk/total mass-fraction gas	61%
dust scale length h_{d} (a)	6.3 kpc
Amplitude: $\Sigma_{\text{dust}}^{\text{peak}}$ (a)	$0.77 \pm 0.2 \text{ M}_{\odot} \text{ pc}^{-2}$
disk/total mass-fraction dust (a)	55%

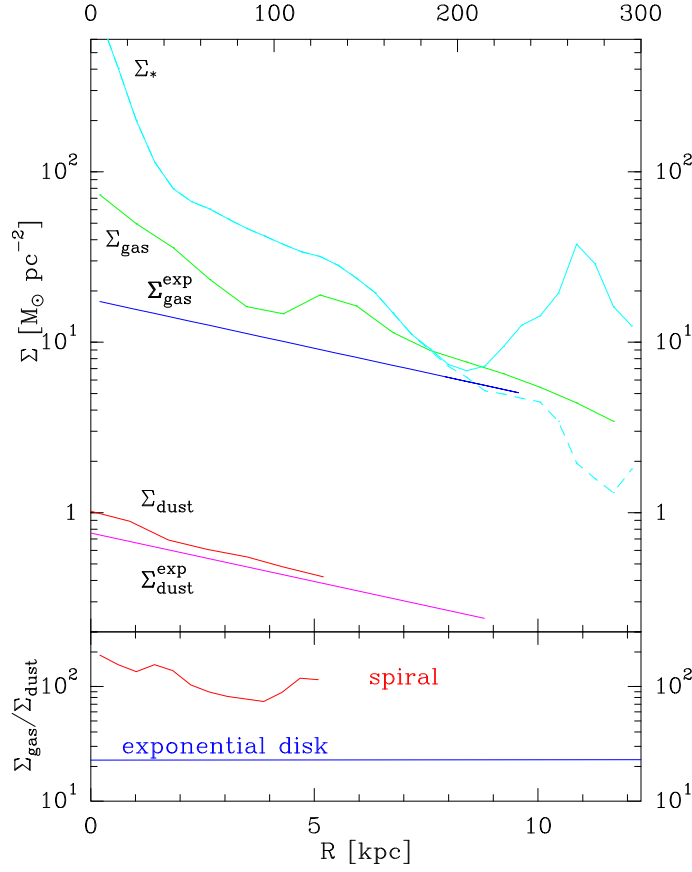


Figure 3.17: Radial averaged distribution of the stellar surface density and the total gas surface density. The dashed line shows stellar densities, ignoring the companion. The mass surface densities of the fitted exponential disks to the total gas density is also shown (cf. Fig.4 in Schuster et al. (2007)). Σ_{dust} is taken from Fig.6 in Meijerink et al. (2005). The ratio of $\Sigma_{\text{gas}}/\Sigma_{\text{dust}}$ for the exponential disk and the residual images, assuming $T_{\text{dust}} = 25\text{K}$ in the spiral arms, is shown in the lower box. Dust values below $3\sigma = 24 \text{ Jy/beam}$ are ignored

will be discussed and the results compared to the properties of the dust disk found by Meijerink et al. (2005).

Exponential disk in the total gas distribution An inclined elliptical exponential disk is fitted to the Σ_{gas} distribution map, assuming a centered disk at an inclination of 20° and a position angle of 170° . The scale length h_{gas} and the amplitude $\Sigma_{\text{gas}}^{\text{peak}}$ are determined from a 2D fit of an exponential distribution $\Sigma_{\text{gas}} = \Sigma_{\text{gas}}^{\text{peak}} \times \exp(-R/h_{\text{gas}})$. All pixels in the total gas density map exceeding a threshold surface density of $\Sigma_{\text{gas}} = 20 \text{ M}_\odot \text{ pc}^{-2}$ were blanked. This corresponds to the arm regions we marked in Fig. 3.8 and discussed in §3.4.1. A significantly higher blanking threshold leads to an overestimation of the exponential disk in the central parts as spiral arm regions are included in the fitting.

The scale length of the fitted exponential decay of the total gas disk is $h_{\text{gas}} = 7.6 \text{ kpc}$ (Table 3.4) with the peak at $17.8 \text{ M}_\odot \text{ pc}^{-2}$. The reduced χ^2 of the fit is 5.1. The fraction of total gas mass contained in the exponential disk is 61%. Thus, the spiral arms contain only $\sim 40\%$ of the total gas mass.

Exponential disk in the dust emission To derive masses from $850 \mu\text{m}$ fluxes, Meijerink et al. (2005) used a radiative transfer model to derive the stellar- and dust scale length and the temperature profile of the dust. They assumed a radial exponential density distribution and used a combined bulge and exponential disk profile for the stellar component. They derive a temperature profile varying slightly from 25 K in the center to 17 K at 10 kpc radial distance. The central dust mass surface density Σ_{dust} varies between $0.7\text{-}0.9 \text{ M}_\odot \text{ pc}^{-2}$ for the silicate to graphite fractions in the models between 0.2:0.8 to 0.5:0.5. In Fig. 3.17 the modeled dust mass surface density of Meijerink et al. (2005) for a silicate to graphite ratio of 0.5:0.5 is presented. This profile only represents the dust surface density Σ_{dust} in the fitted exponential disk.

The scale-length of the dust disk is $h_{\text{d}} = 5.45 \text{ kpc}$ corresponding to $h_{\text{d}} = 6.3 \text{ kpc}$ for a distance of 8.4 Mpc (Feldmeier et al. 1997). The fraction of the dust contained in the exponential diffuse disk is 55%, very similar to the fraction of 61% derived for the total gas. The dust fraction of 55% is derived assuming an isothermal dust disk. Note that the error caused by the difference in temperature from 25 K in the center to 17 K (Meijerink et al. 2005)

in the outer parts, is only 35% using $M_{\text{dust}}^{25\text{K}}/M_{\text{dust}}^{17\text{K}} = B_{850}(17\text{K})/B_{850}(25\text{K})$ where $B(T)$ is the Planck function.

The results found for the total gas density data confirm the importance of the underlying diffuse disk (Meijerink et al. 2005).

Gas-to-dust ratios The gas-to-dust surface density ratio of the exponential disks was derived from two independent data sets, from the CO and HI maps, and from the SCUBA 850 μm map. The radial averaged gas-to-dust surface ratio is shown in blue in the lower box in Fig. 3.17. It is nearly constant with galacto-centric radius at 23-26, about a quarter of the canonical Galactic gas-to-dust ratio of 100. This constancy is in contrast for example to the strong radial variation of the HI/H₂ surface density ratio by more than a factor 100.

Only in the inner region, where H₂ dominates the total gas mass, the X-factor to convert integrated CO intensities to H₂ column densities may play a role: As described in paragraph 3.3.2, we used an X-factor of 0.25 times the Galactic X-factor, as was found by Garcia-Burillo et al. (1993b); Strong et al. (1988).

To check for constancy in the $\Sigma_{\text{gas}}/\Sigma_{\text{dust}}$ ratio in the spiral arms, we compute the Σ_{gas} to Σ_{dust} ratio in the residual map after subtracting the exponential disk, which mainly consists of the spiral arms. This ratio is shown in red in the lower box in Fig. 3.17. The radially averaged residual total gas surface density is computed from Fig. 3.15. For the computation of dust surface density in the spiral arms, we use Fig. 2 in Meijerink et al. (2005) and assume a uniform dust temperature $T_{\text{dust}} = 25\text{K}$ and $\kappa_{850} = 1.2\text{cm}^2\text{g}^{-1}$ (Meijerink et al. 2005). The dust surface density is given via:

$$\Sigma_{\text{dust}} = M_{\text{dust}}/A_{\text{beam}} = F_{850}d^2/(\kappa_{850}B_{850}T_{\text{dust}}). \quad (3.10)$$

$F_{850} = S_{850}/\Omega_{850} \times A_{\text{beam}}$ is the integrated flux. S_{850} is the flux density, Ω_{850} the beam size and A_{beam} the beam area at the distance d . B_{850} labels the Planck-Function at 850 μm .

The resulting fraction of Σ_{gas} and Σ_{dust} in the spiral arms, shown in Fig. 3.17, is not constant with radius. In contrast to the fraction in the exponential disk, we see a strong variation in the spiral arms with a minimum of 73 at 3.8kpc and a value of 186 in the center. Thus the gas-to-dust

surface density ratio is a factor of 3-8 higher in the spiral arms compared to the underlying exponential disk. Note that the dust map in the spiral arms is contaminated with CO 3-2 line emission by up to 30-40% (Meijerink et al. 2005).

3.8 Gravitational stability

In section 2.3, the theoretical background for the Toomre approach to gravitational stability of galactic disks was introduced. Major parameters are the total gas density, which has been discussed in the last sections, and the dispersion of the gas and stars in the disk, respectively. Thus, before entering the stability analysis in M51, we present the velocity field of ^{12}CO 2-1 observations, the equivalent widths of ^{12}CO 2-1, a measure of the dispersion of the molecular gas, and the HI dispersion. Also, the residual velocities from purely rotational motions in the ^{12}CO 2-1 data are computed and used as a measure for streaming motions. The effect of streaming motions on the local dispersion which might be stabilizing the gas against collapse is estimated.

3.8.1 Kinematics of the ^{12}CO 2-1 data

Velocity field and streaming motions

In Fig. 3.18a, the velocity field of the ^{12}CO 2-1 data is shown ranging from 370 to 550 kms^{-1} with the northern part blue-shifted towards us and the southern part of the galaxy red-shifted due to the inclination of the galaxy.

For comparison, Fig. 3.18b shows the velocity field for purely circular motions derived from the rotation curve of M51 (Garcia-Burillo et al. 1993b,a). A position angle of $\Theta_{\text{MA}} = 170^\circ$ (Tully 1974a) is used to create Fig. 3.18b. Also, a constant inclination of $i = 20^\circ$ and a central velocity of $v_{\text{sys}} = 472 \text{ kms}^{-1}$ (Tully 1974a; Shetty et al. 2007) are taken as input parameters. Θ

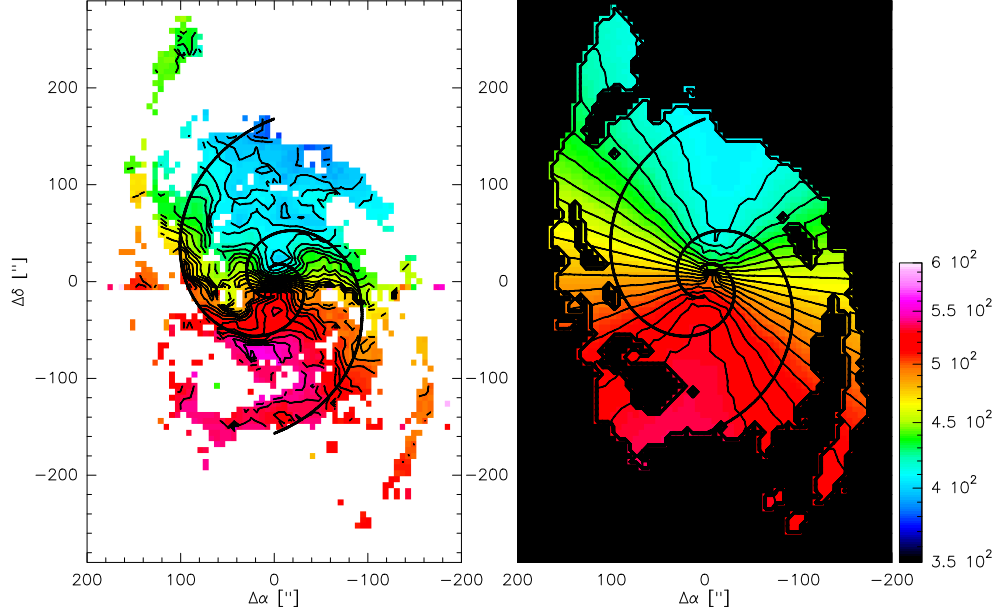


Figure 3.18: Left: Map of the first moment $v_{\text{obs}} = \int T v dv / \int T dv$ showing the intensity weighted mean velocity of the ^{12}CO 2–1 data with all points below the 5- σ -level blanked. Right: Map of the calculated velocity field v_{mod} using the rotation curve of Garcia-Burillo et al. (1993b,a). The velocity ranges from 370 to 550 km s^{-1} . Contour levels in steps of 7 km s^{-1} .

is the azimuthal angle in the disk of M51. The velocity field v_{mod} shown in Fig. 3.18 is then given at each point via

$$v_{\text{mod}} = v_{\text{sys}} + v(R) \times \cos(\Theta - \Theta_{\text{MA}}^{\text{mean}}) * \sin(i). \quad (3.11)$$

The dominant component creating the observed velocity field is the differential rotation curve $v(R)$. This creates symmetrically bending of the iso-velocity contours with respect to the position of the minor axis (Fig. 3.18a). The observed velocity field also shows many complex structures and distortions not expected from purely rotational motions.

Residual velocity The residual velocity is the difference of the observed velocity field v_{obs} (see Fig. 3.18) and the purely rotational motions v_{mod}

(see Fig. 3.18). In the following, these velocities will be also identified with streaming motions. The residual velocity map is shown in Fig. 3.19. This method to determine the non-circular streaming motions has been also presented in (Garcia-Burillo et al. 1993a).

Some of the regions showing the strongest distortions caused by non-circular streaming motions in Fig. 3.18a and Fig. 3.19 will be discussed in the following. In the inner part of the disk especially on the north-west part of the inner spiral arm at $(-80'', 50'')$ and in the south-east on the inner spiral structure at $(70'', -50'')$, strong streaming in a velocity range of around 35 km s^{-1} is evident when comparing with the purely rotational velocity field in Fig. 3.18b. Similar strong distortions of the iso-velocity contours show up at $(60'', -40'')$, also indicating strong non-circular motions in this region.

In the outer regions of the disk, next to the western spiral arm exist streaming motions in the north-west at $(-80'', 100'')$, but also in the south-west at $(-110'', -90'')$ creating a significantly different shape of the observed velocity field compared to the purely rotational velocity field. The gradients and the bending show a similar behavior as in the more central regions of strong streaming.

Interestingly, on both outer spiral arms no strong bending of the iso-velocity contours is seen and the observed velocity field resembles the purely rotational motions. This might be caused by their locations at radii of $\sim 120 - 170''$ from the center of the galaxy, which lie close to the predicted location of the corotation radius at $160''$ by Garcia-Burillo et al. (1993a,b). At this position no net streaming is expected. Next, we will compare the results obtained from the ^{12}CO 2–1 data with previous observations in M51.

Previous results on streaming motions in M51 The residual map Fig. 3.19 matches very well with the streaming motions identified by Garcia-Burillo et al. (1993a). E.g. the very prominent streaming in the north-western part of the inner spiral arm is identified at a residual velocity of -27 km s^{-1} . Also, the streaming in the south-eastern inner spiral arm occurs in both studies at the same residual velocity of around 25 km s^{-1} and shows the same shape and size. This feature extends further down south connecting

the inner spiral to the outer spiral arm in the south-west direction. A high resolution OVRO-map of the inner $30''$ showing the residuals after removing a rotation curve from the observed velocity field is presented in Aalto et al. (1999). The map shows much more detailed the very inner region of M51 at $3''$ resolution and the residuals generally agree with our $11''$ single dish observations.

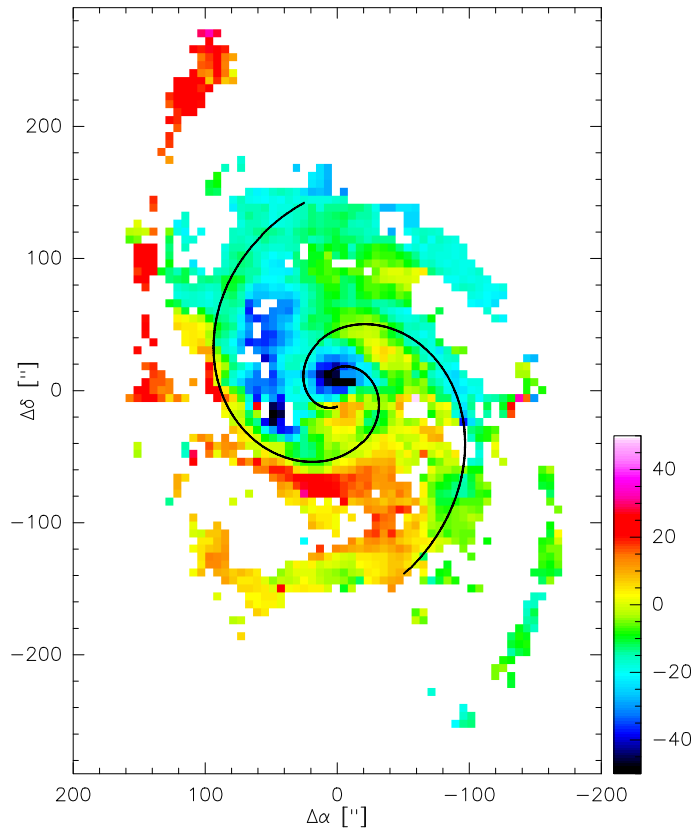


Figure 3.19: Map of the residuals of the observed velocity field Fig. 3.18a corrected for by the modeled velocity field Fig. 3.18b: $v_{\text{obs}} - v_{\text{mod}}$ [km s^{-1}].

Non-circular streaming motions in M51 have been previously observed in HI and CO by several authors (Tilanus & Allen 1989; Vogel et al. 1988; Garcia-Burillo et al. 1993a; Aalto et al. 1999). The former studies mainly concentrated on the central part of M51. Garcia-Burillo et al. (1993a) investigated the ^{12}CO 2–1 gas kinematics in the central $150''$ of M51 at a

similar resolution.

Shetty et al. (2007) present the ^{12}CO 1–0 velocity field at $6''$ resolution covering the whole disk of M51 including the companion. They discuss radial and tangential components of the observed velocity depending on the arm phase. To accurately determine these components, the systemic velocity, position angle and inclination are determined by the authors using a 2D-fit to the data and thus minimizing the error on the radial and azimuthal component splitting of the velocity field.

The radial and azimuthal velocity profiles determined by Shetty et al. (2007) in M51 show a complex structure. Velocity profiles associated with the eastern inner spiral arm qualitatively agree well with density wave theory (Lindblad 1963; Lin & Shu 1964) showing a significant increase of the azimuthal velocity as the gas enters the arm. The profiles in the western inner spiral arm do not agree with this simple picture but indicate that the density wave in M51 is a superposition of different modes (Henry et al. 2003). The ^{12}CO 2–1 data lack spatial resolution to unambiguously resolve this issue. The velocity profiles at $11''$ resolution in the western spiral arm and the lack of streaming in the outer spiral arms are in general agreement with a single density wave (see model by Garcia-Burillo et al. (1993a)).

Indications for streaming in the isovelocity contours A qualitative indication of streaming motions is the bending of iso-velocity contours and the comparison with predictions of density wave theory. The opposite bending of the iso-velocity contours in arm and interarm regions of the ^{12}CO 2–1 observations in Fig. 3.18a as seen i.e. at the north-western inner spiral at around $(20'', -80'')$ in accordance with density-wave theory (Lin & Shu 1964) which predicts this kinematic effect observed in the data. We will briefly describe the mechanism creating the observed velocity profiles.

Density-wave theory, introduced in chapter 2, predicts opposite bending of the iso-velocity contours in the arm and interarm regions (Lin & Shu 1964). For trailing spiral arms the gas upstream of the spiral arm streams radially outwards and slows down its rotation as it enters the spiral potential. After that it will be accelerated tangentially along the potential (Garcia-Burillo

et al. 1993a). This behavior is prominently seen along the minor axis. In the interarm-region, before entering the spiral arm, the iso-velocity contours bend in the northern direction. As the gas gets attracted by the spiral potential, it first slows down its rotation which is seen in a bending in the southern direction as the velocity changes towards the central velocity. Near the spiral arms, the gas gets dragged along the spiral arm. Before leaving the arm, the bending changes again towards the northern direction as the gas movement is again dominated by rotation. However, the overall velocity field in M51 is complex and may consist of a superposition of different modes of a density wave (Henry et al. 2003).

Equivalent widths

¹²CO 2–1 For the analysis of the gravitational stability using the Toomre criterion, the velocity dispersion of the gas is an important parameter possibly stabilizing the gas locally. The map of equivalent ¹²CO 2–1 line widths $\Delta v_{\text{eq}} = \int T dv / T_{\text{pk}}$ is shown in Fig. 3.20.

The maximum equivalent widths are observed in the center with values reaching up to 100 km s^{-1} . The inner spiral structure is clearly visible having enhanced Δv_{eq} between 20 and 70 km s^{-1} decreasing with galactocentric radius. In the south-western inner spiral arm, regions with high equivalent widths at $(80'', -50'')$ are correlated with strong distortions of the iso-velocity contours. Regions with a distance greater than $100''$ from the center show a significantly lower equivalent width of $15\text{--}20 \text{ km s}^{-1}$. At $(60'', 100'')$ there is a break of the equivalent widths of the inner spiral arm. They decrease to $15\text{--}20 \text{ km s}^{-1}$ although the spiral arm continues.

In the outer regions, only some regions at the center of the companion NGC5195, in the south-east at $(-100'', -100'')$ and in the north-east at $(100'', -100'')$, show increased equivalent widths of around 40 km s^{-1} and bending of the iso-velocity contours. The outer spiral arms only show increased equivalent widths at $(-100'', -100'')$ at the connecting arm with the companion. On the south-western outer spiral arm we observe uniform equivalent widths of around 15 km s^{-1} . Next, the dispersion of atomic component traced by H I emission is discussed.

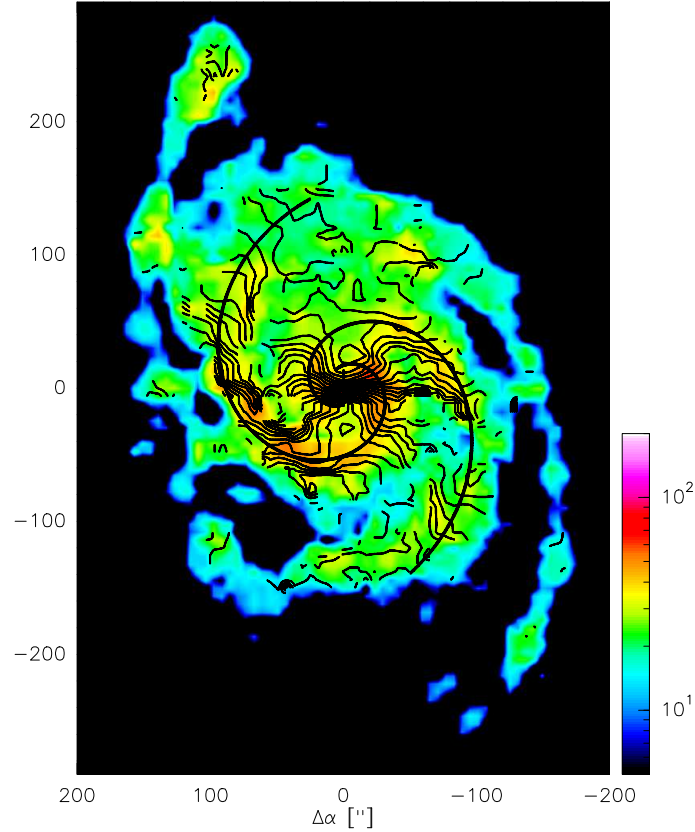


Figure 3.20: Map of the equivalent width Δv_{eq} of the ^{12}CO 2-1 emission in kms^{-1} . In contours the velocity field is shown from 350 kms^{-1} to 600 kms^{-1} in steps of 7 kms^{-1} .

H I In Fig. 3.21 the square root of the second moment $M_2^{1/2} = \sqrt{T v^2 dv / \int T dv}$ of the H I emission is shown. For a Gaussian line profile: $M_2^{1/2} = \text{FWHM} = \Delta v_{\text{eq}}$.

The second moments show values of around $30\text{-}50 \text{ kms}^{-1}$ in the central part. In the spiral arm regions in the inner part as well as in the outer spiral arms the second moment is at $10\text{-}20 \text{ kms}^{-1}$. The spiral arms show higher values of M_2 compared to the interarm regions. E.g. in the inner interarm region at $(0'', 100'')$ M_2 shows values up to 40 kms^{-1} which is significantly higher compared to the arm regions. Towards the companion, the second moments increase again reaching values comparable to the values

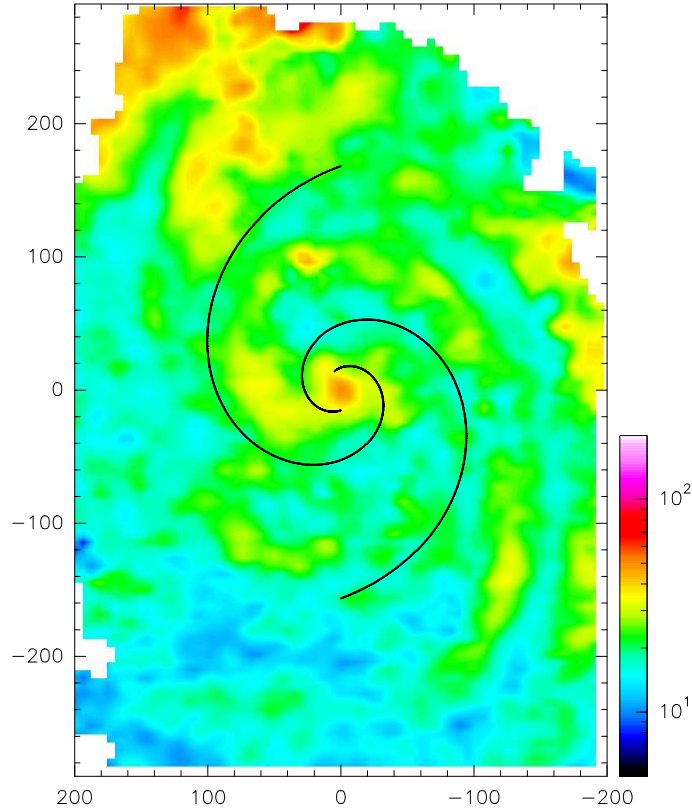


Figure 3.21: Map of the square root of the second moment $M_2^{1/2} = (\int T v^2 dv / \int T dv)^{1/2}$ of the H I emission in kms^{-1} . We blanked the M_2 -map where the H I surface density drops below the $3\text{-}\sigma$ level of $1.33 M_\odot \text{pc}^{-2}$.

in the central region. In Fig. 3.22 the radial averaged velocity dispersion of ^{12}CO 2–1, H I and the stellar component of the disk are shown. The gas dispersions resemble the features described in the maps before. In the radial averages the H I dispersion is higher compared to the CO dispersion from a galactocentric radius of 5 kpc (Fig. 3.22).

Comparison of CO and H I equivalent widths

The radial averaged dispersion of the molecular gas exceeds the atomic dispersion up to a radius of 4 kpc (Fig. 3.22). The decrease of the dispersion of atomic component in the inner part from around 20 to 10 kms^{-1} within

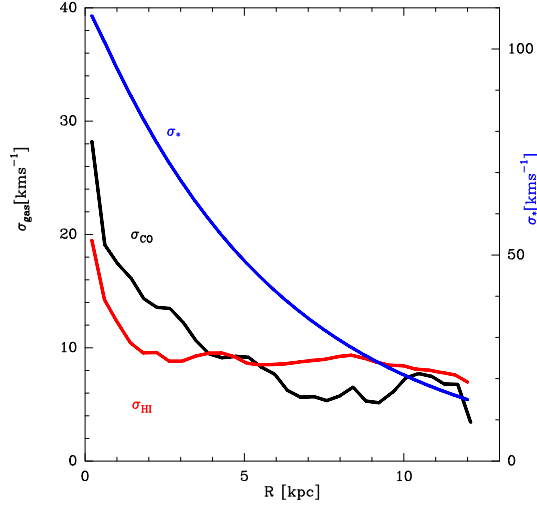


Figure 3.22: Radial averages of the velocity dispersion of CO (σ_{CO}), HI (σ_{HI}) and the stellar component (σ_*).

2 kpc is steeper compared to the decrease of the CO dispersion. The radial averaged atomic component then stays constant at around 10 km s^{-1} out to radii of 12 kpc. The CO dispersion drops to 6 km s^{-1} below the atomic dispersion at radii of around 6 kpc and increases to 11 km s^{-1} outwards due to the increased dispersion in the center of the companion.

Averaged dispersion in spiral arm and interarm regions The average values of the equivalent widths in the inner spiral arm regions, defined in Fig. 3.8, are 25.9 km s^{-1} in CO and 21.5 km s^{-1} in HI (see Tab. 3.5). In the outer spiral arms the difference is bigger with the HI widths at 18.3 km s^{-1} compared to 11.1 km s^{-1} in CO. In the interarm regions the HI widths are 19.4 km s^{-1} are on average significantly broader compared to CO at 7.3 km s^{-1} .

The averaging of the interarm region includes the south-western regions at $(-50'', -200'')$, where the HI widths are significantly smaller compared to the inner interarm regions. Fig. 3.21 reveals in the inner region that HI interarm widths exceed the line widths on the spiral arm regions. E.g. the western inner spiral arm shows HI widths down to 10 km s^{-1} while the interarm region exhibits values up to 40 km s^{-1} . This situation is reversed compared to the picture seen in the CO equivalent widths. We try to give

a interpretation of this scenario next.

Table 3.5: Equivalent widths Δv_{eq} of CO and HI in M51 averaged over the areas shown in Fig. 3.8.

	$\Delta v_{\text{eq}}(\text{CO})$ [kms ⁻¹]	$\Delta v_{\text{eq}}(\text{HI})$ [kms ⁻¹]
inner spiral arms	25.9	21.5
outer spiral arms	11.1	18.3
interarm region	7.3	19.4
ratio inner/outer spiral	2.3	1.2
inner arm/interarm	3.6	1.1
outer arm/interarm	1.5	0.9

Dissociation scenario for the observed line widths The following scenario may explain the observations (cf. Garcia-Burillo et al. 1993b; Rand et al. 1992): the dispersion of the molecular gas is enhanced in the spiral arms due to frequent collisions of molecular clouds which may be enhanced by streaming motions driven by the density wave. The atomic clouds in the arms appear to form a different population as their local velocity dispersion is much less compared to the molecular gas. We speculate that thus HI in the arms stems mainly from photo dissociated H₂ in GMCs, where the dispersion has already decreased due to dissipation. The interpretation of VLA HI and OVRO CO observations by Rand et al. (1992) also favors this dissociation scenario.

Stars The stellar velocity dispersion, shown in Fig. 3.22, is another important parameter for determining the gravitational stability of the combined disk of gas and stars. In combination with the CO and HI dispersion it is briefly presented here and later used to determine the stability of the stellar component.

For the estimation of the stellar velocity dispersion in M51, this analysis follows Boissier et al. (2003) and Bottema (1993). They showed that the velocity dispersion follows an exponential fall-off $\sigma_{\text{stars}} = \sigma_0 \exp(-R/2h_B)$

depending on the scale length of the B-band h_B of the disk. The B-band scale length is $h_B = 2.82$ kpc (Trewheella et al. 2000) and the central stellar velocity dispersion in M51 is $\sigma_0 = 113$ kms^{-1} (McElroy 1995).

Rotation curve

The rotation curve of M51 is needed to calculate the epicyclic frequency, introduced in chapter 2, the last missing parameter for the Toomre analysis in M51. The rotation curve of M51 was derived by Garcia-Burillo et al. (1993b,a) from the CO 2–1 position-velocity diagram along the major axis of M51, using the velocities at the peak intensities, and correcting for the inclination. The rotation curve (Fig. 3.23) rises steeply within $10''$ of the center indicating the presence of a compact nuclear mass component in addition to the central bulge and then stays constant at ~ 200 kms^{-1} out to a radius of 10 kpc. We assume here that the rotation curve stays almost constant further out to at least 12 kpc, ignoring any effect of the companion galaxy. The definition of the rotation curve used here appears to be more appropriate for the face-on galaxy M51 than the definition used by Sofue (1996) who derived the rotation curve from the terminal velocities at which the peak intensity has dropped to 20% of its value, which leads to very high velocities of upto 260 kms^{-1} at radii between 3 and 9 kpc. Next, the stability of the disk is studied using the Toomre criterion.

3.8.2 Radial Toomre analysis for the gaseous disk

We introduced the Toomre criterion for gravitational stability in section 2.3. The stability analysis for M51 is presented in a two step approach: this section deals with the gaseous disk only and the contribution from the stellar component is neglected. This is important to be able to compare to similar approaches in other galaxies. The next section includes the stellar component and shows its importance for the gravitational stability of the disk.

The Toomre parameter (Toomre 1964) for a gaseous disk is defined as

$$Q_{\text{gas}}(R) \equiv \frac{\Sigma_{\text{crit}}(R)}{\Sigma_{\text{gas}}(R)} = \frac{\kappa(R)\sigma_{\text{gas}}(R)}{\pi G \Sigma_{\text{gas}}(R)}, \quad (3.12)$$

describing the competition of pressure and rotation on the one side and gravitation on the other side, at a given radius. If Q_{gas} is less than 1, i.e. when the gas surface density exceeds the critical surface density, the disk is unstable against axisymmetric perturbations.

In the following, it is assumed that the gaseous disk of M51 is almost unstable as predicted by disk models (e.g. Lin & Pringle 1987), i.e. $Q_{\text{gas}} = 1$, to calculate the critical gas velocity dispersion σ_{crit} necessary to stabilize the gas against gravitational collapse. Using these assumptions, σ_{crit} is compared to the observed velocity dispersion of the molecular gas, σ_{CO} , as function of the galacto-centric radius.

Critical velocity dispersion

Fig. 3.23 shows the radially averaged critical velocity dispersion σ_{crit} derived from the gas surface density and the rotation curve, assuming $Q_{\text{gas}} = 1$ (Equation 3.15). The critical dispersion, necessary to stabilize the gas against gravitational collapse, lies between 1.7 and 6.8 km s^{-1} . The dispersion peaks near $R = 5.5$ kpc where the H_2 surface density is high (Fig. 3.10). It then declines slowly to $\sim 2 \text{ km s}^{-1}$ at $R = 12$ kpc.

Observed velocity dispersion

The velocity dispersion of the molecular gas is estimated here from the equivalent ^{12}CO 2–1 line widths $\Delta v_{\text{eq}} = \int T dv / T_{\text{pk}}$ via $\sigma_{\text{CO}} = \Delta v_{\text{eq}} / (2\sqrt{2 \ln 2})$.

The map of the CO equivalent widths was discussed and presented in Fig. 3.20. To compare to the radial prediction of the critical dispersion from the Toomre criteria, Fig. 3.23 shows the radially averaged velocity dispersion σ_{CO} . It drops from $\sim 28 \text{ km s}^{-1}$ in the center to $\sim 6 \text{ km s}^{-1}$ at radii of 7 to

9 kpc. Further out, it rises again to values of $\sim 8 \text{ km s}^{-1}$. The rise of the observed dispersion at radii of 10-13 kpc, is due to the increased line widths in the companion galaxy.

The CO velocity dispersion observed in M51 exceeds the critical dispersion at all radii. The ratio between the observed and the critical dispersions drop from a factor of ~ 5 to almost 1 for radii between 1 and 5 kpc. This may indicate that the gas is stabilized against collapse at all radii.

However, the observed gas dispersions are averages over the 450 pc beam and along the elliptical annuli, and are broadened relative to the intrinsic dispersions due to systematic motions which might not contribute necessarily to local support of the gas against gravity. The influence of the previously discussed streaming motions on the gravitational stability as well as the influence of stars will be investigated in the next section. First, the gas-only stability analysis results are discussed in the context of the literature and similar studies.

3.8.3 Discussion of the radial Q_{gas} analysis

Several authors have argued that galactic disks are self-regulated through gravitational instabilities to have their Toomre Q parameter of the order of 1 (see e.g. Combes 2001). As soon as gas dissipation leads to $\Sigma_{\text{gas}} > \Sigma_{\text{crit}}$ at a given radius, the disk becomes gravitationally unstable, leading to density waves transferring angular momentum, causing dissipation and heating of the gas and thus an increase of the velocity dispersion, stabilizing the disk again. Models indeed indicate that the disk settles at the border of instability (Lin & Pringle 1987).

Observationally, Q_{gas} has often been found to be larger than 1 by factors of a few. Kennicutt (1989) derived radial averages of the Toomre-parameter of a sample of 15 galaxies, assuming a constant velocity dispersion of 6 km s^{-1} , and found that star formation is restricted to regions where $Q_{\text{gas}} < 1.5$. A similar conclusion was drawn from a study of 32 nearby spiral galaxies by Martin & Kennicutt (2001) with few exceptions.¹⁵ Similarly, Wong & Blitz

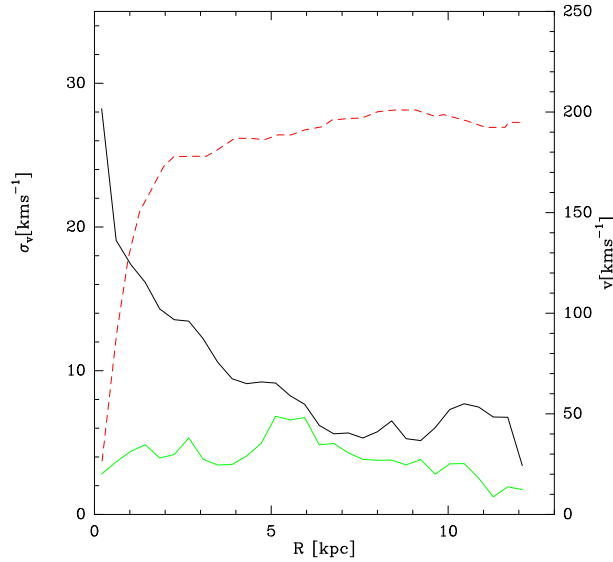


Figure 3.23: **Left:** The black drawn line shows the ^{12}CO 2–1 gas dispersion σ_{CO} derived from the observed equivalent widths. Positions without detection of ^{12}CO are ignored. The green drawn line shows the gas dispersion σ_{crit} , assuming gravitational stability, i.e. $\Sigma_{\text{crit}} = \Sigma_{\text{gas}}$. **Right:** The dashed line gives the rotation curve derived by Garcia-Burillo et al. (1993a).

(2002) also assume a constant velocity dispersion and find $\Sigma_{\text{gas}} \approx \Sigma_{\text{crit}}$ over a wider range of radii for some of their galaxies while others show deviations of factors of ~ 2 .

While in the inner 4 kpc of M51, the gas dispersion is large and Q_{gas} lies between 2 and 5, the stars may contribute here, and push the disk towards gravitational collapse. In the outer parts the observed CO dispersion is near the dispersion expected for a self-regulating disk.

¹⁵Both, Kennicutt (1989) and Martin & Kennicutt (2001) included M51 in their sample, using FCRAO 50'' CO 1–0 data combined with H α data. However, the Toomre parameter and its variation with radius in M51 are not explicitly discussed.

3.8.4 The combined Toomre parameter Q_{total}

Next, we investigate the gravitational stability of the disk of M51 using the Toomre Q -parameter, taking into account the stellar and gaseous contribution. In general, the Toomre stability criterion is depending on the epicyclic frequency $\kappa(R)$, the velocity dispersion $\sigma(R)$ of the component considered, and the surface density Σ (Toomre 1964):

$$Q = \frac{\kappa(R)\sigma(R)}{\pi G \Sigma}. \quad (3.13)$$

Map of Q_{gas} Assuming the molecular and the atomic gas in the disk of M51 are two independent isothermal fluids, the expansion in wavenumber by Wang & Silk (1994) can be applied, neglecting quadratic and higher order terms in the wavenumber i.e. in the velocity dispersions. The combined Toomre parameter for the gas in this approximation is:

$$Q_{\text{gas}}^{-1} = Q_{\text{H}_2}^{-1} + Q_{\text{H I}}^{-1}. \quad (3.14)$$

For $\kappa(R)$, the rotation curve derived from CO is used. For $\sigma(R)$, we use the dispersions derived from CO and H I respectively.

Fig. 3.24 shows the map of Q_{gas} . The central part shows Q_{gas} parameters above 10 which is mainly caused by the enhanced velocity dispersions in the center. Especially the nuclear region in the inner $10''$ the disk is significantly above the threshold for being gravitationally unstable. The steep rotation curve may also lead to a broadening of the velocity dispersion in this very inner region. On the two inner spiral arms the Q_{gas} parameter drops to values of around 2 and slightly below. Some regions e.g. at $60''/60''$ drop below the threshold of 1 and become instable to collapse. There are also some spur like structures with Q_{gas} significantly above the critical level disrupting the spiral arms. The whole map but especially the inner region shows the trend of higher gravitational stability in the interarm regions which is mainly caused by the lower gas surface density.

In the outer spiral arms the gas becomes less stable compared to the inner spiral arms. On the outer south-western arm Q_{gas} values on the whole arm

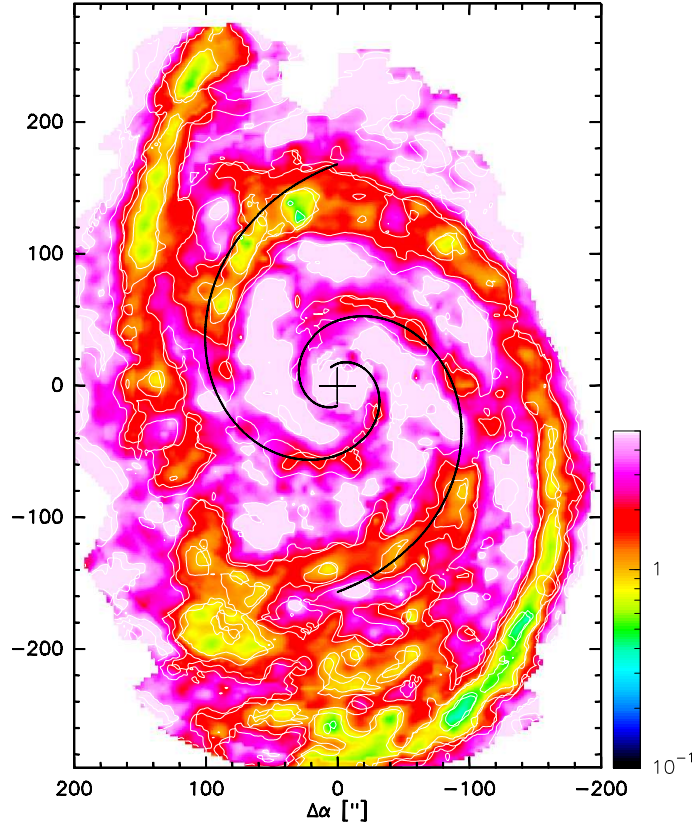


Figure 3.24: Map of the Toomre parameter for the gaseous component Q_{gas} . Pixels with Σ_{gas} below the 3σ -level are blanked. The contours show $Q_{\text{gas}} = 0.5, 1, 2,$ and 5

have values between 0.5 and slightly above 1 indicating a gravitationally critical environment. The outer north-eastern spiral arm shows Q_{gas} values between 0.5 and 3 and is generally not as unstable as the south-western spiral arm. Still, large regions on the arm are near the threshold for gravitational instability. The companion galaxy NGC5195 shows a similar behaviour as M51 with increasing Q_{gas} up to 3 towards the nucleus.

Adding the stellar component For the inclusion of the stellar component, the assumption to two independent isothermal fluids, namely gas and stars, is made. This is a model, assuming that stellar, atomic and molecular

components do not interfere with each other severely and perform frictionless motions (Wang & Silk 1994). The Q -parameter for a pure stellar disk is calculated analog to Q_{gas} . The epicyclic frequency determined from the rotation curve is assumed to be identical.

$$Q_{\text{tot}}^{-1} = Q_{\text{gas}}^{-1} + Q_*^{-1}. \quad (3.15)$$

The calculation of Q_* is based on the 2Mass K -band image smoothed to $11''$, as described before. In Fig. 3.25, the radial averages of Q_{tot} and Q_{gas} are shown.

Radial averages of Q_{tot} The radial averaged Toomre parameter Q_{tot} is at around 2 in the center increasing slightly in the inner spiral arms. To a galactocentric radius of 10 kpc the Toomre parameter always shows values between 1.5-3 close to the threshold for gravitational stability of 1. Fig. 3.25 shows the important impact of the stellar gravitational potential compared to the gas-only stability analysis. The radial averaged Q_{tot} is thus always closer to the threshold of $Q_{\text{tot}} = 1$ compared to Q_{gas} . The combined Toomre parameter is significantly lower in the central part. Q_{gas} is far from the threshold in the central region at values of around 10.

The importance of the stellar contribution has been studied by Boissier et al. (2003) using radial averages of the Toomre Q -parameter in their sample of galaxies comparing Q_{gas} and Q_{tot} . They assume a constant velocity dispersion and find that the stellar contribution lowers the Q -parameter by up to 50% towards the critical threshold. In the central part of M51, we find the impact of the stellar component to be even stronger, reducing the Q -value by around 70%.

In general, the stability parameter in the disk is near the threshold to collapse indicating self-regulation of the disk Combes (2001). Before a more detailed discussion of the results, we estimate the influence of the streaming motions on the gravitational stability.

Influence of streaming motions To study the effect of streaming motions on the stability we deconvolved the residual map (Fig. 3.19) from the

observed map of the ^{12}CO 2–1 equivalent widths Δv_{eq} (Fig. 3.20) assuming Gaussian line profiles:

$$\Delta v_{\text{corr}}^2 = \Delta v_{\text{eq}}^2 - (v_{\text{obs}} - v_{\text{mod}})^2 \quad (3.16)$$

Δv_{corr} is the intrinsic linewidth, corrected for the broadening caused by streaming motions. This reduced dispersion leads to a reduction of Q_{H_2} , which is not significant as is estimated below.

A local change of the equivalent widths Δv_{eq} propagates into Q_{gas} according to Gaussian error propagation - typical values of $Q_{\text{H}_1} = 1 - 5$, $Q_{\text{H}_2} = 1 - 10$, $\sigma_{\text{CO}} = 10\text{kms}^{-1}$ and an error of 50% on the velocity dispersion, yields absolute uncertainties in Q_{gas} of 0.04-0.56. In the radial averages, the maximum relative change between the corrected and uncorrected Q_{tot} is 7%. In the following, the streaming motions are neglected and the observed Δv_{eq} is used as a measure for the velocity dispersion of the molecular gas.

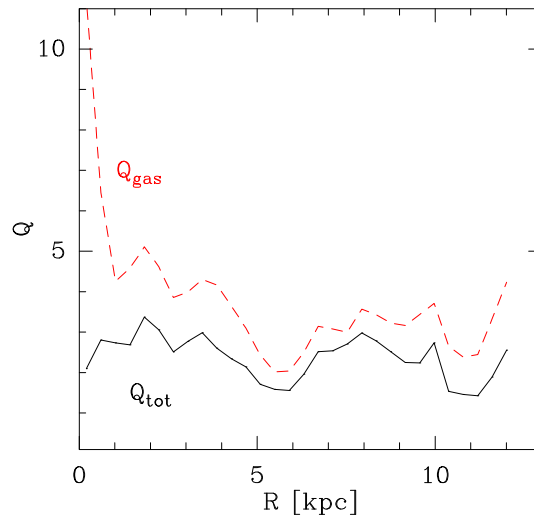


Figure 3.25: Radial average of the total Toomre parameter Q_{tot} including the stellar contribution. In red the radial average of the gas-only Toomre parameter Q_{gas} is shown.

3.8.5 The local distribution of Q_{tot}

In the following, we will discuss the gravitational stability using a map of the Toomre Q -parameter.

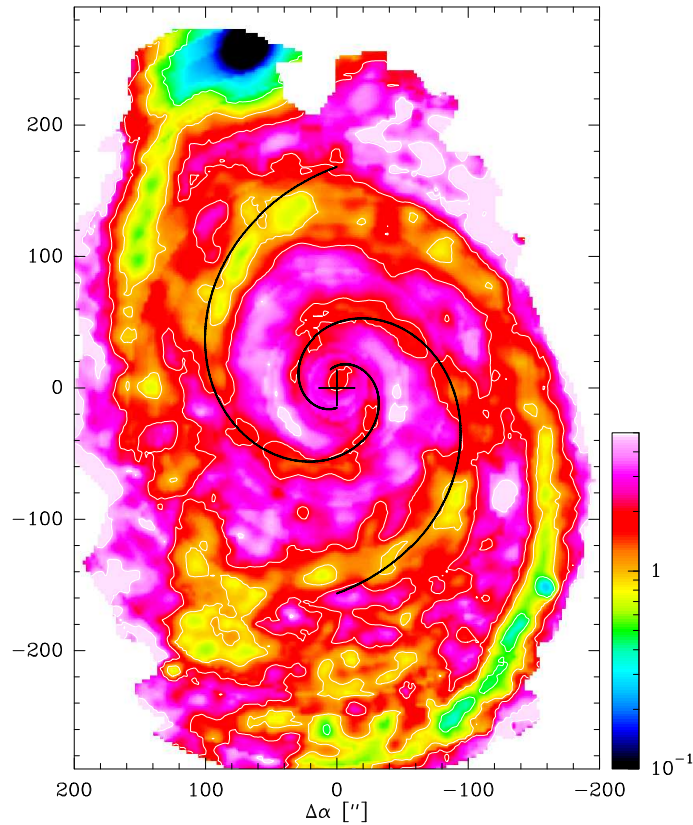


Figure 3.26: Map of the total Toomre parameter Q_{tot} including the stellar contribution. Pixels with Σ_{gas} below the 3σ -level are blanked. The contours show $Q_{\text{tot}} = 0.5, 1, 2,$ and 5 .

The inner spiral arms show Q_{tot} values between 1-2 near to the threshold for gravitational stability (Fig. 3.26). The regions between the inner spiral arms show values up to a factor of 2-3 higher as they lack surface density. Some spurs disrupting the spiral arms and connecting the spiral arms show up.

The outer south-western spiral arm is almost everywhere critical to gravitational collapse with Q_{tot} below 1 or around 1. Compared to the radial averaged analysis of the gaseous component, this result is significantly different as the stellar potential lowers the Q -value as discussed before and we only find one region at $(-130'', -60'')$ with Q_{tot} slightly above 1. The outer north-eastern spiral arm shows Q_{tot} of around 1 and below and few small regions reaching values of about 2.

Thus, in summary we see two systematic trends in Q_{tot} : a slight decrease from the central parts to the outer regions. In the spiral arms peak values decrease from $\sim 1.5 - 3$ to $\sim 0.5 - 1$. Note, that no systematic change of the gas depletion times and thus the star formation efficiency from the inner to the outer parts was found in section 3.6.4. The second evident trend is a generally lower Q_{tot} for the spiral arm regions compared to the interarm regions. In the outer disk, beyond the outer spiral arms, the disk is far from gravitational collapse based on the Toomre analysis.

Q_{total} for a constant gaseous velocity dispersion In Fig. 3.27 the total Toomre parameter using a constant velocity dispersion of the gaseous component of $\sigma = 6 \text{ km s}^{-1}$ is shown. It is closer to the critical regime in the inner part of M51 up to a radius of 4 kpc. This shows the influence of the observed velocity dispersion in the central regions where the dispersion of the gas increases the threshold for instability. In the outer part the observed dispersions are below the assumed constant velocities. The Q -parameter for the constant velocity dispersion is everywhere close to 1 and never exceeds values of 2. The comparison of the results of these different approaches is important when comparing with results in the literature. The assumption of a constant dispersion lowers the Q -value in M51, especially in the spiral arm regions. Next, we compare the obtained results to similar investigations in other galaxies.

Maps of Q_{total} in the LMC A similar study at higher spatial resolution of the total Toomre parameter combining the stellar and gaseous contribution Q_{tot} has been done in the LMC by Yang et al. (2007) using the assumption of a constant velocity dispersion. As the LMC has no prominent spiral structure, the Q_{tot} -map by Yang et al. (2007) also shows no

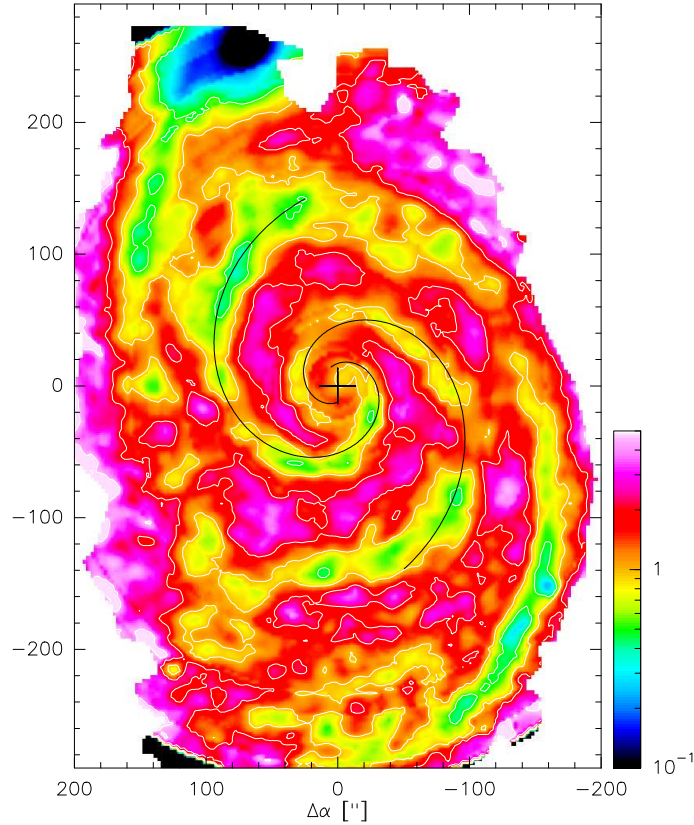


Figure 3.27: Map of the total Toomre parameter Q_{tot} including the stellar contribution, assuming $\sigma_{\text{gas}} = 6 \text{ km s}^{-1}$.

spiral arms with enhanced instability. They conclude the importance of the stellar contribution for the gravitational stability. Correlating the locations of massive young stellar objects (YSOs) in the LMC with the gravitational stability, Yang et al. (2007) find 85% inside gravitational unstable regions. This underlines the importance of gravitational stability of the disk for large-scale star formation in the LMC.

Both galaxies show large regions near the critical value for collapse indicating possible sites for star formation. The threshold density according to the Toomre approach is depending on gravity counter balanced by velocity dispersion and the epicyclic motion of the gas and stars. The result that Q_{tot} is near 1 in large areas of the disk is notable and has led other authors

e.g. Combes (2001) to speculate that self-regulation drives these galaxies near the threshold of gravitational stability and thus yielding Toomre parameters of the order of 1.

The self-regulation scenario A sketch of the feedback-cycle is the following: the birthplaces of stars are deeply embedded in dense cores of molecular clouds formed through gravitational collapse of molecular material. Once massive star formation has set in, the dispersion in the cloud is increased due to expansion of HII-regions. Stellar winds, supernovae explosions from massive stars and bipolar jets will introduce mechanical energy in the interstellar medium and locally enhance the dispersion. Before the formation of molecular clouds and subsequent dissipation leading to star formation, density waves induce turbulence on large scales via cloud-cloud collisions in spiral arms. These feedback mechanisms increase the dispersion of the gas and the Q -value.

The ionization radiation will form atomic gas from the molecular material which will subsequently cool down, become less turbulent and condensate forming new molecular clouds. The Toomre parameter will thus decrease towards gravitational instability. Globally, this regulation keeps Q near 1. In the interarm regions the gas keeps stable as no stars are formed, although these feedback mechanisms are not at work.

Simulations including feedback Shetty & Ostriker (2008) use hydrodynamic simulations including feedback to study star formation and the structure of galactic disks. They find that a simple feedback mechanism with one star formation event per cloud can not sustain a global spiral pattern in galactic disks. This indicates that the modeling of feedback needs to be improved as spiral structure is evident in observations. Quillen & Bland-Hawthorn (2008) explain episodic star formation in galaxies by strong feedback mechanisms using numerical models.

In recent 3D smoothed particle hydrodynamics simulations of isolated disk galaxies, Li et al. (2005, 2006) confirmed the major role of gravitational stability in the process of star formation and were able to examine a threshold

surface density. This evidence for the Toomre formalism in their simulations is also dominating any magnetic effects on star formation. Magnetic fields slow the collapse of the gas but do not stop it (Shetty & Ostriker 2008).

Having discussed the gravitational stability and the fraction of molecular and atomic gas in the disk of M51, next a possible correlation of both is investigated.

3.9 Correlation of Toomre Q and $\text{H}_2/\text{H I}$

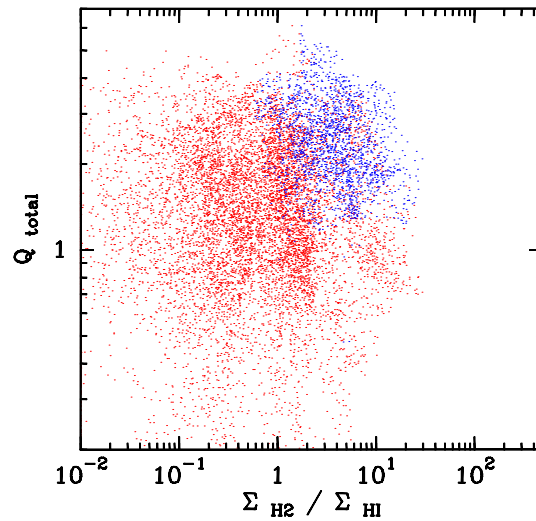


Figure 3.28: For every position in M51, the total Toomre parameter Q_{total} is plotted against the ratio of the molecular and atomic surface densities $\Sigma_{\text{H}_2}/\Sigma_{\text{H I}}$. Blue points mark the inner 70'' of galactrocentric radius.

In Fig. 3.28, the Toomre Q -parameter is correlated with ratio of molecular and atomic surface density in M51. The inner 70'' radius corresponding to the central part of the galaxy and the outer parts are discerned.

There is no correlation evident from Fig. 3.28. Low molecular gas fractions show both Q -values above and below the critical value of 1. At the molecular dominated regions the Q -value tends to be above the critical threshold, but also values below 1 occur.

Discerning between the inner $70''$ in galactrocentric radius (marked blue in Fig. 3.28) and the positions lying further outward, there is a clear trend for higher Q 's in the central part. As seen in the map of the Toomre parameter before, the main reason for a higher Q is an enhanced dispersion in this regions. From this result, a clear correlation of the gravitational stability with the fraction of molecular to atomic gas does not exist in M51.

The gravitational stability of the galactic disk in M51 determines the possible collapse of gas to molecular condensations and eventually subsequent star formation. An alternative mechanism of molecular cloud formation by Wyse (1986) is applied to M51 in the next section.

3.10 Giant Molecular Associations in M51

3.10.1 Formation and destruction of GMCs

Wyse (1986) discussed the observed differences between the radial profiles of atomic and molecular gas of disc galaxies. She suggested that random collisions between low-mass atomic clouds in the interarm region create small molecular clouds, which agglomerate into GMCs in the spiral arms. These agglomerations of molecular material have typical sizes of around 100 pc and masses of 10^2 - $10^6 M_{\odot}$. An example of a Giant molecular cloud near the Carina nebulae by the *Hubble Space Telescope* (HST) is shown in Fig. 3.29.

The collision rate of the atomic clouds is determined by how often a spiral arm is encountered which is expressed by the orbital frequency $\Omega(R)$, reduced by the pattern speed Ω_p of the spiral density wave:

$$\Sigma_{\text{H}_2} \propto (\Sigma_{\text{HI}})^2 (\Omega(R) - \Omega_p). \quad (3.17)$$

Garcia-Burillo et al. (1993b) derived a pattern speed of $\Omega_p = 27 \text{ kms}^{-1} \text{ kpc}^{-1}$ and corotation at 7.4 kpc by comparing Monte Carlo simulations of the cloud hydrodynamics in M51, with the CO data of Garcia-Burillo et al. (1993a). In the studies of Elmegreen et al. (1992); Zimmer



Figure 3.29: *HST image indicating the Giant molecular cloud associated with M16 (eagle nebula) at 2.1 kpc distance traced by HI in contours (www.spacetelescope.org).*

et al. (2004, cf.) similar values for pattern velocity and corotation radius were found. For radii outside corotation, the pattern speed Ω_p exceeds the orbital speed Ω . To estimate the collision frequency, $|\Omega(R) - \Omega_p|$ is used. Note however, that Garcia-Burillo et al. (1993b) could not exclude the presence of a second pattern excited by the tidal interaction and corotating with the companion in the outer parts.

Fig. 3.30 shows the observed Σ_{H_2} versus $\Sigma_{\text{HI}}^2 |\Omega - \Omega_p|$. Note that in this case the atomic surface density Σ_{HI} is estimated from the VLA map of integrated HI intensities by Rots et al. (1990) at $13''$ resolution. The radial averaged Σ_{HI} differs less than 20% from the more recent THINGS data.

Ignoring the singularity near corotation, a fit to the data results in a slope of 1.01 ± 0.54 , in excellent agreement with the predicted slope of 1. Equation 3.17 describes a remarkable tight correlation between the radial profiles of the molecular and atomic gas densities squared, showing that these two surface densities are related through the number of spiral arm passages. Interestingly, the seven galaxies studied by Wong & Blitz (2002) do not

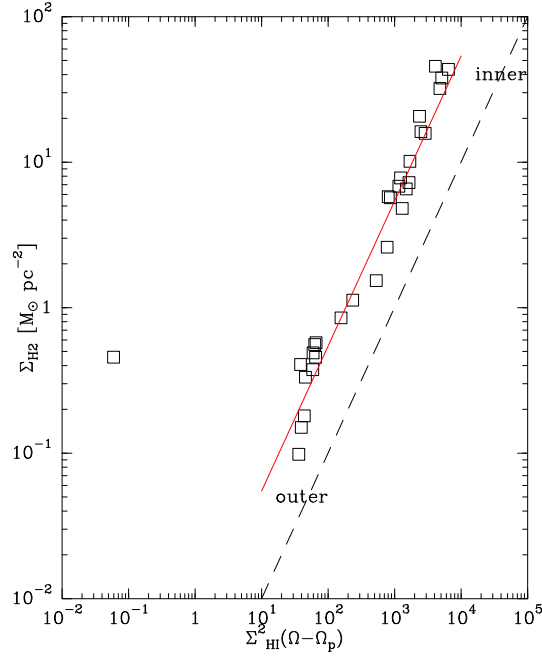


Figure 3.30: Molecular gas surface density Σ_{H_2} plotted against $(\Sigma_{\text{HI}})^2 |\Omega - \Omega_p|$. The dashed line represents a slope of 1 which holds when $\Sigma_{\text{H}_2} \propto \Sigma_{\text{HI}}^2 |\Omega - \Omega_p|$ (Wyse 1986). The drawn line shows the results of a linear fit, excluding one data point near corotation.

exhibit any such clear correlation. As already discussed in section 3.3.4, HI clouds are in general found downstream of the spiral arms throughout the disk, indicating that they are the photo dissociated remnants of GMCs. The relation proposed by Wyse (1986) thus appears to be a valid description of the destruction of GMCs, rather than their formation. In the next section, locations and properties of molecular clouds in M51 based on the ^{12}CO 2–1 observations will be studied systematically.

3.11 Molecular cloud properties

3.11.1 *Gaussclumps*

To study the properties of molecular clouds in M51, the ^{12}CO 2–1 emission of M51 has been decomposed into Gaussian shaped clouds using the *Gaussclumps* algorithm by Stutzki & Güsten (1990). Before discussing the results, an overview of the algorithm and alternative approaches is given next.

The *Gaussclumps*-algorithm has been developed to study the clumpy structure of the interstellar medium and to derive properties of the ensemble of fitted *clumps* like mass or the distribution of *clumps*¹⁶. One alternative approach for the decomposition of emission is eye-inspection (e.g. Lada et al. 1996; Blitz 1993), which is biased towards larger clumps and limited to less crowded areas. Another commonly used machine-based algorithm is *Clumpfind* by Williams et al. (1994). It identifies the local maxima in the observed intensity and assigns the 3D volume elements of the data cube to the local maxima. Thus, the clump number is fixed by the number of local maxima, while the clump shape in *Clumpfind* can be complex. The identification of weaker overlapping clumps is problematic in this scheme. Next, we will briefly describe the *Gaussclumps* algorithm, used in this thesis:

Gaussclumps iteratively fits a local Gaussian to the global maximum of the 3D-data cube (two spatial, one velocity component) and subtracts it. Additional constraints for the fit (imposed through *stiffness*-parameters) control the intensity of the fitted Gaussian with respect to the observed intensity and the relative difference in the positions of the fitted Gaussian center and the maximum intensity in the actual map. The algorithm fits the intrinsic, deconvolved widths in all three dimensions to the observed data taking into account the specified angular and spectral resolutions. It uses a modified least-square fitting procedure (as described above). *Gaussclumps* reproduced artificially created power law indices of clump ensembles with

¹⁶ We use the term *clumps* to describe the discrete units in which the emission is decomposed using *Gaussclumps*.

an accuracy of 0.1 for the powerlaw index α in the range of 1.1 to 1.75 (Stutzki & Güsten 1990). The output results are the clump center positions, widths in the two spatial and the velocity coordinates and the clump peak temperature. The properties of individual clumps, especially at the lower-mass end where the decomposition is not without ambiguities, are to be taken with caution.

The algorithm has been applied in several different molecules and sources, for example by Stutzki & Güsten (1990) in M17 using C¹⁸O 2–1 emission. E.g. Kramer et al. (1998); Simon et al. (2000) studied galactic molecular clouds using *Gaussclumps* and find clump mass spectra with a powerlaw index $\alpha = 1.8$. Below, we will apply *Gaussclumps* to identify clumps in the ¹²CO 2–1 emission of M51.

Cloud properties and selection

The IRAM data set is fully sampled on a 6'' grid with 5 kms⁻¹ velocity resolution. We will adopt the notation *Giant Molecular Associations* (GMAs) for the fitted massive clumps. This is due to the distance to M51 of 8.4 Mpc and the spatial resolution of 11'' which corresponds to 470 pc and is beyond the typical size of single GMCs of around 100 pc. Thus the lower mass limit in the result for M51 is significantly higher compared to similar galactic studies, e.g. Kramer et al. (1998).

The iterative clump-fitting algorithm was stopped in the case of the ¹²CO 2–1 data, if the peak intensity of the fitted clump went below the 3 σ limit of 0.51 Kkms⁻¹ on T_A^{*}-scale for the ¹²CO 2–1 data.

Only clumps with a deconvolved size of at least 20% beamsize in both spatial dimensions and channel width were accepted. The 155 accepted clumps of the IRAM data contain a total mass of 1.48 10⁹M_⊙ which corresponds to 78% of the total molecular gas mass found in M51.

The corresponding central clump positions fitted by *Gaussclumps* are shown on top of the ¹²CO 2–1 integrated intensity map in Fig. 3.31.

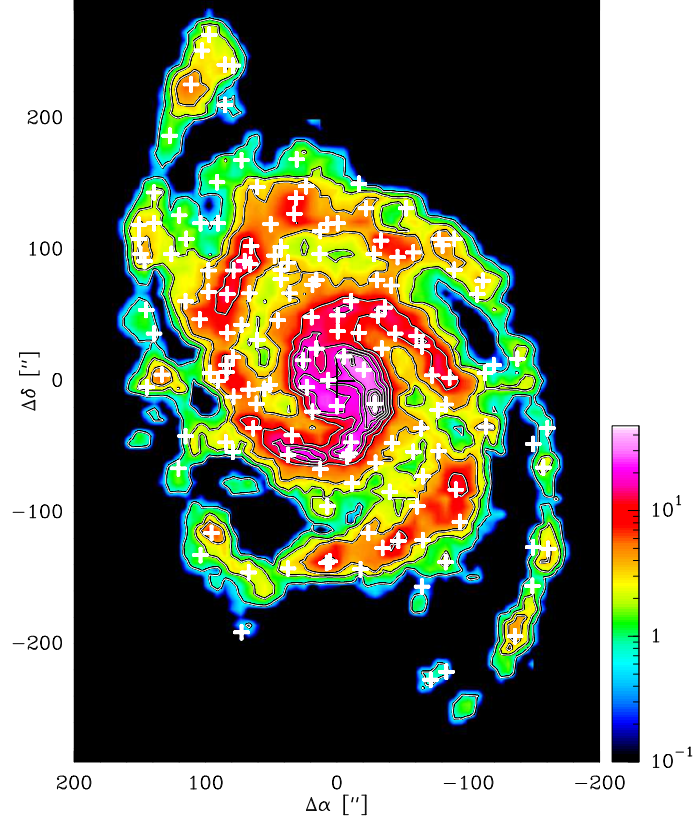


Figure 3.31: Map of the integrated ^{12}CO 2–1 intensity and the 155 clumps identified by Gaussclumps.

3.11.2 Mass and mass spectrum of clumps

The calculation of the molecular surface density of the clouds is one as described before in section 3.3.2. Assuming a Gaussian-shaped clump and a distance to M51 of 8.4 Mpc, the LTE mass is given via:

$$M_{LTE} = 3327 M_{\odot} \times T_{mb}/\text{K} \times \Delta v/\text{kms}^{-1} \times \theta_x/\text{''} \times \theta_y/\text{''}. \quad (3.18)$$

where θ_x and θ_y are the angular sizes of the half-axis of the fitted clump, T_{mb} is the main beam temperature and Δv is the FWHM line width.

The clump mass spectra is shown in Fig. 3.32. We used a least-squares fit weighted with $\Delta N^{1/2}$ to determine a power law index α of the clumpmass

distribution:

$$dN/dM \propto M^{-\alpha}. \quad (3.19)$$

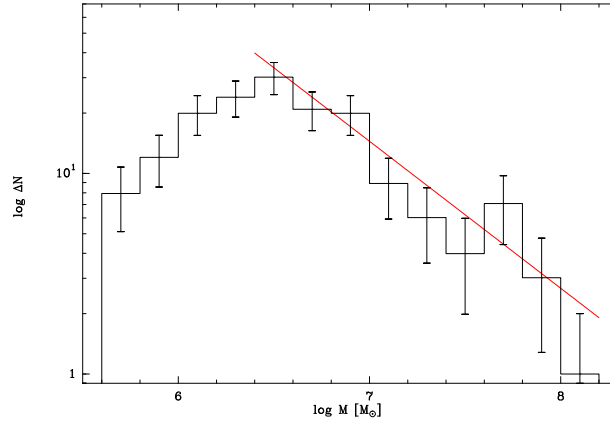


Figure 3.32: Binned mass spectrum of the accepted 155 clumps of the ^{12}CO 2–1 emission in M51.

Table 3.6: Mass spectra of GMCs and GMAs in external galaxies. The number of identified clouds is given in column 4.

Source	Distance	Resol. [pc ²]	No.	α
Antennae	19 Mpc	310×480	100	1.4 ± 0.1
M51	8.4 Mpc	450	155	1.7 ± 0.2
M33	850 kpc	50	148	2.6 ± 0.3
M31	780 kpc	90	389	1.6 ± 0.2
LMC	54 kpc	41	168	1.9 ± 0.1

The result for the power law index is $\alpha = 1.71 \pm 0.24$. The correlation coefficient is $r = 0.95$.

This result deviates significantly from the shallow power law found for the Antennae by Wilson et al. (2003) where a similar spatial resolution was achieved. The power law index in the study of the LMC (Fukui et al. 2001) is similar to our result. The spatial resolution of this study of the LMC is $2.6'$ and due to the relative proximity of the LMC thus allows to resolve masses down to single GMCs. The same is valid for the lower mass limit of

Table 3.7: Mass spectra of GMCs and GMAs in external galaxies. M_{\min} and M_{\max} are the minimum and maximum cloud mass detected. M_{turn} is the mass at the turnover of the spectrum.

Source	M_{\min}	M_{turn} [M_{\odot}]	M_{\max} [M_{\odot}]	Lit. [M_{\odot}]
Antennae	$2 \cdot 10^6$	$5 \cdot 10^6$	$9 \cdot 10^8$	Wilson et al. (2003)
M51	$5 \cdot 10^5$	$3 \cdot 10^6$	$1 \cdot 10^8$	this paper
M33	$3 \cdot 10^4$	$2 \cdot 10^5$	$7 \cdot 10^5$	Engargiola et al. (2003)
M31	$2 \cdot 10^4$	$1 \cdot 10^5$	$5 \cdot 10^5$	Muller (2006)
LMC	$4 \cdot 10^4$	$8 \cdot 10^4$	$3 \cdot 10^6$	Fukui et al. (2001)

the study by Engargiola et al. (2003) in M33. The power law found in M33 is significantly steeper than in the other galaxies (Table 3.7).

The mass range of the fitted clumps in M51 is $4.9 \cdot 10^5 M_{\odot}$ to $1.2 \cdot 10^8 M_{\odot}$ for the ^{12}CO 2–1 data. The clump mass range is of the order of the study of Supergiant Molecular Complexes in the Antennae by Wilson et al. (2003). The lower limit in our study goes about one order of magnitude deeper. The biggest GMA found in M51 has a mass of $1.2 \cdot 10^8 M_{\odot}$ and is therefore ten times less massive than the most massive complex found in the Antennae.

Spiral structure of the GMAs

An analysis of the spatial distribution of the most massive clumps found by *Gaussclumps* in M51 is presented next. As discussed by e.g. Kennicutt (1981) spiral arms of galaxies tend to resemble the shape of a logarithmic spiral.

A logarithmic spiral takes its simplest form in polar coordinates: $r(\phi) = r_0 \exp(\tan(\psi) \phi)$. Here r and ϕ are 2D polar coordinates and ψ is the pitch-angle of the logarithmic spiral. Hyperbolic and normal spiral shapes yield worse fits for the centers of the clouds in M51.

In Fig. 3.33 the two fits to the 16 most massive GMAs for a low mass cut of $2 \times 10^7 M_{\odot}$ are shown. These clumps resemble 55% of the total mass

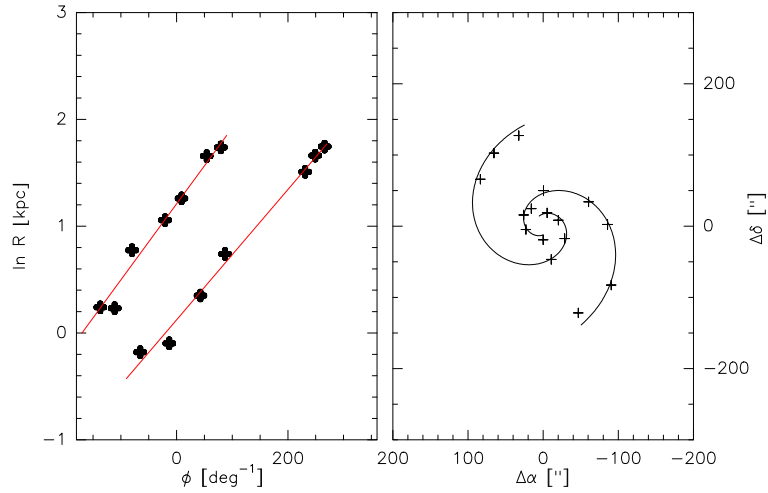


Figure 3.33: The red lines represent logarithmic spiral fits to the distribution of the 16 most massive GMAs in M51 in a ϕ - $\ln r$ -plot. These most massive clumps fitted by Gaussclumps contain 55% of the total clump mass. In the right plot the fits and position are shown on a $\Delta\alpha$ - $\Delta\delta$ -scale.

decomposed into clumps. We deprojected the center positions of the clumps using as before a position angle of 170° and a inclination of 20° and created a $\ln r$ - ϕ -plot. The linear fits give two logarithmic spirals with pitch angles $\psi_1 = 23 \pm 6^\circ$ and $\psi_2 = 20 \pm 10^\circ$ for the inner area of M51 out to a radius of 7.4kpc.

The prominent spiral shape is strongly degenerated if we include more low mass clumps. This is caused by the locations of the more massive clumps in the inner region and a strong variation of the pitch angle in the outer regions of M51. Low mass clumps can also be found on the spurs connecting the spiral arms and in some innerarm regions as shown in Fig. 3.31.

This results for the pitch angle ψ agree within the errors with the result of Kennicutt (1981) who obtains $\psi = 15 \pm 2^\circ$ for M51 via visual inspection of optical images. Shetty et al. (2007) determine a pitch angle of $\psi = 21.1^\circ$ for the spiral arms in the ^{12}CO 1–0 data in accordance with the ^{12}CO 2–1 result.

The derived spiral structure is plotted on the integrated ^{12}CO 2–1 intensity

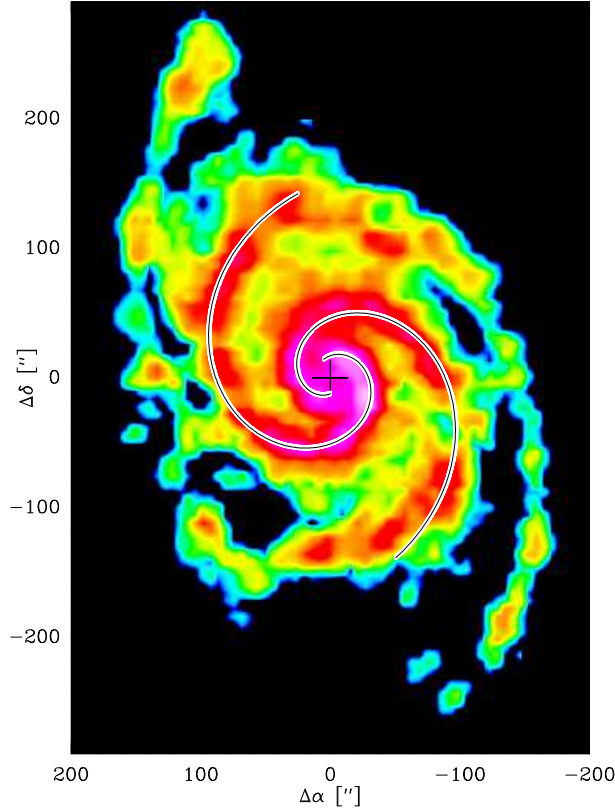


Figure 3.34: Map of the integrated ^{12}CO 2–1 intensity and the logarithmic spirals derived by the distribution of the 16 most massive clumps found by the Gaussclumps algorithm.

in Fig. 3.34 and shows a good correlation with the inner spiral arms seen in the integrated intensity.

Next, a summary of the main results obtained for M51 in the last chapter is presented.

3.12 Summary

Using the complete ^{12}CO 2–1 map of M51 combined with H1 VLA data from the THINGS team, amongst other things the total gas density and

ratio map of molecular and atomic surface density have been presented. Additionally, the radio continuum at 20 cm and 850 μ m dust emission at similar resolutions were used to study the Schmidt law, the ^{12}CO 2–1 velocity field and the combined gaseous and stellar Toomre Q -parameter. The gas-to-dust ratio in an underlying exponential disk and in the spiral arms was calculated. In details the main results are :

- Global properties: The total H_2 mass of M51 is $1.94 \cdot 10^9 M_\odot$, the total HI mass is $2.28 \cdot 10^9 M_\odot$ and the global star formation rate is $2.56 M_\odot \text{yr}^{-1}$.
- The total gas surface density drops from $\sim 70 M_\odot \text{pc}^{-2}$ in the center to $\sim 3 M_\odot \text{pc}^{-2}$ at radii of 12 kpc. The ratio of atomic to molecular gas surface density rises from 0.1 in the center to 20 in the outer regions. It is 1 at ~ 4 kpc. Up to ~ 6 kpc, the ratio follows a simple power law of $R^{1.5}$ similar to that found in other spirals. At larger radii, the simple power law relation breaks down.
- The gas depletion times in M51 vary between 0.1 and 1 Gyrs, and are shorter than in many other non-interacting normal galaxies. Simulations indeed show that interaction can lead to high star formation efficiencies.
- The star formation rate per unit area drops from $\sim 400 M_\odot \text{pc}^{-2} \text{Gyr}^{-1}$ in the starburst center to $\sim 2 M_\odot \text{pc}^{-2} \text{Gyr}^{-1}$ in the outskirts. It is much better correlated with the total gas surface density than with the surface densities of the molecular or atomic gas. The correlation follows a Schmidt law $\dot{\Sigma}_{\text{SFR}} \propto \Sigma_{\text{gas}}^n$ with an index of $n = 1.4 \pm 0.6$. Only few studies of local Schmidt laws exist to date. The slopes of local Schmidt laws observed in other spirals vary strongly between 1.2 and 3.3. The slope of 1.4 agrees with recent SPH simulations of isolated disk galaxies Li et al. (2005).
- The averaged total gas density on the inner spiral arms is at around $28 M_\odot \text{pc}^{-2}$ which is nearly a factor of 3 higher compared to the interarm regions. The ratio of molecular to atomic gas surface density is highest in the inner spiral arms at around 50 decreasing to 0.2 in the outer spiral arms.

- We fit an underlying exponential disk to the total gas density data with a scale length of 7.6 kpc. This is comparable to an underlying exponential disk in the $850\mu\text{m}$ dust continuum (Meijerink et al. 2005). The gas-dust ratio stays constant with galactocentric radius at values of 24 in the exponential disk but varies in the spiral arms from values of 80-200.
- The ^{12}CO 2–1 velocity field shows distinct differences with respect to purely rotational velocity field and a map of this residuals from purely rotational motions is shown. The equivalent width of the ^{12}CO 2–1 lines decrease from 100 km s^{-1} in the central part to less than 15 km s^{-1} in the outer regions. The second moments of HI show similar values compared with ^{12}CO 2–1 but a significantly different distribution with higher dispersion in the interarm regions and lower values on the spiral arms.
- The critical gas velocity dispersions needed to stabilize a gas-only disk against gravitational collapse in M51, vary with radius between 1.7 and 6.8 km s^{-1} applying the Toomre criterion. Observed radially averaged dispersions derived from the CO data exceed the critical dispersions by factors of 1 to 5.
- The gravitational stability using a combined stellar and gaseous Toomre parameter Q_{total} was also presented. The impact of the stellar component on the stability is significant. It lowers Q_{total} up to 70 %. The Toomre parameter is thus close to the threshold for instability $Q = 1$. The values of the Toomre parameter vary between 5 in the interarm regions decreasing to below 1 on the spiral arms. In general, the spiral arm regions are close to the threshold for gravitational instability. This result indicates self-regulation in the disk of M51.
- The Wyse relation describing the accumulation of molecular clouds from atomic clouds (Σ_{H_2} versus $\Sigma_{\text{HI}}^2|\Omega - \Omega_p|$) holds with a nearly linear slope in M51.
- The ^{12}CO 2–1 emission is decomposed into clumps using *Gauss-clumps*. The clump mass spectrum is fitted by a powerlaw with a powerlaw index $\alpha = 1.7 \pm 0.2$. The mass range of the clumps in M51 extends from $2 \cdot 10^6$ to $9 \cdot 10^8 M_{\odot}$.

Chapter 4

The physical conditions in the central regions of galaxies

4.1 Introduction

Parts of this chapter have been published in

- Hitschfeld, M., Aravena, M., Kramer, C., Bertoldi, F. and the NANTEN2-Team, *Astronomy & Astrophysics*, 2008, in press.

In this chapter, we study the physical conditions, namely the temperature, density and column density of the spiral galaxies NGC4945 and Circinus. The spiral galaxies NGC 4945 and Circinus are relatively nearby at distances of ~ 3.7 and ~ 4 Mpc. They belong to the nearest but also infrared brightest galaxies on the sky indicating strong emission also in the sub-mm domain and thus ideal targets for this study on the physical conditions using sub-mm line transitions.

First, we present the major properties of the sources and the results of previous studies in these sources. Afterwards, we introduce the observations with the new NANTEN2 submm telescope on Pampa la Bola, Chile and analyze the integrated line intensities using the escape probability formalism, which was summarized in chapter 2. Subsequently, the results of the observations and the radiative transfer modeling are compared with similar observations in other extragalactic sources.

Table 4.1: *Basic properties of Circinus and NGC 4945. L_{IR} is the total mid and far infrared luminosity calculated from the flux densities at $12\mu\text{m}$, $25\mu\text{m}$, $60\mu\text{m}$, $100\mu\text{m}$ listed in the IRAS point source catalogue (Lonsdale & Helou 1985) using the formulae given in Table 1 of Sanders & Mirabel (1996) and the distances listed below. References: ^a RC3 catalogue of de Vaucouleurs et al. (1991), ^b Mauersberger et al. (1996), ^c Freeman et al. (1977), ^d Curran et al. (1998), ^e Fullmer & Lonsdale (1989) .*

	Circinus	NGC 4945
RA(2000)	14:13:09.9	13:05:27.4
DEC(2000)	-65:20:21	-49:28:05
Type	SA(s)b ^a	SB(s)cd ^a
Distance [Mpc]	4.0 ^d	3.7 ^b
38'' correspond to	732 pc	682 pc
LSR velocity [kms ⁻¹]	434	555
Inclination [deg]	65 ^c	78 ^b
L_{IR} [$10^{10} L_{\odot}$]	1.41 ^g	1.39 ^g
S_{100} [Jy]	3.16 10^2	6.86 10^2

4.1.1 NGC 4945

NGC 4945, a member of the Centaurus group of galaxies, is seen nearly edge-on (Table 4.1) with an optical diameter of $\sim 20'$ (de Vaucouleurs et al. 1991). HI kinematics indicate a galaxy mass of $1.4 \cdot 10^{11} M_{\odot}$ within a radius of $6.3'$ with molecular and neutral atomic gas contributing $\sim 2\%$ respectively (Ott et al. 2001).

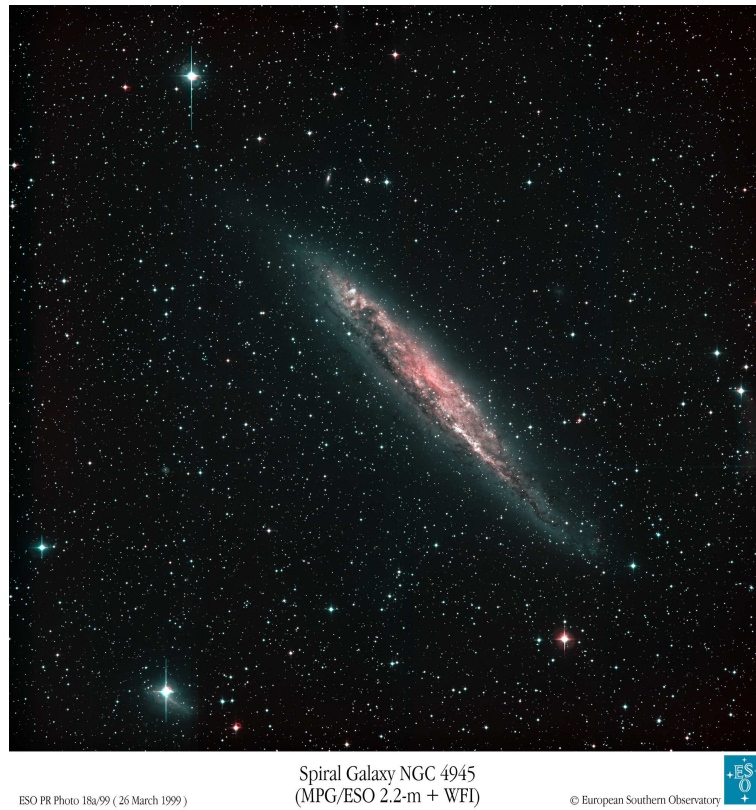


Figure 4.1: ESO optical image of the spiral galaxy NGC4945.

With a dynamical mass of $\sim 3 \cdot 10^9 M_{\odot}$ in the central 600 pc (Mauersberger et al. 1996), it is one of the strongest IRAS point sources with almost all the far infrared luminosity coming from the nucleus (Brock et al. 1988). Observations of the X-ray spectrum are consistent with a Seyfert nucleus (Iwasawa et al. 1993), and further analysis of optical imaging and infrared spectra (Moorwood & Oliva 1994) suggests that this object is in a late stage on the transition from starburst to a Seyfert galaxy. Its nucleus was the first source in which a powerful H_2O mega maser was detected (Dos Santos & Lépine 1979).

Studies in HI (Ables et al. 1987) and low- J CO transitions (Whiteoak et al. 1990; Dahlem et al. 1993; Ott 1995; Mauersberger et al. 1996) suggest the presence of a face-on circumnuclear molecular ring. Millimeter molecular

multiple transition studies (Wang et al. 2004; Cunningham & Whiteoak 2005) are consistent with this result. The bright infrared and radio emission in the nucleus (Ghosh et al. 1992), and the evidence that large amounts of gas seem to coexist in the central $30''$ (Henkel et al. 1994) make it particularly suited for studying the high density environment in the center of this galaxy.

4.1.2 Circinus

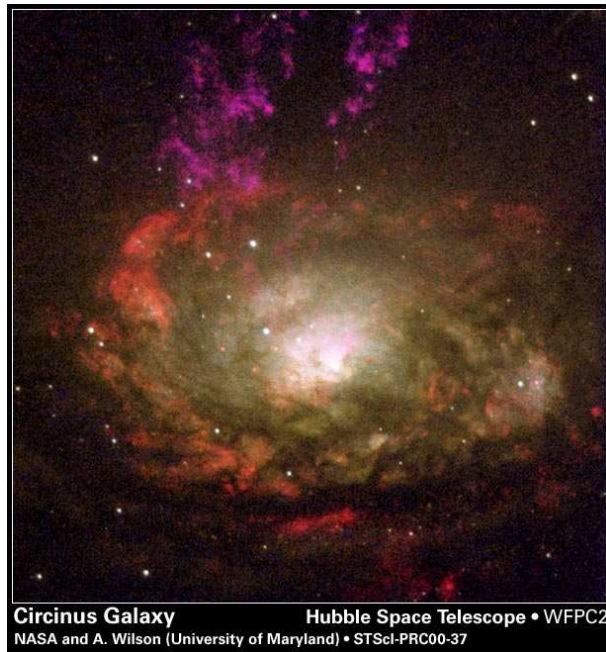


Figure 4.2: HST composite image of the spiral galaxy Circinus.

The nearby starburst spiral Circinus has a small optical angular diameter of $\sim 7'$ compared to its hydrogen diameter $D_{\text{H}} = 36'$ defined by the $1 \times 10^{20} \text{ atoms cm}^{-2}$ contour in Freeman et al. (1977).

Circinus has a dynamical mass of $\sim 3 \times 10^9 M_{\odot}$ within the inner 560 pc (Curran et al. 1998) matching the value obtained for NGC 4945. Large amounts of molecular gas have been found by studies of low- J CO observations (Johansson et al. 1991; Aalto et al. 1995; Elmouttie et al. 1998; Curran et al.

1998) including $C^{17}O$, $C^{18}O$ and HCN (Curran et al. 2001). The strong H_2O maser emission found (Gardner & Whiteoak 1982) trace a thin accretion disk of 0.8 pc radius, with a significant population of masers lying away from this disk, possibly in an outflow (Greenhill et al. 1998). Its obscured nucleus is classified as X-ray Compton thick Seyfert 2. It shows a circumnuclear star burst on scales of 100 - 200 pc (Maiolino et al. 1998) with complex structure of H II as seen in HST $H\alpha$ images (Wilson et al. 2000). Adaptive optics studies find there has been a recent star burst (~ 100 Myr old) in the central 8 pc accounting for 2% of the total luminosity (Mueller Sánchez et al. 2006). The strong FIR emission, the large molecular gas reservoir, the existence of a molecular ring associated with star burst activity (Curran et al. 1998) and the similarity with NGC 4945 make Circinus and the former ideal objects for comparative studies of the dense and warm ISM in their nuclei.

4.1.3 The importance of submm lines in NGC4945 and Circinus

Both NGC4945 and Circinus show a strong central star burst activity which is fed by large amounts of molecular material which has been studied extensively at millimeter wavelengths (e.g. Curran et al. 2001; Wang et al. 2004). Sub-millimeter observations are largely missing. The important rotational transitions of CO with $J \geq 4$ and the fine structure transitions of atomic carbon have not yet been observed. These transitions often contribute significantly to the thermal budget of the interstellar gas in galactic nuclei and are therefore important tracers of the physical conditions of the warm and dense gas. We motivated the importance of submm-observations and in particular of CO and [C I] in chapter 1. The CO 4–3 transition in particular is a sensitive diagnostic of the dense and warm gas while the CO 1–0 transition traces the total molecular mass.

Heating mechanisms The strong cooling emission is balanced by equally strong heating caused by the vigorous star formation activity in the galaxy centers. The variation of CO cooling intensities with rotational number, i.e. the peak of the CO cooling curve, reflects the star forming

activity (Bayet et al. 2006) and, possibly, also the underlying heating mechanisms. Several mechanisms have been proposed to explain the heating of the ISM in galactic nuclei and it is currently rather unclear which of these is dominating in individual sources (e.g. Wang et al. 2004). Heating by X-rays from the active galactic nuclei (AGN) may lead to strongly enhanced intensities of high- J CO transitions (Meijerink et al. 2007), possibly allowing to discriminate this heating mechanism from e.g. stellar ultraviolet heating via PDRs (e.g. Bayet et al. 2006). The greatly enhanced supernova rate by several orders of magnitude relative to the solar system value leads to an enhanced cosmic ray flux, providing another source of gas heating in the centers (Faruhar et al. 1994; Bradford et al. 2003).

Another mechanism for heating is provided by shocks. The most important, large-scale shocks, are produced by density wave instabilities which induce gravitational torques (in spiral arms and/or bars) and make the gas fall into the nucleus (Usero et al. 2006). A non-negligible contribution is also given by shocks produced by supernovae explosions. On smaller scales, bipolar outflows from young stellar objects (YSO) can also contribute to this heating although to a lesser extent (e.g. García-Burillo et al. 2001).

4.2 Observations with the NANTEN2 telescope



Figure 4.3: *The NANTEN2 sub-millimeter telescope at Pampa la Bola, Chile. Picture taken by R.Simon.*

The NANTEN2 sub-millimeter telescope (e.g. Simon et al. 2007; Kramer et al. 2007) on Pampa la Bola at an elevation of 4900m together with a dual channel 490/810 GHz receiver was used to observe the centers of NGC 4945 and Circinus (Table.4.1) in CO 4–3 and [C I] 1–0. This telescope is operated jointly by the Nagoya University radioastronomy group, the KOSMA group from Universität zu Köln, the University of Bonn and other contributing partners from Chile, Australia and Korea.

The observations were done from September to October 2006 using position-switch mode with 20 sec On- and 20 sec Off-time. In October 2007 we re-observed ^{12}CO 4–3 in the centers of NGC4945 and Circinus with the newly available chopping tertiary in double beam-switch mode yielding significantly improved baselines and removing atmospheric features in the spectra. In NGC 4945 the total integration times ON-source are 17 min and 10 min for ^{12}CO 4–3 and [C I] 1–0 respectively and in Circinus integration times ON-source are 10 min and 34 min for ^{12}CO 4–3 and [C I] 1–0 respectively at source elevations of 40-60°. The relative calibration uncertainty derived from repeated pointings on the nuclei is about 15%.

Observation mode and telescope characteristics Position-switching was conducted by moving the telescope 10' in azimuth, i.e. out of the galaxy. Using double beam-switch (dbs) mode, the chopper throw is fixed at 162'' in azimuth with a chopping frequency of 1 Hz. Typical double-sideband receiver temperatures of the dual-channel 460/810 GHz receiver were ~ 250 K at 460 GHz and 492 GHz. The system temperature varied between ~ 850 and ~ 1200 K. As backends we used two acousto optical spectrometers (AOS) with a bandwidth of 1 GHz and a channel resolution of 0.37 km s^{-1} at 460 GHz and 0.21 km s^{-1} at 806 GHz. The pointing was regularly checked and pointing accuracy was stable with corrections of $\sim 10''$. The *half power beam width* (HPBW) at 460 GHz and 492 GHz is 38'' with a beam efficiency $B_{\text{eff}} = 0.50$ and a forward efficiency $F_{\text{eff}} = 0.86$ (Simon et al. 2007). The calibrated data on T_A^* -scale were converted to T_{mb} by multiplying with the ratio $F_{\text{eff}}/B_{\text{eff}}$. The standard calibration procedure derives the atmospheric transmission (averaged over the bandpass) from the observed difference spectrum of hot load and blank sky, the latter taken at a reference position. Next, the model atmosphere `atm` is used to derive the atmospheric opacity taking into account the sideband imbalance. This is an important correction, especially when observing the CO 4-3 and [CI] 1-0 lines. This pipeline produces the standard spectra on the antenna temperature scale (T_A^*). In addition, we removed baselines up to first order.

The 810 GHz channel was not used for these observations due to insufficient baseline stability. All data presented subsequently are on the T_{mb} scale. Next, we will present the spectra of CO 4–3 and [C I] 1–0 in NGC4945 and

Circinus and present complementary data, needed for the radiative transfer modeling.

4.2.1 Spectra of CO 4–3 and [C I] 1–0

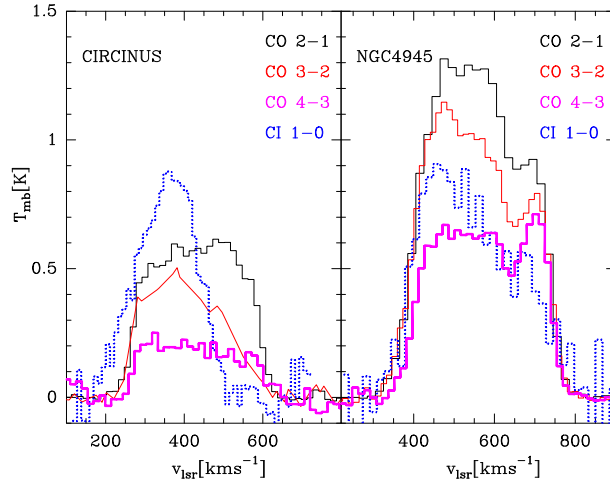


Figure 4.4: CO 4–3 and [C I] 1–0 spectra of Circinus and NGC 4945 obtained with the NANTEN2 telescope together with low- J CO observations by Curran et al. (2001, 1998); Mauersberger et al. (1996). All data are at $38''$ resolution, only the CO 3–2 spectrum of Circinus is at $15''$ resolution. The small amount of excess emission in the blue wing of the [C I] 1–0 line in Circinus maybe caused by small pointing variations in the eastern direction as emission in lower- J CO lines extends to this region and velocities (Curran et al. 1998).

Fig. 4.4 shows the ^{12}CO 4–3 and [C I] 1–0 spectra of NGC 4945 and Circinus obtained with the NANTEN2 telescope. CO 4–3 spectra peak at 700 mK in NGC 4945 and 250 mK in Circinus. Outside the velocity ranges of 350–800 kms^{-1} and 200–600 kms^{-1} respectively, the baseline rms values are 11 mK and 25 mK, respectively, at the velocity resolution of 15 kms^{-1} .

[C I] 1–0 spectra peak at 900 mK in both galaxies while the rms values are 110 mK and 140 mK, respectively. The [C I] 1–0 area-integrated luminosities are 91 $\text{Kkms}^{-1}\text{kpc}^2$ and 67 $\text{Kkms}^{-1}\text{kpc}^2$ in NGC4945 and Circinus.

Curran et al. (2001, 1998) and Mauersberger et al. (1996) mapped the low- J 2–1, and 3–2 transitions of CO in the centers of both galaxies with SEST. We smoothed these data to the resolution of the NANTEN2 data, i.e. to 38". Only the ^{12}CO 3–2 spectrum in Circinus is shown at its original resolution of 15" because a map of the central region could not be retrieved. Calibration of the CO 3–2 spectrum in NGC 4945 was confirmed recently at APEX (Risacher et al. 2006). The ^{12}CO 1–0, ^{13}CO 1–0 and ^{13}CO 2–1 spectra of the central region of NGC 4945 and Circinus are presented in Curran et al. (2001). Integrated intensities are given in Table 4.2.

Table 4.2: Observed line intensities in Circinus and NGC 4945. Calibration uncertainties are estimated to be 15%. The spectra in Fig. 4.4 and the integrated intensities correspond to the listed angular resolution (FWHM). References: ^a Curran et al. (2001), ^b Mauersberger et al. (1996).

line transition	Circinus		NGC 4945
	I_{int} [Kkms ⁻¹]	I_{int} [Kkms ⁻¹]	FWHM ["]
CO 1–0 ^a	180	510	45
CO 2–1 ^a	177	390	38
CO 3–2 ^b	-	330	38
CO 3–2 ^b	230	-	15
CO 4–3	58	212	38
^{13}CO 1–0 ^a	12	30	45
^{13}CO 2–1 ^a	19	45	38
[C I] 1–0	163	248	38

NGC 4945 shows broad emission between 350 and 800 kms⁻¹. The CO 4–3 line shape resembles the line shapes of 1–0 and 2–1. The line shape of [C I] 1–0 is similar to that of the CO transitions with a slightly higher peak temperature than CO 4–3.

In CO 1–0 and 2–1, Circinus shows broad emission between 200 and about 600 kms⁻¹. The velocity component at ~ 550 kms⁻¹ becomes weaker with rising rotational number. Emission of [C I] 1–0 is restricted to 200 and ~ 500 kms⁻¹ only. In Circinus, the [C I] peak temperature is a factor ~ 3 stronger than CO 4–3.

In the next section we estimate the CO and [C I] column densities from the integrated intensities in LTE approximation and using an Galactic X-factor. After that more sophisticated radiative transfer calculations in the escape probability approximation are used to determine the physical conditions.

4.3 Physical conditions

LTE In the optically thin limit, the integrated intensities of [C I] and ^{13}CO listed in Table 4.2 are proportional to the total column densities. Local thermal equilibrium (LTE) column densities of carbon are rather independent of the assumed excitation temperatures (e.g. Frerking et al. 1989). We find $N_{\text{C}} = 3.4 - 3.9 \cdot 10^{18} \text{cm}^{-2}$ in NGC 4945 and $N_{\text{C}} = 2.2 - 2.5 \cdot 10^{18} \text{cm}^{-2}$ in Circinus for a temperature range of $T_{\text{ex}} = 20 - 150 \text{K}$.

We used the ^{13}CO $J=1-0$ and $J=2-1$ integrated intensities to derive total CO column densities, assuming LTE, optically thin ^{13}CO emission, a CO/ ^{13}CO abundance ratio of 40 (Curran et al. 2001), and $T_{\text{ex}} = 20 \text{K}$. We find a total CO column density of $N_{\text{CO}} = 1.0 - 1.7 \cdot 10^{18} \text{cm}^{-2}$ and $N_{\text{CO}} = 4.1 - 6.7 \cdot 10^{17} \text{cm}^{-2}$ in NGC 4945 and Circinus respectively depending on which transition is used, 1-0 or 2-1. Varying the temperature to $T_{\text{ex}} = 150 \text{K}$ the column density of CO slightly increases up to $N_{\text{CO}} = 3.2 \cdot 10^{18} \text{cm}^{-2}$ and $N_{\text{CO}} = 1.4 \cdot 10^{18} \text{cm}^{-2}$ for NGC 4945 and Circinus.

X-factor method Another method is using the Galactic CO 1-0 to H_2 conversion factor $X_{\text{MW}} = 2.3 \cdot 10^{20} \text{cm}^{-2} (\text{K km s}^{-1})^{-1}$ (Strong et al. 1988; Strong & Mattox 1996) and the canonical CO to H_2 abundance of $8.5 \cdot 10^{-5}$ (Frerking et al. 1982) to derive $N_{\text{CO}} = 3.5 \cdot 10^{18} \text{cm}^{-2}$ for Circinus, i.e. a factor of ~ 10 larger than the LTE estimate indicating that the X-factor is only 1/10 Galactic. As the abundance of CO maybe different in NGC 4945 and Circinus this result has to be taken with caution.

For NGC 4945 Wang et al. (2004) derive an X-factor 7 times smaller than the Galactic which leads to $N_{\text{CO}} = 1.4 \cdot 10^{18} \text{cm}^{-2}$ in good agreement with the LTE approximation from ^{13}CO . The LTE column density derived from

^{13}CO in Circinus also indicates an X-factor which is around 10 times smaller than the Galactic value.

The CO/C abundance ratio is 0.29-0.50 in NGC 4945 and 0.19-0.27 in Circinus using the LTE column densities.

4.3.1 Escape probability calculations using CO and ^{13}CO

We modeled the ^{12}CO and ^{13}CO emission lines using an escape probability radiative transfer model for spherical clumps. The radiative and collisional excitation mechanisms, all relevant quantities and the escape probability approximation were introduced in chapter 2. For the modeling we use the escape probability code by Stutzki & Winnewisser (1985).

Model input Input parameters in the model are the CO collision rates of Schinke et al. (1985), energy levels of the transitions and Einstein A-values. The physical parameters kinetic temperature T_{kin} , molecular density $n(\text{H}_2)$, and column density N_{CO} determine the excitation conditions in this non-LTE model (Table 4.3).

In NGC 4945 and Circinus, we used the ratios of the observed integrated intensities of CO 1–0 to 4–3 and the ^{13}CO 1–0 and 2–1 transitions (Curran et al. 2001) to obtain column densities, density and kinetic temperature, assuming a constant $^{12}\text{CO}/^{13}\text{CO}$ abundance ratio. Using line ratios at similar resolution gives us the advantage that the beam filling factor cancels out in the ratio. We used an abundance ratio of 40 in both sources in accordance with Curran et al. (2001). The escape probability code uses an internal clump line width Δv_{mod} which is hardly effecting the outcome of the model in the reasonable range of 1-20 kms^{-1} .

A χ^2 -fitting routine then compared in a simultaneous fit the J line ratios of the model output R_{mod}^j to the ratios of the observed integrated intensities R_{obs}^j and determined the model with the minimal χ^2 . We compute the normalized χ^2 with the degrees of freedom $d = J - p$ and J being the

number of independent ratios and p the number of parameters, in our case T_{kin} , $n(\text{H}_2)$ and N_{CO} , to be determined :

$$\chi^2 = \frac{1}{d} \sum_{j=1}^J (R_{\text{mod}}^j - R_{\text{obs}}^j) / \sigma_j. \quad (4.1)$$

The errors σ_j due to calibration uncertainties are estimated to be 20%.

In Circinus the ^{12}CO 3–2 line is missing leaving one degree of freedom compared to two in NGC 4945.

T_{kin} and $n(\text{H}_2)$ are determined with this step. To compare the modeled integrated intensities I_{mod} to the absolute observed intensities I_{obs} we have to account for the velocity filling, due to the velocity width Δv_{mod} of an individual clump to the width of the galaxy spectrum Δv_{obs} and the beam dilution, due to the size of the modeled clump A_{cl} compared to the beam area A_{beam} .

Velocity filling and beam dilution The large velocity width of the observed spectra implies several clumps in the beam $N_{\text{cl}} = n \Delta v_{\text{obs}} / \Delta v_{\text{mod}}$ with $n \geq 1$ (Table 4.3). The beam dilution is determined by the fraction of modeled clump area to the beam size which we express in terms of an area filling factor per clump $\phi_{\text{A,cl}} = A_{\text{cl}} / A_{\text{beam}}$. The total area filling factor is $\phi_{\text{A}} = N_{\text{cl}} \phi_{\text{A,cl}}$. The size of the clump with radius R , $A_{\text{cl}} = \pi R^2$, can be inferred via the mass M and density $n(\text{H}_2)$ of the clump: $R = (3 / (4\pi) M / n)^{1/3}$. In summary, the modeled intensities of the individual clumps I_{mod} are converted to the intensities of a clump ensemble I_{ens} which can then be compared with the observed intensities:

$$I_{\text{ens}} = I_{\text{mod}} \times N_{\text{cl}} \times \phi_{\text{A,cl}} = I_{\text{mod}} \times \phi_{\text{A}}. \quad (4.2)$$

Table 4.3: Escape probability model results with two representative solutions for each source. N_{CO} and N_{H_2} denote the total beam averaged column density of CO and H_2 , i.e. local clump column densities weighted by the total area filling factor ϕ_{A} . M denotes the total mass. N_{cl} is the number of clumps in the beam, Δv_{mod} is the modeled velocity width and ϕ_{A} is the total filling factor to convert from modeled to observed intensities. The total cooling intensities are given in units of $10^{-5} \text{ ergs}^{-1} \text{ cm}^{-2} \text{ sr}^{-1}$.

	Circinus		NGC 4945	
χ^2	2.0	9.6	4.8	12.4
$n(\text{H}_2)_{\text{loc}} [\text{cm}^{-3}]$	10^4	10^3	$3 \cdot 10^4$	10^3
$T_{\text{kin}} [\text{K}]$	20	100	20	100
$N_{\text{CO}} [10^{16} \text{cm}^{-2}]$	35	50	76	63
$N_{\text{C}} [10^{16} \text{cm}^{-2}]$	230	30	330	98
$N_{\text{H}_2} [10^{20} \text{cm}^{-2}]$	37	46.5	89	74
$M [10^6 M_{\odot}]$	630	792	1385	1114
$\Delta v_{\text{mod}} [\text{kms}^{-1}]$	5	5	10	10
$\Delta v_{\text{obs}} [\text{kms}^{-1}]$	186	186	188	188
N_{cl}	50	38	35	40
ϕ_{A}	2.0	6.3	1.5	4.0
$^{12}\text{CO}/^{13}\text{CO}$ abundance ratio	40	40	40	40
CO/C abundance ratio	0.15	1.67	0.23	0.64
[C I] cooling intensity	4.1	7.88	7.2	11.8
CO cooling intensity	2.1	2.8	6.6	5.7
[C I] /CO cooling intensity ratio	2.0	2.8	1.1	2.1

Results in NGC 4945

Fig. 4.5b shows the observed intensities of CO, ^{13}CO , and [C I] together with two representative solutions of the radiative transfer calculations (see also Table 4.3).

CO. Fitting the CO and ^{13}CO lines, we find a degeneracy in the $n(\text{H}_2)$ - T_{kin} plane of the solutions for a rather constant pressure $n(\text{H}_2) \times T_{\text{kin}} \sim 10^5 \text{ Kcm}^{-3}$. The best fits are achieved for a $^{12}\text{CO}/^{13}\text{CO}$ abundance ratio of 40,

similar to the value found by Curran et al. (2001). Low χ^2 -values (see Table 4.3) constrain the densities to $n(\text{H}_2) = 10^3 - 10^5 \text{cm}^{-3}$ and temperatures to a wide range of $T_{\text{kin}}=20\text{-}180$ K with higher temperature solutions corresponding to lower densities. The best fitting solution is $n(\text{H}_2) = 3 \cdot 10^4 \text{cm}^{-3}$ and $T_{\text{kin}}=20$ K. However, this solution is not significantly better than e.g. $n(\text{H}_2) = 10^3 \text{cm}^{-3}$ and $T_{\text{kin}}=100$ K (Fig. 4.5b, Table 4.3).

The fitted column density N_{CO} agrees with the LTE approximation for the CO-column density within a factor of 2–3.

The peak of the modeled CO cooling curve at $J=4$ contains 35.6% of the total ^{12}CO cooling intensity of $6.6 \cdot 10^{-5} \text{ergs}^{-1} \text{cm}^{-2} \text{sr}^{-1}$ computed by summing of the cooling intensity of the ^{12}CO transitions from $J=1$ to 20 for the $T_{\text{kin}}=20$ K solution.

We use the radiative transfer model to predict the ^{12}CO 7–6 intensity. It is rather weak, depending strongly on T_{kin} . It varies from 1.3Kkms^{-1} for the $T_{\text{kin}}=20$ K solution to 4.1Kkms^{-1} for the $T_{\text{kin}}=100$ K fit.

Curran et al. (2001) find in this source $n(\text{H}_2)=3 \times 10^3 \text{cm}^{-3}$ and $T_{\text{kin}}=100$ K from ^{12}CO observations of the 3 lowest transitions and ^{13}CO data of the two lowest transitions. In their multi-transition study Wang et al. (2004) estimate a density of $n(\text{H}_2)=10^3 \text{cm}^{-3}$ for an assumed temperature $T_{\text{kin}}=50$ K from CO transitions up to $J = 3$. In contrast, the observed CN and CH_3OH lines indicate local densities around 10^4cm^{-3} . The solutions for CO and ^{13}CO found in the literature are in good agreement with our parameter space of solutions showing that the additional CO 4–3 line does not help significantly to improve on the fits.

Atomic carbon. Assuming the same density, kinetic temperature, velocity filling, and beam dilution for Carbon as for CO, we use the observed [C I] intensity and the radiative transfer model to estimate the carbon column density and hence the CO/C abundance ratio. The CO/C abundance ratio varies between 0.23 and 0.64 for the two solutions listed in Table 4.3. The corresponding carbon column densities are $N_{\text{C}} = 3.3 \cdot 10^{18} \text{cm}^{-2}$ and $N_{\text{C}} = 9.8 \cdot 10^{17} \text{cm}^{-2}$ for the high and the low density solution, respectively. The column density for the latter solution is a factor of 3 lower compared to

the LTE carbon column density. The assumption of optically thin emission in the LTE might be overestimating the column density compared to the escape probability modeling. We also use the model to predict the [C I] 2–1 intensity. It is 16 Kkms^{-1} for the $T_{\text{kin}}=20 \text{ K}/n(\text{H}_2) = 3 \cdot 10^4 \text{ cm}^{-3}$ solution. However, this result is critically depending on the kinetic temperature. The $T_{\text{kin}}=100 \text{ K}/n(\text{H}_2) = 10^3 \text{ cm}^{-3}$ solution yields 182 Kkms^{-1} . Also, the [C I] 2–1/[C I] 1–0 line ratios change from 0.07 to 0.75, depending on the solution. This shows that the high lying transitions can be used to break the degeneracy. The total cooling intensity of both [C I] lines is listed in Table 4.3 for both presented solutions. The cooling intensity of the two [C I] lines is thus of the order of the total cooling intensity of CO with the C/CO cooling intensity ratio varying between 1.1-2.1 for the discussed solutions.

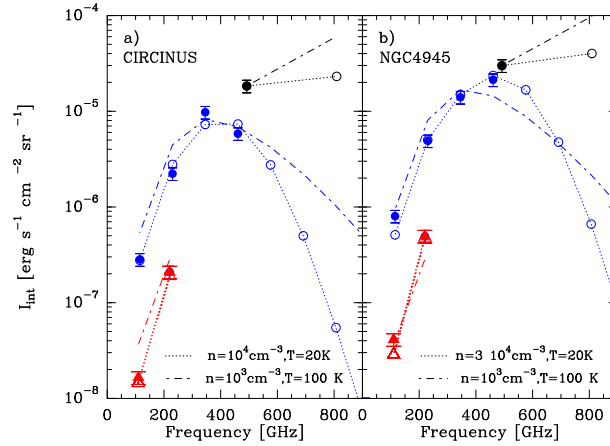


Figure 4.5: Radiative transfer modeling results and observations: Filled blue points show the observed CO and blue circles the modeled CO. The dotted line indicates the best fit solution. Filled red triangles show the observed ^{13}CO and red triangles the modeled ^{13}CO . Dash-dotted lines show a higher temperature solution. Filled black points are the observed [C I] integrated intensities and black circles the predicted [C I] integrated intensities.

Results in Circinus

CO. The modeled CO cooling curves are shown in Fig. 4.5a and the fit results are summarized in Table 4.3. The CO line ratios are given for a $\Delta v_{\text{mod}}=5 \text{ kms}^{-1}$ so there are about 40 clouds in the beam to account for

the observed velocity width of $\Delta v_{obs}=186\text{kms}^{-1}$. The assumed $^{12}\text{CO}/^{13}\text{CO}$ abundance ratio of 40 is slightly lower than the values of ~ 60 , found by Curran et al. (2001).

Good fits corresponding to low χ^2 (see Table 4.3) can be found for densities of $n(\text{H}_2) = 10^3 - 10^{4.5}\text{cm}^{-3}$ and a large range of temperatures of $T_{kin}=20\text{-}160$ K while the product of $n(\text{H}_2) \times T_{kin}$ stays approximately constant at $\sim 10^5\text{Kcm}^{-3}$. Again, a number of solutions provide consistent CO cooling curves.

The lowest χ^2 is obtained for $n(\text{H}_2) = 10^4\text{cm}^{-3}$, $T_{kin}=20$ K and a column density of $N_{CO} = 3.5 \cdot 10^{17}\text{cm}^{-2}$ assuming 50 modeled clumps in the beam. The column density N_{CO} is well determined showing a steep gradient of χ^2 -values for varying densities and temperatures. This is in reasonable agreement with the LTE-approximation from ^{13}CO . A second solution at $n = 10^3\text{cm}^{-3}$ and $T_{kin}=100$ K also lies within the 1σ -contour of the χ^2 distribution (cf. Fig. 4.5 and Tab.4.3).

The results agree well with the solutions found by Curran et al. (2001). They find $T_{kin}=50\text{-}80$ K and $n(\text{H}_2) = 2 \cdot 10^3\text{cm}^{-3}$ from observations of the 3 lowest ^{12}CO transitions and the 2 lowest ^{13}CO transitions.

The modeled CO cooling curve peaks at $J=4$ containing 35% of the total ^{12}CO cooling intensity of $2.1 \cdot 10^{-5} \text{ ergs}^{-1}\text{cm}^{-2}\text{sr}^{-1}$ for the $T_{kin}=20$ K fit.

The predicted integrated intensity of ^{12}CO 7–6 is very weak, varying strongly from 0.1 Kkms^{-1} for the $T_{kin}=20$ K solution to 1.9 Kkms^{-1} for $T_{kin} = 100$ K.

Atomic carbon. Assuming the same density and temperature for carbon as for CO, we use the best fitting CO model to derive the [C I] 1–0 intensity, carbon column densities, and CO/C abundance ratios. The predicted CO/C abundance ratio is 0.15, again consistent with the optically thin LTE result. The predicted [C I] 2–1 integrated intensity is 6.1 Kkms^{-1} .

As in NGC 4945, changing the temperature has a big effect on the [C I] 2–1 intensity. The $T_{kin}=100$ K solution yields 111 Kkms^{-1} and a higher CO/C

abundance ratio of 1.67. Thus the $[\text{C I}]2-1/[\text{C I}]1-0$ line ratios changes from 0.04 to 0.74.

The corresponding carbon column densities for the two presented solutions are $N_{\text{C}} = 2.3 \cdot 10^{18} \text{cm}^{-2}$ and $N_{\text{C}} = 3.0 \cdot 10^{17} \text{cm}^{-2}$, respectively. For the latter solution the column density is about a factor of 10 lower compared to the LTE carbon column density. The optically thin assumption for the LTE modeling is obviously not working in the high temperature and low density scenario.

The total cooling intensity ratio of $[\text{C I}] / \text{CO}$ is varying from 2.1 to 2.8 for the presented solutions. Carbon is a stronger coolant than CO by a factor of 2-3.

Next, we will discuss the results obtained from observations and radiative transfer modeling in the context of previous extragalactic investigations. First, the purely observationally determined quantities like $[\text{C I}]$ luminosity, $[\text{C I}] 1-0/\text{CO} 4-3$ and $[\text{C I}] 1-0/^{13}\text{CO} 2-1$ line ratios are compared to previous extragalactic observations. Subsequently, results based on the radiative transfer calculations like abundance ratios and total cooling power are discussed.

4.4 Summary and discussion

$[\text{C I}] 1-0$ luminosities

The $[\text{C I}] 1-0$ luminosities for the centers of the Seyfert galaxies NGC 4945 and Circinus are 91 and 67 $\text{K km s}^{-1} \text{kpc}^2$ (Fig. 4.6). To date, about 30 galactic nuclei have been studied in the 1-0 line of atomic carbon, most of which are presented in Gerin & Phillips (2000) and Israel & Baas (2002). The $[\text{C I}]$ luminosity of a source is an important property since it gives the amount of energy emitted per time which is proportional to the number of emitting atoms, i.e. proportional to the $[\text{C I}]$ column density in the limit of optically thin emission. The NANTEN2 $38''$ beam achieves ~ 700 pc resolution in

Circinus and NGC 4945 which both lie at ~ 4 Mpc. To achieve the same spatial resolution for galaxies at ~ 12 Mpc distance, e.g. for NGC 278, NGC 660, NGC 1068, NGC 3079 and NGC 7331 listed in Israel & Baas (2002), one would need an angular resolution of $\sim 13''$, comparable to the $10''$ JCMT beam at 492 GHz. The luminosities studied in these 7 sources do thus all sample the innermost ~ 700 pc. Area integrated [C I] luminosities are found to vary strongly between ~ 1 and $\sim 160 \text{ Kkms}^{-1} \text{ kpc}^2$ in these 7 galaxies (Fig. 4.6) (Israel 2005; Israel & Baas 2002). Quiescent centers show modest luminosities $1 \leq L([\text{C I}]) \leq 5 \text{ Kkms}^{-1} \text{ kpc}^2$, while starburst nuclei in general show higher luminosities. The largest luminosities are found in the active nuclei of NGC 1068 and NGC 3079 which show 50 and $160 \text{ Kkms}^{-1} \text{ kpc}^2$ (Israel & Baas 2002). NGC4945 and Circinus also fall in this category (Fig. 4.6).

[C I] 1–0/CO 4–3 line ratios

The [C I] 1–0/CO 4–3 ratio of integrated intensities is 1.2 in NGC 4945 and 2.8 in Circinus. For Circinus the ratio is larger than any ratios previously observed in other galactic nuclei or in the Milky Way. The [C I]1–0/CO 4–3 ratio is shown in Fig. 4.6) versus the area integrated [C I] luminosity. As also discussed in Israel & Baas (2002), we see no functional dependence. Galactic sources (not shown in this figure) would be lying in the lower left corner. Israel (2005) studies 13 galactic nuclei and finds that the [C I] 1–0 line is in general weaker than the CO 4–3 line, but not by much. Ratios vary over one order of magnitude between 0.1 in Maffei2 and 1.2 NGC 4826. Galactic star forming regions like W3 Main or the Carina clouds show much lower values, between about 0.1 and 0.5, which are consistent with emission from PDRs (Kramer et al. 2004; Jakob et al. 2007; Kramer et al. 2007). Fixsen et al. (1999) find 0.22 in the Galactic center and 0.31 in the Inner Galaxy. The variation seen in the various Galactic and extragalactic sources appears to be intrinsic and not due to observations of different angular resolutions. This is because the frequencies of the two lines are very close and angular resolutions are therefore similar if the same telescope is used.

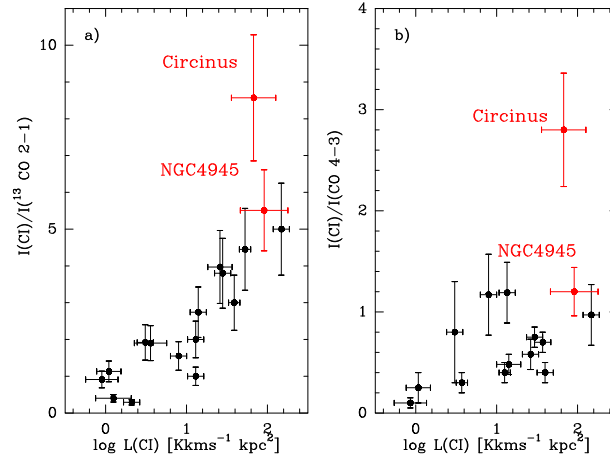


Figure 4.6: a) $[\text{C I}]1-0/^{13}\text{CO } 2-1$ ratios versus $L([\text{C I}])$. b) $[\text{C I}]1-0/\text{CO } 4-3$ ratios versus $L([\text{C I}])$. Black points are the results from Israel & Baas (2002) and red points are the ratios from this thesis.

$[\text{C I}] 1-0/^{13}\text{CO } 2-1$ line ratios

The $[\text{C I}] 1-0/^{13}\text{CO } 2-1$ line ratios in NGC 4945 and Circinus are 5.51 and 8.57, respectively (Fig. 4.6). In NGC 4945, the observed ratio is consistent with results found in previous studies (Israel & Baas 2002; Gerin & Phillips 2000) ranging up to ratios of 5. For Circinus, the ratio is again higher than any previous measurement.

Two thirds of the sample of galaxies studied by Israel & Baas (2002) show $[\text{C I}] 1-0/^{13}\text{CO } 2-1$ line ratios well above unity. The sample consists of quiescent, star burst and active nuclei. The highest $[\text{C I}] 1-0/^{13}\text{CO } 2-1$ ratios are found in star burst and active nuclei consistent with our observations. Gerin & Phillips (2000) find a similar result with two thirds of the galaxies in their sample exceeding a ratio of 2. High ratios can be qualitatively understood in low column density environments with mild UV radiation fields. In these regimes most CO will be dissociated and the gas-phase carbon will be neutral atomic (Israel & Baas 2002). This implies that dense, star forming molecular cloud cores are not the major emission source in galaxy centers.

In general the studied centers of external galaxies show stronger $[\text{C I}]$ emis-

sion than one would expect from Galactic observations which show typical ratios of 0.2-1.1 (Mookerjea et al. 2006). In Galactic sources high ratios are found in low gas column densities and medium UV radiation environments where ^{13}CO will be dissociated and atomic carbon remains neutral in the gas phase like i.e. in translucent clouds and at cloud edges (Israel 2005). He concludes that the dominant emission from galaxy centers does not stem from PDRs.

Meijerink et al. (2007) studied irradiated dense gas in galaxy nuclei using a grid of XDR¹ and PDR-models. For the same density the predicted [C I] 1-0/ ^{13}CO 2-1 line ratios are significantly higher for the XDR- compared to PDR-models (Fig. 10 in Meijerink et al. 2007). We observed ratios of 61 and 95 in NGC4945 and Circinus respectively, on the erg-scale. These ratios can be explained by XDR-models at high densities $n(\text{H}_2) = 2 \cdot 10^3 - 10^5 \text{cm}^{-3}$. PDR-models explain the observed ratios in low density regimes with $n(\text{H}_2) = 2 \cdot 10^2 - 6 \cdot 10^2 \text{cm}^{-3}$. The high [C I] 1-0/ ^{13}CO 2-1 line ratios observed in NGC 4945 and Circinus may hint at a significant role of X-ray heating in these galaxy nuclei as our predicted densities of $n(\text{H}_2) = 10^3 - 10^4 \text{cm}^{-3}$ agree with the high-density XDR-models in Meijerink et al. (2007).

Total CO and [C I] cooling intensity

In all sources studied by Bayet et al. (2006) but NGC 6946, the CO cooling intensity exceeds that of atomic carbon. They find the [C I] to CO cooling ratio to vary between ~ 0.3 for M83 to ~ 2 for NGC 6946. NGC 4945 and Circinus show similarly high values as the latter galaxy: In NGC 4945 this, ratio is $\sim 1 - 2$ and in Circinus we find $\sim 2 - 3$. These values are around 2 orders of magnitude higher than the typical values found in Galactic star forming regions (Jakob et al. 2007; Kramer et al. 2007).

¹X-ray dominated regions

Shape of the CO cooling curve

The modeled CO cooling curve of NGC 4945 and Circinus peaks at $J = 4$. Observations of the higher lying CO lines i.e. the CO 6-5 and CO 7-6 lines will however be important to verify our model predictions and the importance of CO cooling relative to C.

The shape and maximum of the cooling curve of ^{12}CO has been studied in a number of nearby and high- z galaxies. Fixsen et al. (1999) find a peak at $J=5$ in the central part of the Milky Way using FIRAS/COBE data and rotational transitions upto 8–7. Bayet et al. (2006) observed 13 nuclei in mid- J CO lines upto 7–6 and find that the peak of the cooling curves vary with nuclear activity. While normal nuclei exhibit peaks near $J_{\text{up}} = 4$ or 5, active nuclei show a peak near $J_{\text{up}} = 6$ or 7. NGC 253 was observed at APEX in CO upto $J_{\text{up}} = 7$ and shows a maximum at $J = 6$ (Güsten et al. 2006). On the other hand, studies of high redshift galaxies show cooling curves peaking as low as $J=4$ for SMM 16359 (Weiß et al. 2005), as high as $J=9$ in the case of the QSO APM 08279 (Weiss et al. 2007), and peaking at $J=7$ for the very high redshift ($z = 6.4$) QSO J1148 (Walter et al. 2003).

Pressure of the molecular gas

A wide range of temperatures $T_{\text{kin}} = 25 - 150$ K and densities $n(\text{H}_2) = 5 \cdot 10^2 - 7 \cdot 10^5 \text{cm}^{-3}$ has been found in similar studies of external nuclei, including ULIRGs², normal spirals, star burst galaxies, and interacting galaxies (e.g. Bayet et al. 2006; Israel & Baas 2002). In the irregular galaxy IC 10 rather high densities $n(\text{H}_2) \sim 10^6 \text{cm}^{-3}$ and low temperatures of $T_{\text{kin}} = 25$ K are found while the molecular gas in the center of the spiral galaxy NGC 6946 is found to be less dense $n(\text{H}_2) = 10^3 \text{cm}^{-3}$ but much hotter $T_{\text{kin}} = 130$ K. Güsten et al. (2006) studied NGC 253 to obtain $n(\text{H}_2) = 10^{3.9} \text{cm}^{-3}$ and $T_{\text{kin}} = 60$ K while Bradford et al. (2003) investigated the same source and derived a higher $T_{\text{kin}} = 120$ K and density $n(\text{H}_2) = 4.5 \cdot 10^4 \text{cm}^{-3}$. Both studies used ^{12}CO 7–6 observations. However, the temperature/density degeneracy cannot be resolved. The solutions we

²Ultra-Luminous Infrared Galaxy

present in our study of NGC 4945 and Circinus show densities and temperatures of $n(\text{H}_2) = 10^3 - 10^4 \text{cm}^{-3}$ with a less well constrained temperature $T_{\text{kin}} = 20 - 100 \text{K}$ depending on the density, as discussed before.

[C I] 2–1/1–0 line ratio

The modeled [C I] 2–1/1–0 line ratios change from 0.07 to 0.75 in NGC 4945 and from 0.04 to 0.74 in Circinus for the presented escape probability solutions. Observed ratios vary from 0.48 in G333.0-0.4 (Tieftrunk et al. 2001) to 2.9 in W3 main for galactic and extragalactic sources (Kramer et al. 2004). For M82, Stutzki et al. (1998) found a ratio of 0.96. Bayet et al. (2006) observed ratios ranging between 1.2 (in NGC 253) to 3.2 (in IC 342). The [C I] 2–1/1–0 line ratio for the low temperature solution predicted for NGC4945 and Circinus is significantly lower than previous results in the literature.

CO/C abundance ratio

Compared to an abundance ratio CO/C of 3-5 in NGC 253 (Bayet et al. 2004) and an average value of 2 in the nucleus of M83 (White et al. 1994; Israel & Baas 2002), NGC 4945 and Circinus have a higher fraction of atomic carbon in their nuclei which resembles the low CO/C abundance ratios found in Galactic translucent clouds. We find values of 0.23-0.64 in NGC 4945 and 0.15-1.67 in Circinus. Due to the degeneracy of $n(\text{H}_2)$, T the abundance ratios cannot be determined more accurately. In galactic molecular clouds values range between 0.16-100, low values are found in translucent clouds (Stark & Dishoeck 1994) while massive star forming regions show high CO/C abundances (Mookerjea et al. 2006).

Future observations of CO 7–6 and [C I] 2–1 will be important to get a better handle on the the kinetic temperature and density to resolve their degeneracy, also for an understanding of the dominating heating mechanism i.e. X-ray or UV heating.

In the next chapter, we will give an outlook on future observational facilities and why they might help to improve the recent understanding of star formation and the related mechanisms.

Chapter 5

Outlook



Figure 5.1: The future CCAT observatory - KOSMA is a partner in this collaborative effort lead by Cornell University and CalTech. The location will be Cerro Chajnantor, Chile (altitude 5.600 m).

We found in the stability analysis of M51, using a combined stellar and gaseous Q -parameter, a value near the threshold of gravitational stability $Q_{\text{total}} = 1$ over large regions of the galactic disk of M51. Especially spiral arm regions showed a value closer to the threshold compared with interarm regions. A similar study in the LMC (Yang et al. 2007) also found the galactic disk of the LMC near the threshold for gravitational collapse which indicates possible self-regulation in galactic disks.

In the future, it will be interesting to investigate these processes in a bigger

sample of nearby galaxies. Recently, high-resolution complete H I -maps e.g. by the THINGS H I survey of a sample of 34 galaxies and LVHIS¹, covering all nearby galaxies, were obtained or are close to completion. The necessity of complete CO single-dish or interferometer maps of nearby galaxies tracing the molecular component is at the moment met by new observing campaigns e.g. at the IRAM-30m telescope lead by Walter, Leroy et al. Thus, it will soon be possible to investigate the gravitational stability and its link to star formation in different galaxy environments in a larger sample.

The spatial resolution of the IRAM-30m ¹²CO 2–1 corresponds to about 500 pc in M51 and limits us to study agglomerations of several molecular clouds in the beam. Current state of the art interferometers in their most extended configuration, like the PdB-IRAM interferometer (angular resolution 1.5'' at 230 GHz), Carma (0.2'' at 230 GHz) and the SMA (1'' at 230 GHz), can achieve a factor of about 10 better angular resolutions.

Future high resolution facilities will significantly improve on this situation. The foremost, ALMA with angular resolutions of 0.01'' at 275 GHz in the most extended configuration, will improve on the current facilities. ALMA will exhibit a collective area of about 7000 m² and a frequency coverage of 31-950 GHz (*www.eso.org*). ALMA will extend similar analysis as today is done in nearby galaxies upto redshifts of $z = 1-2$. An angular resolution of 0.1'' corresponds to 870 pc at $z=1$ ($D= 1800$ Mpc).

In nearby galaxies with a distance of 5-10 Mpc, 0.1'' correspond to less than 5 pc spatial resolution which allows future high-resolution investigations of e.g. the Schmidt law. ALMA offers the possibility to resolve individual GMCs in these sources, determine their virial masses, and to subsequently check the CO-H₂ conversion factor X . This analysis, performed in a big sample of nearby galaxies, will improve the understanding of the dependence of the X -factor on galactic environment such as e.g. the metallicity. Thus, uncertainties in the current understanding of star formation laws can be reduced.

Additionally, it will be possible to check the gravitational stability of different areas of a galactic disk in spiral arm and interarm regions at high

¹The Local Volume H I Survey



Figure 5.2: *SOFIA observatory - KOSMA is contributing to the GREAT receiver aboard SOFIA.*

angular resolution. The details of how stars form from the gravitational collapse of molecular clouds might then be better understood and a comprehensive overview of an entire galaxy can be obtained.

We saw in the analysis of the central regions of NGC4945 and Circinus that low to mid- J CO and the [C I] 1–0 lines are not sufficient to unambiguously determine the physical conditions in these regions. With the SMART-array receiver operational from mid-2008 at the NANTEN2 telescope, CHAMP+² at the APEX telescope and the future CCAT³ observatory, new observational opportunities become available soon. NANTEN2 with the 16-pixel SMART⁴ receiver and a 25'' beam at 810 GHz is well suited for fast mapping of extended areas on the sky. CCAT will be a 25 m diameter telescope with a surface rms of 10 μm and a field of view of 5' x 5' equipped with multi-pixel heterodyne arrays and bolometer cameras (www.submm.org). Its angular resolution is upto 2'' at 1.5 THz. These observatories enable efficient mapping of galactic and extragalactic sources in the CO 4–3 and 7–6 lines as well as in the [C I] atomic fine-structure lines. ALMA will provide follow-up observations at high angular resolution in this frequency range.

The ground-based detection of other important cooling lines of the ISM

² Carbon Heterodyne Array of the MPIfR

³ Cornell Caltech Atacama Telescope

⁴ SubMillimeter Array Receiver for Two frequencies

in the Terahertz regime, e.g. the atomic fine structure lines of [OI], [CII] and [NII], is impossible due to atmospheric absorption. [OI](63 μ m, 145 μ m), [CII](158 μ m) and [NII](122 μ m, 205 μ m) combined with [C I] and CO are the major cooling lines of the gas in the ISM. The major part of [CII] emission originates from the surfaces of PDRs. The combined ratio of [NII](205 μ m) and [CII] is a tracer of the star formation rate and will provide valuable information about the star formation efficiency in different positions of a galaxy as well as different galaxy types.

The airplane observatory SOFIA⁵ will be able to largely overcome the atmospheric limitations and the satellite-mission HERSCHEL will not be affected by the atmosphere. SOFIA with the GREAT⁶ and future STAR⁷ heterodyne receivers and HERSCHEL with HIFI⁸ and PACS⁹ will thus provide insight into the transition from atomic and molecular gas as well as the ionized fraction of the ISM, starting from early 2009. For the first time, small maps of the above mentioned major cooling lines of the ISM will be observable with full velocity resolution. Thus, also more detailed modeling of the central regions of NGC4945 and Circinus (among many other galaxies) will be able to further constrain the physical conditions in these regions.

⁵ Stratospheric Observatory for Infrared Astronomy

⁶ The German first light heterodyne instrument for SOFIA

⁷ SOFIA Terahertz Array Receiver

⁸ Heterodyne Instrument for the Far Infrared

⁹ Photodetection Array Camera Spectrometer

Bibliography

- Aalto, S., Booth, R. S., Black, J. H., & Johansson, L. E. B. 1995, *A&A*, 300, 369
- Aalto, S., Huettemeister, S., Scoville, N. Z., & Thaddeus, P. 1999, 522, 165
- Ables, J. G., Forster, J. R., Manchester, R. N., et al. 1987, *MNRAS*, 226, 157
- Adler, D. S., Lo, K. Y., Wright, M. C. H., et al. 1992, *ApJ*, 392, 497
- Arimoto, N., Sofue, Y., & Tsujimoto, T. 1996, *PASJ*, 48, 275
- Bastian, N., Gieles, M., Efremov, Y. N., & Lamers, H. J. G. L. M. 2005, *A&A*, 443, 79
- Bayet, E., Gerin, M., Phillips, T., & Contursi, A. 2004, 427, 45
- Bayet, E., Gerin, M., Phillips, T. G., & Contursi, A. 2006, *A&A*, 460, 467
- Bell, E. F. & de Jong, R. S. 2001, *ApJ*, 550, 212
- Bell, T. A., Roueff, E., Viti, S., & Williams, D. A. 2006, *MNRAS*, 371, 1865
- Bigiel, F., Leroy, A., Walter, F., de Blok, W. J. G., & Brinks, E. 2007, in *American Astronomical Society Meeting Abstracts*, Vol. 211, American Astronomical Society Meeting Abstracts, 113.06
- Blitz, L. 1993, in *Protostars and Planets III*, ed. E. H. Levy & J. I. Lunine, 125–161
- Blitz, L. & Rosolowsky, E. 2004a, in *Astronomical Society of the Pacific Conference Series*, Vol. 323, *Star Formation in the Interstellar Medium*:

- In Honor of David Hollenbach, ed. D. Johnstone, F. C. Adams, D. N. C. Lin, D. A. Neufeld, & E. C. Ostriker, 89
- Blitz, L. & Rosolowsky, E. 2004b, *ApJ*, 612, L29
- Blitz, L. & Rosolowsky, E. 2006, *ApJ*, 650, 933
- Boissier, S., Prantzos, N., Boselli, A., & Gavazzi, G. 2003, *MNRAS*, 346, 1215
- Bottema, R. 1993, *A&A*, 275, 16
- Boulanger, F. & Perault, M. 1988, *ApJ*, 330, 964
- Bradford, C. M., Nikola, T., Stacey, G. J., et al. 2003, 586, 891
- Bresolin, F., Garnett, D. R., & Kennicutt, R. C. 2004, *ApJ*, 615, 228
- Brock, D., Joy, M., Lester, D. F., Harvey, P. M., & Ellis, H. B. J. 1988, *ApJ*, 329, 208
- Buta, R. & Combes, F. 1996, *Fundamentals of Cosmic Physics*, 17, 95
- Calzetti, D., Kennicutt, R. C., Bianchi, L., et al. 2005, *ApJ*, 633, 871
- Combes, F. 2001, in *Astronomical Society of the Pacific Conference Series*, Vol. 249, *The Central Kiloparsec of Starbursts and AGN: The La Palma Connection*, ed. J. H. Knapen, J. E. Beckman, I. Shlosman, & T. J. Mahoney, 475
- Condon, J. J. 1992, *ARA&A*, 30, 575
- Cox, P. & Mezger, P. G. 1989, *A&A*, 1, 49
- Cunningham, M. R. & Whiteoak, J. B. 2005, *MNRAS*, 364, 37
- Curran, S. J., Johansson, L. E. B., Bergman, P., Heikkilä, A., & Aalto, S. 2001, *A&A*, 367, 457
- Curran, S. J., Johansson, L. E. B., Rydbeck, G., & Booth, R. S. 1998, *A&A*, 338, 863
- Dahlem, M., Golla, G., Whiteoak, J. B., et al. 1993, *A&A*, 270, 29
- Daigle, O. 2006, *MNRAS*, 999, 999

- de Vaucouleurs, G. 1959, *Handbuch der Physik*, 53, 275
- de Vaucouleurs, G., de Vaucouleurs, A., Corwin, H. J., et al. 1991, *Third reference catalogue of bright galaxies* (New York: Springer-Verlag)
- Dos Santos, P. M. & Lépine, J. R. D. 1979, *Nature*, 278, 34
- Elmegreen, B. G. 1993, *ApJ*, 411, 170
- Elmegreen, B. G. 1994, *ApJ*, 425, L73
- Elmegreen, B. G., Elmegreen, D. M., & Montenegro, L. 1992, *ApJS*, 79, 37
- Elmegreen, B. G., Seiden, P. E., & Elmegreen, D. M. 1989, *ApJ*, 343, 602
- Elmegreen, D. M. & Elmegreen, B. G. 1982, *MNRAS*, 201, 1021
- Elmouttie, M., Krause, M., Haynes, R. F., & Jones, K. L. 1998, *MNRAS*, 300, 1119
- Engargiola, G., Plambeck, R. L., Rosolowsky, E., & Blitz, L. 2003, *ApJS*, 149, 343
- Farquhar, P. R. A., Millar, T. J., & Herbst, E. 1994, in *American Institute of Physics Conference Series*, Vol. 312, *Molecules and Grains in Space*, ed. I. Nenner, 135
- Feldmeier, J. J., Ciardullo, R., & Jacoby, G. H. 1997, *ApJ*, 479, 231
- Fixsen, D. J., Bennett, C. L., & Mather, J. C. 1999, 526, 207
- Flower, D. R. & Launay, J. M. 1985, *mn*, 214, 271
- Freeman, K. C., Karlsson, B., Lynga, G., et al. 1977, *A&A*, 55, 445
- Frerking, M. A., Keene, J., Blake, G., & Phillips, T. 1989, 344, 311
- Frerking, M. A., Langer, W. D., & Wilson, R. W. 1982, 262, 590
- Fukui, Y., Mizuno, N., Yamaguchi, R., Mizuno, A., & Onishi, T. 2001, *PASJ*, 53, L41
- Fullmer, L. & Lonsdale, C. J. 1989, *Cataloged galaxies and quasars observed in the IRAS survey* (JPL D, Pasadena: Jet Propulsion Laboratory, 1989, Version 2)

- Garcia-Burillo, S., Combes, F., & Gerin, M. 1993a, 274, 148
- Garcia-Burillo, S., Guélin, M., & Cernicharo, J. 1993b, 274, 123
- García-Burillo, S., Martín-Pintado, J., Fuente, A., & Neri, R. 2001, ApJ, 563, L27
- Gardner, F. F. & Whiteoak, J. B. 1982, MNRAS, 201, 13P
- Gerin, M. & Phillips, T. 2000, 537, 644
- Gerin, M. & Phillips, T. G. 2000, ApJ, 537, 644
- Ghosh, S. K., Bisht, R. S., Iyengar, K. V. K., et al. 1992, ApJ, 391, 111
- Goldreich, P. & Lynden-Bell, D. 1965, MNRAS, 130, 97
- Goldreich, P. & Tremaine, S. 1978, ApJ, 222, 850
- Greenhill, L. J., Herrnstein, J. R., Ellingsen, S. P., et al. 1998, in Bulletin of the American Astronomical Society, 1332
- Greve, A., Kramer, C., & Wild, W. 1998, A&AS, 133, 271
- Guélin, M., Zylka, R., Mezger, P. G., Haslam, C. G. T., & Kreysa, E. 1995, 298, 29
- Güsten, R., Philipp, S. D., Weiß, A., & Klein, B. 2006, A&A, 454, L115
- Helfer, T. T., Thornley, M. D., Regan, M. W., et al. 2003, ApJS, 145, 259
- Helou, G. 1986, ApJ, 311, L33
- Helou, G., Soifer, B. T., & Rowan-Robinson, M. 1985, ApJ, 298, L7
- Henkel, C., Whiteoak, J. B., & Mauersberger, R. 1994, A&A, 284, 17
- Henry, A. L., Quillen, A. C., & Gutermuth, R. 2003, AJ, 126, 2831
- Heyer, M. H., Corbelli, E., Schneider, S. E., & Young, J. S. 2004, ApJ, 602, 723
- Howard, S. & Byrd, G. G. 1990, AJ, 99, 1798
- Hubble, E. 1938, PASP, 50, 97

- Huntley, J. M., Sanders, R. H., & Roberts, Jr., W. W. 1978, *ApJ*, 221, 521
- Israel, F. 2005, *Astrophysics and Space Science*, 295, 171
- Israel, F. P. 2005, *Ap&SS*, 295, 171
- Israel, F. P. & Baas, F. 2002, 383, 82
- Israel, F. P. & Baas, F. 2002, *A&A*, 383, 82
- Israel, F. P., Tilanus, R. P. J., & Baas, F. 2006, *A&A*, 445, 907
- Iwasawa, K., Koyama, K., Awaki, H., et al. 1993, *ApJ*, 409, 155
- Jakob, H., Kramer, C., Simon, R., et al. 2007, *A&A*, 461, 999
- Jansky, K. G. 1982, 1933, *Electrical Disturbances Apparently of Extraterrestrial Origin (Classics in Radio Astronomy)*, 23
- Jarrett, T. H., Chester, T., Cutri, R., Schneider, S. E., & Huchra, J. P. 2003, *AJ*, 125, 525
- Jog, C. J. & Solomon, P. M. 1984, *ApJ*, 276, 127
- Johansson, L. E. B., Aalto, S., Booth, R. S., & Rydbeck, G. 1991, in *Dynamics of Disc Galaxies*, ed. B. Sundelius, 249
- Julian, W. H. & Toomre, A. 1966, *ApJ*, 146, 810
- Kalnajs, A. J. 1973, *Proceedings of the Astronomical Society of Australia*, 2, 174
- Kennicutt, R. C. 1998, *ApJ*, 498, 541
- Kennicutt, Jr., R. C. 1981, *AJ*, 86, 1847
- Kennicutt, Jr., R. C. 1989, *ApJ*, 344, 685
- Kennicutt, Jr., R. C., Calzetti, D., Walter, F., et al. 2007, *ApJ*, 671, 333
- Kim, S., Staveley-Smith, L., Dopita, M. A., et al. 2003, *ApJS*, 148, 473
- Kohno, K., Kawabe, R., Tosaki, T., & Okumura, S. 1996, 461, 29
- Kramer, C., Cubick, M., Röllig, M., & et al., . 2007, *A&A*, submitted

- Kramer, C., Jakob, H., Mookerjea, B., et al. 2004, 424, 887
- Kramer, C., Mookerjea, B., Bayet, E., et al. 2005, A&A, 441, 961
- Kramer, C., Stutzki, J., Röhrig, R., & Corneliussen, U. 1998, 329, 249
- Kregel, M., van der Kruit, P. C., & de Grijs, R. 2002, MNRAS, 334, 646
- Kuno, N. & Nakai, N. 1997, PASJ, 49, 279
- Kuno, N., Nakai, N., Handa, T., & Sofue, Y. 1995a, PASJ, 47, 745
- Kuno, N., Nakai, N., Handa, T., & Sofue, Y. 1995b, PASJ, 47, 745
- Lada, C. J., Alves, J., & Lada, E. A. 1996, AJ, 111, 1964
- Li, Y., Mac Low, M.-M., & Klessen, R. S. 2004, ApJ, 614, L29
- Li, Y., Mac Low, M.-M., & Klessen, R. S. 2005, ApJ, 620, L19
- Li, Y., Mac Low, M.-M., & Klessen, R. S. 2006, ApJ, 639, 879
- Lin, C. C. & Shu, F. H. 1964, ApJ, 140, 646
- Lin, D. N. C. & Pringle, J. E. 1987, ApJ, 320, L87
- Lindblad, B. 1963, Stockholms Observatoriums Annaler, 5
- Lonsdale, C. J. & Helou, G. 1985, Cataloged galaxies and quasars observed in the IRAS survey (Pasadena: Jet Propulsion Laboratory (JPL), 1985)
- Lord, S. & Young, J. 1990, 356, 135
- Lundgren, A. A., Olofsson, H., Wiklind, T., & Rydbeck, G. 2004, A&A, 422, 865
- Maiolino, R., Salvati, M., Bassani, L., et al. 1998, A&A, 338, 781
- Mark, J. W. K. 1976, ApJ, 205, 363
- Martin, C. L. & Kennicutt, R. C. 2001, ApJ, 555, 301
- Matsushita, S., Kohno, K., Vila-Vilaro, B., Tosaki, T., & Kawabe, R. 1998, 495, 267
- Matsushita, S., Sakamoto, K., Kuo, C.-Y., et al. 2004, 616, 55

- Mauersberger, R., Henkel, C., Whiteoak, J. B., Chin, Y.-N., & Tieftrunk, A. R. 1996, *A&A*, 309, 705
- McElroy, D. B. 1995, *ApJS*, 100, 105
- McKee, C. F. & Ostriker, E. C. 2007, *ARA&A*, 45, 565
- Meijerink, R., Spaans, M., & Israel, F. P. 2007, *A&A*, 461, 793
- Meijerink, R., Tilanus, R. P. J., Dullemond, C. P., Israel, F. P., & van der Werf, P. P. 2005, *A&A*, 430, 427
- Misiriotis, A., Xilouris, E. M., Papamastorakis, J., Boumis, P., & Goudis, C. D. 2006, *A&A*, 459, 113
- Mookerjee, B., Kramer, C., Röllig, M., & Masur, M. 2006, *A&A*, 456, 235
- Moorwood, A. F. M. & Oliva, E. 1994, *ApJ*, 429, 602
- Mueller Sánchez, F., Davies, R. I., Eisenhauer, F., et al. 2006, *Å*, 454, 481
- Muller, S. 2006, Ishigaki Conference
- Murphy, E. J., Armus, L., Helou, G., Braun, R., & the SINGS team. 2005, *ArXiv Astrophysics e-prints*
- Nakai, N., Kuno, N., Handa, T., & Y. Sofue, Y. 1994, 46, 527
- Nikola, T., Geis, N., Herrmann, F., et al. 2001, 561, 203
- Ott, M. 1995, PhD thesis, PhD thesis, Univ. Bonn, (1995)
- Ott, M., Whiteoak, J. B., Henkel, C., & Wielebinski, R. 2001, *A&A*, 372, 463
- Patrikeev, I., Fletcher, A., Stepanov, R., et al. 2006, *A&A*, 458, 441
- Quillen, A. C. & Bland-Hawthorn, J. 2008, *MNRAS*, 386, 2227
- Rand, R. J. & Kulkarni, S. R. 1990, *ApJ*, 349, L43
- Rand, R. J., Kulkarni, S. R., & Rice, W. 1992, *ApJ*, 390, 66
- Reber, G. 1940, *ApJ*, 91, 621

- Rickard, L. J., Palmer, P., Morris, M., Zuckerman, B., & Turner, B. E. 1975, *ApJ*, 199, L75
- Risacher, C., Vassilev, V., Monje, R., et al. 2006, *A&A*, 454, L17
- Rots, A., Crane, P., Bosma, A., Athanassoula, E., & van der Hulst, J. 1990, *Astronomical Journal*, 100, 387
- Rydbeck, G., Thomasson, M., Aalto, S., Johansson, L., & Hüttemeister, S. 2004, in *Astronomical Society of the Pacific Conference Series*, Vol. 320, *The Neutral ISM in Starburst Galaxies*, ed. S. Aalto, S. Huttemeister, & A. Pedlar, 152
- Sakamoto, K., Okumura, S., Ishizuki, S., & Scoville, N. 1999, 124, 403
- Sandage, A. 1961, *The Hubble atlas of galaxies* (Washington: Carnegie Institution, 1961)
- Sanders, D. B. & Mirabel, I. F. 1996, *ARA&A*, 34, 749
- Schinke, R., Engel, V., Buck, U., Meyer, H., & Diercksen, G. 1985, 299, 939
- Schinnerer, E., Weiss, A., Scoville, N. Z., & Aalto, S. 2004, in *Bulletin of the American Astronomical Society*, Vol. 36, *Bulletin of the American Astronomical Society*, 812
- Schlegel, D. J., Finkbeiner, D. P., & Davis, M. 1998, *ApJ*, 500, 525
- Schmidt, M. 1959, *ApJ*, 129, 243
- Schuster, K.-F., Boucher, C., Brunswig, W., et al. 2004, *A&A*, 423, 1171
- Schuster, K. F., Kramer, C., Hitschfeld, M., Garcia-Burillo, S., & Mookerjee, B. 2007, *A&A*, 461, 143
- Scoville, N. & Young, J. S. 1983, *ApJ*, 265, 148
- Scoville, N. Z., Polletta, M., Ewald, S., et al. 2001, *AJ*, 122, 3017
- Sellwood, J. A. & Carlberg, R. G. 1984, *ApJ*, 282, 61
- Shetty, R. & Ostriker, E. C. 2008, *ArXiv e-prints*, 805
- Shetty, R., Vogel, S. N., Ostriker, E. C., & Teuben, P. J. 2007, *ApJ*, 665, 1138

- Simon, R., Graf, U., Kramer, C., Stutzki, J., & Onishi, T. 2007, Technical Report: Beam efficiency measurements at NANTEN
- Simon, R., Jackson, J. M., Bania, T. M., Clemens, D. P., & Heyer, M. H. 2000, *Bulletin of the American Astronomical Society*, 32, 708
- Sofue, Y. 1996, *ApJ*, 458, 120
- Sofue, Y., Tutui, Y., Honma, M., et al. 1999, *ApJ*, 523, 136
- Stark, R. & Dishoeck, E. F. V. 1994, 286, L43
- Strong, A. W., Bloemen, J. B. G. M., Dame, T. M., et al. 1988, *A&A*, 207, 1
- Strong, A. W. & Mattox, J. R. 1996, *A&A*, 308, L21
- Stutzki, J. 2001, *Astrophysik I - Skript*
- Stutzki, J., Bensch, F., Heithausen, A., Ossenkopf, V., & Zielinsky, M. 1998, 336, 697
- Stutzki, J. & Güsten, R. 1990, 356, 513
- Stutzki, J. & Winnewisser, G. 1985, *A&A*, 144, 13
- Swings, P. & Rosenfeld, L. 1937, *ApJ*, 86, 483
- Takáts, K. & Vinkó, J. 2006, *MNRAS*, 372, 1735
- Thronson, H. A. & Telesco, C. M. 1986, *ApJ*, 311, 98
- Tieftrunk, A., Jacobs, K., Martin, C., et al. 2001, 23, 23
- Tilanus, R. & Allen, R. 1991, 244, 8
- Tilanus, R. P. J. & Allen, R. J. 1989, *ApJ*, 339, L57
- Tilanus, R. P. J. & Allen, R. J. 1991, *A&A*, 244, 8
- Toomre, A. 1964, *ApJ*, 139, 1217
- Toomre, A. 1977, *ARA&A*, 15, 437
- Toomre, A. 1981, in *Structure and Evolution of Normal Galaxies*, ed. S. M. Fall & D. Lynden-Bell, 111–136

- Toomre, A. & Toomre, J. 1972, 178, 623
- Trewhella, M., Davies, J. I., Alton, P. B., Bianchi, S., & Madore, B. F. 2000, *apj*, 543, 153
- Tully, R. B. 1974a, *ApJS*, 27, 437
- Tully, R. B. 1974b, *ApJS*, 27, 449
- Usero, A., García-Burillo, S., Martín-Pintado, J., Fuente, A., & Neri, R. 2006, *A&A*, 448, 457
- van der Kruit, P. C. & Searle, L. 1981, *A&A*, 95, 105
- Vogel, S. N., Kulkarni, S. R., & Scoville, N. Z. 1988, *Nature*, 334, 402
- Walter, F., Bertoldi, F., Carilli, C., et al. 2003, *nature*, 424, 406
- Walter, F., Brinks, E., de Blok, W. J. G., et al. 2008, *ApJ* submitted
- Walter, F., Brinks, E., de Blok, W. J. G., Thornley, M. D., & Kennicutt, R. C. 2005, in *Astronomical Society of the Pacific Conference Series*, Vol. 331, *Extra-Planar Gas*, ed. R. Braun, 269
- Wang, B. & Silk, J. 1994, *ApJ*, 427, 759
- Wang, M., Henkel, C., Chin, Y.-N., et al. 2004, *A&A*, 422, 883
- Weiss, A., Downes, D., Neri, R., et al. 2007, *A&A*, xx
- Wei, A., Downes, D., Walter, F., & Henkel, C. 2005, *A&A*, 440, L45
- White, G. J., Ellison, B., Claude, S., Dent, W. R. F., & Matheson, D. N. 1994, *A&A*, 284, L23
- Whiteoak, J. B., Dahlem, M., Wielebinski, R., & Harnett, J. I. 1990, *A&A*, 231, 25
- Whiteoak, J. B. & Gardner, F. F. 1974, *Astrophysical Letters*, 15, 211
- Williams, J. P., de Geus, E. J., & Blitz, L. 1994, *ApJ*, 428, 693
- Wilson, A. S., Shopbell, P. L., Simpson, C., et al. 2000, *AJ*, 120, 1325

-
- Wilson, C. D., Scoville, N., Madden, S. C., & Charmandaris, V. 2003, *ApJ*, 599, 1049
- Wong, T. & Blitz, L. 2002, *ApJ*, 569, 157
- Wyse, R. F. G. 1986, *ApJ*, 311, L41
- Yang, C.-C., Gruendl, R. A., Chu, Y.-H., Mac Low, M.-M., & Fukui, Y. 2007, *ApJ*, 671, 374
- Yun, M. S., Reddy, N. A., & Condon, J. J. 2001, *ApJ*, 554, 803
- Zimmer, P., Rand, R. J., & McGraw, J. T. 2004, *ApJ*, 607, 285

Appendix A

^{12}CO 4–3 in NGC 253

We observed the central region of NGC253 in ^{12}CO 4–3 to check the NANTEN2 calibration scheme. This region was already mapped in ^{12}CO 4–3 with the APEX telescope (Güsten et al. 2006). The angular resolution of APEX is $13.3''$ at ^{12}CO 4–3. The APEX data were smoothed to the NANTEN2 HPBW of $38''$ using a Gaussian kernel.

The resulting spectra at the center position are shown in Fig. A.1. The agreement in line temperatures and shapes is very good and thus confirms the calibration scheme at NANTEN2. A investigation of the physical conditions of the central region of NGC 253 using a LVG-approximation can be found in Güsten et al. (2006).

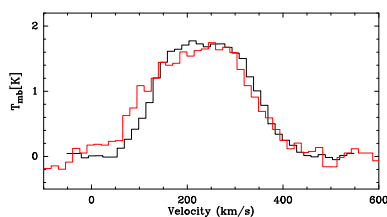


Figure A.1: Observed ^{12}CO 4–3 line emission in NGC 253 from APEX (black line) and NANTEN2 (red line). We attribute small but systematic deviations of peak temperatures in the blue wing of the ^{12}CO 4–3 line to small pointing variations.

List of Figures

2.1	Hubble sequence of galaxy morphology.	21
2.2	An HST composite edge on view of the Sa-type spiral galaxy M101. M101 nicely shows the structure of disk galaxies including the bulge in the center, the disk and the halo (<i>www.spacetelescope.org</i>).	22
2.3	Classification of galaxy morphology by de Vaucouleurs. The sketch is taken from Buta & Combes (1996).	23
2.4	Composite Hubble Space Telescope image of the grand-design spiral galaxy M51 showing the prominent spiral structure (<i>www.spacetelescope.org</i>).	25
2.5	Illustration of different trajectories: a) Definition of the coordinate system. b) General case of a rosette. c) $\kappa = 2\Omega$. d) $\Omega = \Omega_p$	26
2.6	Corotation radius and Lindblad resonances in density wave theory.	27
2.7	Spiral patterns created by small differences in the pattern speed Ω_p in the different orbits.	28
2.8	Sketch of the mechanism of swing amplification of a density wave mode as presented in Toomre (1981).	29

- 2.9 Relation of the global star formation rate Σ_{SFR} and the gas density Σ_{gas} in 61 normal spirals from the sample studied in Kennicutt (1998). Dashed and dotted lines indicate relations for constant global star formation efficiency. 34
- 3.1 Map of ^{12}CO 2–1 integrated intensities [Kkms^{-1}] showing M51 and its companion galaxy NGC 5195 in the north-east. The image has a resolution of $11''$ and is constructed from a masked moment calculation integrating over the full kinematic extent of M51, $350 \text{ kms}^{-1} < v_{\text{lsr}} < 600 \text{ kms}^{-1}$ (see section 3.3.1). Color coded intensities are on a logarithmic scale. The cross marks the 0/0 center position at (eq.2000) The noise level is $1\sigma = 0.65 \text{ Kkms}^{-1}$. Contours range in units of 1σ from 1, 3, 6, 16 to 56 in steps of 10. The peak intensity is 47.3 Kkms^{-1} . All intensities are on the T_{A}^* scale. 47
- 3.2 ^{12}CO 2–1 and ^{13}CO 2–1 observations were conducted with the IRAM-30m telescope on Pico Veleta, Sierra Nevada. . . 48
- 3.3 Map of ^{13}CO 2–1 spectra in the northern spiral arm region of M51. The spectra are on T_{A}^* -scale from -0.01 to 0.05 K and the velocity range covers 300-550 kms^{-1} 54
- 3.4 Map of ^{12}CO 2–1 integrated intensities and ^{13}CO 2–1 in contours on top. The map shows the entire north-eastern spiral arm region where we detected ^{13}CO 2–1 in M51. Contours range in units of 0.5σ from 0.18 to 1.20 Kkms^{-1} . The underlying ^{12}CO 2–1 integrated intensity is given in units of Kkms^{-1} 55
- 3.5 VLA map of the HI column density [$1\text{E}20 \text{ cm}^{-2}$] at $6''$ resolution in colors. Contours show integrated ^{12}CO 2–1 intensities (cf. Fig. 3.1). 56
- 3.6 Map of radio continuum intensities at 20 cm (VLA C+D, $15''$ resolution) in units of Jy/beam (Patrikeev et al. 2006). Contours show integrated ^{12}CO 2–1 intensities (cf. Fig. 3.1). 57

- 3.7 Map of 850 μ m dust emission observed with SCUBA (in raw instrumental units) at the JCMT (Meijerink et al. 2005). ^{12}CO 2–1 in contours and HPBW indicated. 58
- 3.8 Map of the total gas mass surface density Σ_{gas} in M51 in $M_{\odot} \text{pc}^{-2}$ derived from the ^{12}CO 2-1 and H I-emission. The 1- σ value of the total gas density map is $0.8 M_{\odot} \text{pc}^{-2}$. A logarithmic spiral is shown in all Figures of M51 to guide the eye. Contours mark regions discussed in §3.4.1 and Table 3.2. 59
- 3.9 Map of the K -band luminosity L_K from the Two Micron All Sky Survey (2MASS) Large Galaxy Atlas (Jarrett et al. 2003) smoothed to 11'' resolution. The units are L_{\odot} 63
- 3.10 Radial distributions of surface densities of H_2 , H I, the total gas, and the star formation rate per unit area in M51. The lower box shows the ratios $\Sigma_{\text{gas}}/\dot{\Sigma}_{\text{SFR}}$ and $\Sigma_{\text{H}_2}/\dot{\Sigma}_{\text{SFR}}$ 64
- 3.11 Radial distribution of the ratio of atomic Σ_{HI} to molecular surface densities Σ_{H_2} for M51 (thick line), the six spirals of the sample of Wong & Blitz (2002), and M33 (Heyer et al. 2004). For comparison, we show two powerlaws, one where the ratio scales with $R^{1.5}$ and one where it scales with R 66
- 3.12 Map of the ratio of molecular- (Σ_{H_2}) and atomic gas surface density (Σ_{HI}) in M51 derived from the ^{12}CO 2-1 and H I-emission. Regions without detection of ^{12}CO 2-1 are blanked. The 1- σ limit in the ^{12}CO 2-1 data is 0.65Kkms^{-1} corresponding to $\Sigma_{\text{H}_2} = 0.36 M_{\odot} \text{pc}^{-2}$ 68
- 3.13 The fraction of molecular gas density Σ_{H_2} and atomic gas density Σ_{HI} is plotted against the hydrostatic pressure P_{hydro} . The slope found in Blitz & Rosolowsky (2006) is indicated in red. In green the fit to our data P^{fit} is shown. Galactocentric radius in decreasing from left to right. 70

- 3.14 Radially averaged star formation rate per unit area, $\dot{\Sigma}_{\text{SFR}}$, versus surface density of H I, H₂, and the total gas Σ_{gas} . The solid green line is the local Schmidt law found in M51. The dashed-dotted black line is the global Schmidt law found by Kennicutt (1998). Drawn blue lines represent lines of constant gas depletion time or star formation efficiency. 72
- 3.15 The residual map of the total gas surface density after removal of a fitted underlying exponential disk. The exponential disk is shown in contours with contour levels $1 M_{\odot} \text{pc}^{-2}$, $5 M_{\odot} \text{pc}^{-2}$ increasing to $20 M_{\odot} \text{pc}^{-2}$ in steps of $5 M_{\odot} \text{pc}^{-2}$. 79
- 3.16 The residual map of the $850\mu\text{m}$ dust emission after removal of a fitted underlying exponential disk (Fig.2 in Meijerink et al. 2005). The 3σ -level is at 24Jy/beam 80
- 3.17 Radial averaged distribution of the stellar surface density and the the total gas surface density. The dashed line shows stellar densities, ignoring the companion. The mass surface densities of the fitted exponential disks to the total gas density is also shown (cf. Fig.4 in Schuster et al. (2007)). Σ_{dust} is taken from Fig.6 in Meijerink et al. (2005). The ratio of $\Sigma_{\text{gas}}/\Sigma_{\text{dust}}$ for the exponential disk and the residual images, assuming $T_{\text{dust}} = 25K$ in the spiral arms, is shown in the lower box. Dust values below $3\sigma = 24 \text{Jy/beam}$ are ignored 81
- 3.18 Left: Map of the first moment $v_{\text{obs}} = \int T v dv / \int T dv$ showing the intensity weighted mean velocity of the ¹²CO 2–1 data with all points below the $5\text{-}\sigma$ -level blanked. Right: Map of the calculated velocity field v_{mod} using the rotation curve of Garcia-Burillo et al. (1993b,a). The velocity ranges from 370 to 550kms^{-1} . Contour levels in steps of 7kms^{-1} 85
- 3.19 Map of the residuals of the observed velocity field Fig. 3.18a corrected for by the modeled velocity field Fig. 3.18b: $v_{\text{obs}} - v_{\text{mod}} [\text{kms}^{-1}]$ 87

-
- 3.20 Map of the equivalent width Δv_{eq} of the ^{12}CO 2-1 emission in kms^{-1} . In contours the velocity field is shown from 350 kms^{-1} to 600 kms^{-1} in steps of 7 kms^{-1} 90
- 3.21 Map of the square root of the second moment $M_2^{1/2} = (\int T v^2 dv / \int T dv)^{1/2}$ of the HI emission in kms^{-1} . We blanked the M_2 -map where the HI surface density drops below the $3\text{-}\sigma$ level of $1.33 M_{\odot} \text{ pc}^{-2}$ 91
- 3.22 Radial averages of the velocity dispersion of CO (σ_{CO}), HI (σ_{HI}) and the stellar component (σ_*). 92
- 3.23 **Left:** The black drawn line shows the ^{12}CO 2-1 gas dispersion σ_{CO} derived from the observed equivalent widths. Positions without detection of ^{12}CO are ignored. The green drawn line shows the gas dispersion σ_{crit} , assuming gravitational stability, i.e. $\Sigma_{\text{crit}} = \Sigma_{\text{gas}}$. **Right:** The dashed line gives the rotation curve derived by Garcia-Burillo et al. (1993a). 97
- 3.24 Map of the Toomre parameter for the gaseous component Q_{gas} . Pixels with Σ_{gas} below the 3σ -level are blanked. The contours show $Q_{\text{gas}} = 0.5, 1, 2,$ and 5 99
- 3.25 Radial average of the total Toomre parameter Q_{tot} including the stellar contribution. In red the radial average of the gas-only Toomre parameter Q_{gas} is shown. 101
- 3.26 Map of the total Toomre parameter Q_{tot} including the stellar contribution. Pixels with Σ_{gas} below the 3σ -level are blanked. The contours show $Q_{\text{tot}} = 0.5, 1, 2,$ and 5 102
- 3.27 Map of the total Toomre parameter Q_{tot} including the stellar contribution, assuming $\sigma_{\text{gas}} = 6 \text{ kms}^{-1}$ 104
- 3.28 For every position in M51, the total Toomre parameter Q_{total} is plotted against the ratio of the molecular and atomic surface densities $\Sigma_{\text{H}_2}/\Sigma_{\text{H}_I}$. Blue points mark the inner $70''$ of galactrocentric radius. 106

3.29	HST image indicating the Giant molecular cloud associated with M16 (eagle nebula) at 2.1 kpc distance traced by HI in contours (<i>www.spacetelescope.org</i>).	108
3.30	Molecular gas surface density Σ_{H_2} plotted against $(\Sigma_{\text{HI}})^2 \Omega - \Omega_p $. The dashed line represents a slope of 1 which holds when $\Sigma_{\text{H}_2} \propto \Sigma_{\text{HI}}^2 \Omega - \Omega_p $ (Wyse 1986). The drawn line shows the results of a linear fit, excluding one data point near corotation.	109
3.31	Map of the integrated ^{12}CO 2–1 intensity and the 155 clumps identified by <i>Gaussclumps</i>	112
3.32	Binned mass spectrum of the accepted 155 clumps of the ^{12}CO 2–1 emission in M51.	113
3.33	The red lines represent logarithmic spiral fits to the distribution of the 16 most massive GMAs in M51 in a ϕ -lnr-plot. These most massive clumps fitted by <i>Gaussclumps</i> contain 55% of the total clump mass. In the right plot the fits and position are shown on a $\Delta\alpha$ - $\Delta\delta$ -scale.	115
3.34	Map of the integrated ^{12}CO 2–1 intensity and the logarithmic spirals derived by the distribution of the 16 most massive clumps found by the <i>Gaussclumps</i> algorithm.	116
4.1	ESO optical image of the spiral galaxy NGC4945.	121
4.2	HST composite image of the spiral galaxy Circinus.	122
4.3	The NANTEN2 sub-millimeter telescope at Pampa la Bola, Chile. Picture taken by R.Simon.	124

- 4.4 CO 4–3 and [C I] 1–0 spectra of Circinus and NGC 4945 obtained with the NANTEN2 telescope together with low- J CO observations by Curran et al. (2001, 1998); Mauersberger et al. (1996). All data are at $38''$ resolution, only the CO 3–2 spectrum of Circinus is at $15''$ resolution. The small amount of excess emission in the blue wing of the [C I] 1–0 line in Circinus maybe caused by small pointing variations in the eastern direction as emission in lower- J CO lines extends to this region and velocities (Curran et al. 1998). 126
- 4.5 Radiative transfer modeling results and observations: Filled blue points show the observed CO and blue circles the modeled CO. The dotted line indicates the best fit solution. Filled red triangles show the observed ^{13}CO and red triangles the modeled ^{13}CO . Dash-dotted lines show a higher temperature solution. Filled black points are the observed [C I] integrated intensities and black circles the predicted [C I] integrated intensities. 133
- 4.6 a) [C I]1-0/ ^{13}CO 2–1 ratios versus $L([\text{C I}])$. b) [C I]1-0/CO 4–3 ratios versus $L([\text{C I}])$. Black points are the results from Israel & Baas (2002) and red points are the ratios from this thesis. 137
- 5.1 The future CCAT observatory - KOSMA is a partner in this collaborative effort lead by Cornell University and CalTech. The location will be Cerro Chajnantor, Chile (altitude 5.600 m). 143
- 5.2 SOFIA observatory - KOSMA is contributing to the GREAT receiver aboard SOFIA. 145
- A.1 Observed ^{12}CO 4–3 line emission in NGC 253 from APEX (black line) and NANTEN2 (red line). We attribute small but systematic deviations of peak temperatures in the blue wing of the ^{12}CO 4–3 line to small pointing variations. . . . 159

List of Tables

3.1	Basic properties of M51	44
3.2	Properties of Σ_{gas} and $\Sigma_{\text{H}_2}/\Sigma_{\text{HI}}$ in M51 averaged over the areas shown in Fig. 3.8.	61
3.3	Schmidt law $\dot{\Sigma}_{\text{SFR}} = A\Sigma_{\text{gas}}^n$ observed in M51 and other galaxies and samples of galaxies in comparison with the Schmidt law derived simulations	76
3.4	Properties of the exponential gas disk in M51	80
3.5	Equivalent widths Δv_{eq} of CO and HI.	93
3.6	Mass spectra of GMCs and GMAs in external galaxies - powerlaw indices.	113
3.7	Mass spectra of GMCs and GMAs in external galaxies - the mass range.	114
4.1	Basic properties of Circinus and NGC 4945.	120
4.2	Observed line intensities in Circinus and NGC 4945.	127
4.3	Escape probability model results in Circinus and NGC4945.	131

List of Publications

Refereed

A complete ^{12}CO 2–1 map of M51 with HERA. I. Radial averages of CO, H I, and radio continuum, Schuster, K. F., Kramer, C., Hitschfeld, M., Garcia-Burillo, S., & Mookerjea, B. 2007, *Astronomy and Astrophysics*, 461, 143.

^{12}CO 4–3 and [C I] 1–0 at the centers of NGC4945 and Circinus, Hitschfeld, M., et al., 2008, *Astronomy and Astrophysics*, 479, 75

Clumpy photon-dominated regions in Carina. I. [C I] and mid- J CO lines in two $4' \times 4'$ fields, Kramer, C.,..., Hitschfeld, M.,... et al., 2008, *Astronomy and Astrophysics*, 477, 547

Submillimeter line emission from LMC N159W: a dense, clumpy PDR in a low metallicity environment, Pineda, J. L.,..., Hitschfeld, M.,... et al., 2008, *Astronomy and Astrophysics*, 482, 197

A complete ^{12}CO 2–1 map of M51 with HERA. II. Total gas surface densities and gravitational stability, Hitschfeld, M., Kramer, C., Schuster, K. F., Garcia-Burillo, S., Stutzki, J., 2008, *Astronomy and Astrophysics*, submitted.

Ratio of atomic and molecular gas and gravitational stability in the disk of M51, Hitschfeld, M., Kramer, C., Schuster, K.F., Garcia-Burillo, S., Stutzki, J., 2007, *Astronomische Nachrichten*, 328, 638

Non-refereed

A Complete CO 2-1 Map of M51 with HERA, Kramer, C., Hitschfeld, M., Schuster, K.F., Garcia-Burillo, S., Mookerjee, B., 2008, *Mapping the Galaxy and Nearby Galaxies*, 219, Ishigaki, Japan

Giant Molecular Associations in M51, Hitschfeld, M., Kramer, C., Schuster, K., Garcia-Burillo, S., Stutzki, J., 2007, *IAU Symposium*, 237, 427, 26th IAU-General Assembly, Prague, Czech Republic

Gravitational stability in the disk of M51, Hitschfeld, M., Kramer, C., Schuster, K.F., Garcia-Burillo, S., Stutzki, J., 2007, *ArXiv e-prints*, 708, arXiv:0708.2172, *Galaxies in the Local Volume*, Sydney, Australia

Star formation laws in M51 - the HERA CO survey, Kramer, C., Hitschfeld, M., Schuster, K., 2007, *Legacy of multi-wavelength surveys*, Xining, China

Danksagung

Bei den vielen Menschen, die die Erstellung dieser Arbeit durch Diskussionen, Ermutigungen sowie Bereitstellung Ihres unerschöpflichen Wissens und Ihrer langen Erfahrung begleitet haben, möchte ich mich sehr herzlich bedanken:

- bei Prof. Dr. J. Stutzki für die Möglichkeit, die Doktorarbeit im I. Physikalischen Institut durchzuführen, die Betreuung während dieser Zeit und die exzellente Unterstützung, die es ermöglichte schon als Doktorand am internationalen Forschungsumfeld teilzunehmen.
- bei Prof. Dr. F. Bertoldi für die Betreuung im Rahmen der Bonn-Cologne Graduate School, die gute Zusammenarbeit im NANTEN2-Galaxien Projekt und die Bereitschaft als Ko-Referent diese Arbeit zu begutachten.
- bei Priv. Doz. Dr. C. Kramer für die intensive Betreuung, die gute und enge Zusammenarbeit und seine Bereitschaft und Interesse an den Themen und Fragestellungen dieser Arbeit intensiv mitzuarbeiten. Die Reduktion von Daten, Vorbereitung und Durchführung von Beobachtungskampagnen an verschiedenen Teleskopen sowie die nachfolgende Analyse wäre ohne seine Hilfe so nicht möglich gewesen.
- bei Dr. R. Simon für viele Gespräche über physikalische und nicht-physikalische Themen. Gemeinsame Beobachtungsreisen waren eines der Highlights dieser Zeit und immer sehr kurzweilig.

-
- bei Dr. S. Garcia-Burillo, Dr. K. Schuster und Dr. B. Mookerjea für produktive und enge Zusammenarbeit im Rahmen der M51-Analyse.
 - bei dem gesamten KOSMA- und NANTEN2-Team und M. Aravena für die Unterstützung und die Kollaboration während und im Anschluß an NANTEN2-Beobachtungen.
 - bei Priv.Doiz.Dr. V. Ossenkopf, Dr. M. Miller, Dr. M. Röllig und Dr. M. Wiedner für hilfreiche und angenehme Diskussionen in den Gruppentreffen und eine insgesamt sehr angenehme und positive Arbeitatmosphäre in der Gruppe.
 - bei Kefeng Sun für die tolle Büroatmosphäre und einen Zusammenhalt, der weit über die Arbeit hinausging.
 - bei Martin Emprechtinger, Markus Cubick, Oliver Ricken, Pablo Garcia für die gute Stimmung, und vor allem bei Martin für viele interessante und zerstreuende Gespräche die während des Kaffees die Probleme des Alltags vergessen ließen.
 - bei Leo Meyer für die Unterstützung in den ersten beiden Jahren - unsere Gespräche haben mir in der gemeinsamen Zeit von Aachen bis Köln in allen Lebenslagen geholfen.
 - bei allen Freunden und Bekannten, die mich in dieser Zeit begleitet haben.
 - bei meinen Eltern und meiner Schwester für die Unterstützung während der ganzen arbeitsreichen und manchmal nervenaufreibenden Studien- und Promotionszeit.
 - ganz besonders bei meiner Freundin Janka Bönisch für die gemeinsamen letzten Jahre.

Finanzielle Förderung

- Der *Bonn-Cologne Graduate School for Physics and Astronomy* (BCGS) bin ich als Mitglied für die Förderung zu Dank verpflichtet. Ein Teil dieser Dissertation wurde im Rahmen des Promotionsprogrammes der BCGS durchgeführt.



Bonn-Cologne Graduate School
of Physics and Astronomy

- Diese Arbeit wurde im Rahmen des SFB 494¹ durch die *Deutsche Forschungsgemeinschaft* (DFG) finanziell unterstützt.
- IRAM danke ich für finanzielle Unterstützung im Rahmen von Beobachtungsreisen nach Granada zum IRAM-30m Teleskop.

¹Sonderforschungsbereich 494: Die Entwicklung der interstellaren Materie: Terahertz-Spektroskopie in Weltall und Labor.

Erklärung

Ich versichere, daß ich die von mir vorgelegte Dissertation selbständig angefertigt, die benutzten Quellen und Hilfsmittel vollständig angegeben und die Stellen der Arbeit – einschließlich Tabellen, Karten und Abbildungen –, die anderen Werken im Wortlaut oder dem Sinn nach entnommen sind, in jedem Einzelfall als Entlehnung kenntlich gemacht habe; daß diese Dissertation noch keiner anderen Fakultät oder Universität zur Prüfung vorgelegen hat; daß sie – abgesehen von unten angegebenen Teilpublikationen – noch nicht veröffentlicht worden ist sowie, daß ich eine solche Veröffentlichung vor Abschluß des Promotionsverfahrens nicht vornehmen werde.

Die Bestimmungen dieser Promotionsordnung sind mir bekannt. Die von mir vorgelegte Dissertation ist von Prof. Dr. Stutzki betreut worden.

Köln, den 23.9.2008

A handwritten signature in blue ink, appearing to read 'Marc Hitschfeld'.

Marc Hitschfeld

Lebenslauf

Name : Marc Hitschfeld
Anschrift : Gleueler Str. 177
50931 Köln-Lindenthal
Geburtsdatum : 16.07.1979
Geburtsort : Waldbröl, Deutschland
Staatsangehörigkeit : Deutsch
E-Mail : hitschfeld@ph1.uni-koeln.de

Schule

1986 - 1990 Gemeinschafts-Grundschule Obernau
1990 - 1999 Bodelschwingh-Gymnasium Herchen

Universität

10.2000 - 08.2005 RWTH Aachen
Diplomstudium Physik
10.2002 - 09.2003 Queen Mary College London, University of London, UK
Eramus Stipendiat, Physik
seit 10.2005 I. Physikalisches Institut, Universität zu Köln, Deutschland
Promotionsstudium
seit 2006 BCGS for Physics and Astronomy,
Universität zu Köln / Universität Bonn
Stipendiat Promotion

Berufserfahrung

2002 - 2005 Tutor, Institut für theoretische Physik, RWTH Aachen
10.2005 - 12.2008 wissenschaftlicher Mitarbeiter, I. Physikalisches Institut,
Universität zu Köln

